Optical Generation and Detection of High-Frequency Focused Ultrasound and Associated Nonlinear Effects

by

Hyoung Won Baac

A dissertation submitted in partial fulfillment
of the requirements for the degree of
Doctor of Philosophy
(Electrical Engineering)
in The University of Michigan
2012

Doctoral Committee:

Professor L. Jay Guo, Chair
Assistant Professor Pei-Cheng Ku
Professor Theodore B. Norris
Assistant Professor Xueding Wang

2012

To my family

ACKNOWLEDGEMENTS

I would like to express my gratitude and appreciation to my advisor Prof. L. Jay Guo from the bottom of my heart. It was really lucky for me to have such a long journey with him in this graduate school. What he has always showed me was not quantitative knowledge but qualitative values of his endless passion and insights for research which originate from deep and exact understanding. Discussion and communication with him have stimulated my thought and made me happy throughout the graduate study. I could feel I was truly in the academia. I really appreciate his continual support, encouragement, and guidance.

I would like to thank Prof. Theodore Norris, Prof. Pei-Cheng Ku, and Prof. Xueding Wang to serve on my committee and provide valuable suggestions. I express special thanks to Prof. Paul Carson, Prof. Zhen Xu, Prof. A. John Hart, and Dr. Tim Hall for valuable discussion and advice. Also, I would like to appreciate my old advisors who had supported and guided me before I came to Ann Arbor. I cannot forget Prof. Weon Guk Jeong, Prof. Sin-Doo Lee, Prof. Sung June Kim, and Prof. Michael Shuler who have greatly influenced my thought, view, and strategy in research.

I am thankful to my past group members, Dr. Myung-Gyu Kang, Dr. Sehyun Ahn, Dr. Li-Jing Cheng, Dr. Carlos Pina-Hernandez, Dr. Phillip Choi, Dr. Yi-Hao Chen, and current members, Dr. Haofei Shi, Dr. Moon-Kyu Kwak, Brandon Lucas, Hui Joon Park, Tao Ling, Sung-Liang Chen, Jong G. Ok, Yi-Kuei Wu, Alex Kaplan, Hyunsoo Kim, Jae

Yong Lee, Ashwin Panday, Young Jae Shin, Cheng Zhang, Kyu-Tae Lee, Dr. Hongseok Youn, Dr. Jing Zhou, Christina Jones, Long Chen, Kyeongwoon Chung, Taehee Jang, all for sharing precious time, ideas, and experiences. Especially, I am very pleased to work with Jong G. Ok. I would like to give him special thanks for all of his help about carbon nanotubes and valuable discussion over many subjects. Also, I think it was great luck to work with excellent collaborators I could meet here in Michigan, Adam Maxwell, Kuang-Wei Lin, Simone Park, Seunghyun Lee, and Kyung-Hoon Lee. I would like to extend my gratitude to those, not mentioned, who helped me directly and indirectly.

I wish to acknowledge the Korean National Scholarship from Ministry of Education for the PhD study, the National Institute of Health (NIH) in United States for funding the graduate research, and various supports from the Rackham graduate school of University of Michigan.

Finally, I would like to give my heartfelt thanks to my parents, wife, son, and daughter for their love and support.

TABLE OF CONTENTS

LIST OF FIGURES

Figure

ABSTRACT

In this thesis, optical generation and detection of high-frequency ultrasound are presented. On the generation side, high-efficiency optical transmitters have been devised and developed which can generate high-frequency and high-amplitude pressure. Conventional optoacoustic transmitters have suffered from poor optoacoustic energy conversion efficiency (10^{-7}~10^{-8}) and weak output pressure. Such transmitters can work for short-range ultrasonic imaging (a few cm), but the amplitude is weak for long-range imaging and too weak to induce any therapeutic effects. Here, far beyond such traditional regime, high-amplitude pressure was generated going into a therapeutic range (tens of MPa). First, high-efficiency optoacoustic sources were investigated and developed in a planar geometry. Planar transmitters, made by using composites of multi-walled carbon nanotubes and elastomeric polymers, could generate 18-fold stronger pressure than thin metallic films used as a reference, together with providing broadband and high-frequency spectra over 120 MHz. Next, the planar nano-composite films were formed on concave substrates to generate and simultaneously focus the ultrasound. Unprecedented optoacoustic pressure was achieved at lens focus (>50 MPa in positive peaks) which is sufficient to induce shock waves and acoustic cavitation. Due to an inherent high-frequency nature of optoacoustic generation, such therapeutic pressure and the induced effects could be localized onto tight focal widths, 75 μm in lateral and 400 μm in axial directions, which are an order of magnitude smaller than those of traditional high-

amplitude piezoelectric transducers. The shock waves and the cavitation effect were investigated by using various experimental methods. Main features of the optoacoustic approach were discussed such as high frequency, high focal gains, short distances for shock formation, and great flexibility in terms of lens design (lens dimension and *f*-number) and choice of excitation lasers (temporal pulse width and repetition rate). Ultimate performance of the optoacoustic approach will not be limited by specific lenses and optical arrangements used in this work. The laser-generated focusing scheme is expected to open numerous opportunities for a broad range of biomedical applications demanding high-accuracy treatment with minimal damage volumes around focal zones.

For optical detection of ultrasound, optical microring resonators have been used due to their broadband frequency responses (~100 MHz) and high sensitivity. However, high-frequency responses have not been characterized especially where acoustic wavelengths are smaller than ring diameters (~100 μm). The ring geometry can make spatial responses depending on the acoustic wavelengths of incoming waves. This aspect has not been investigated so far despite its importance in practical high-resolution imaging. Here, the microring responses were characterized and theoretically verified in this regime. As a final subject, the microrings were used to detect focused ultrasound and realize novel optoacoustic 4f imaging systems which have capabilities of fast 3-D imaging without requiring mathematical reconstruction steps. Two systems for long- and short-range imaging (focal lengths of 39 mm and 6.5 mm, respectively) were designed and compared. The high-frequency sensitivity of the microrings enabled high-resolution imaging in the 4f arrangement. This was demonstrated by resolving polymer microspheres of 100-μm diameter.

Chapter I

Introduction

1.1 Background

Ultrasound and optoacoustic imaging are realized by ultrasonic transducers which generate and receive acoustic signal. Piezoelectric materials have been commonly used to make the transducers, which convert acoustic pressure to electric energy back and forth [1-3]. These piezoelectric transducers have been widely utilized for biomedical imaging and non-destructive evaluation. They have been developed in a variety of platforms relying on output pressure characteristics (operation frequencies and pressure amplitudes), and structural designs (single element or array; focused or unfocused) [4-6]. The transducer technologies have been developed to improve their performances in terms of resolution, frame rate in scanning, dynamic range, and sensitivity.

The piezoelectric transducers, however, have common drawbacks in frequency characteristics and device fabrication. In terms of frequency characteristics, it is difficult to adjust the frequency ranges and have broad bandwidths. The fixed dimensions of the source materials initially determine the operation frequency in the transducers. Their frequency bandwidth is also limited near the operation frequency. Once these frequency-dependent parameters are determined internally by the materials, they are not tunable for

both generation and detection. In fabrication, a dice-and-fill technique is mostly used to define the piezoelectric elements [7]. The kerf widths, diced by diamond saw (smallest dimension is limited to about 20 μm [3]), give a primary limitation on the high-frequency performance. Additional complexity comes from connecting electrical wires, reducing crosstalk between elements, and matching electrical and acoustic impedances which are associated with piezoelectric material properties and device geometries.

In the traditional transducers, their utilization and improvement have been mostly intended for better imaging in terms of quality and efficiency. However, with developments of high-efficiency transducers, great efforts have been dedicated in another way on the generation side. As the pressure amplitudes from the efficient transmitters can be even focused by acoustic lenses, unusual mechanical and thermal impacts have been created over localized volumes [8-10]. These induce interesting nonlinear phenomena, including secondary effects, such as shock waves, acoustic cavitation, and heat deposition. As a non-invasive approach, the high-amplitude focused ultrasound has inspired emerging interests for biomedical applications both *in vivo* and *in vitro* [11-22]. These have made promising results over broad areas in cancer therapy [11-13], drug delivery [14-17], brain activity modulation [18,19], kidney-stone lithotripsy [20,21], and thrombolysis [22].

In order to generate such strong ultrasound, the piezoelectric transducers have been used as acoustic transmitters or emitters. While they can generate sufficient pressure amplitudes, their focal spots are usually bulky (a few mm in diameter and several to tens of mm in depth) because of low operation frequency ranges over a few MHz [10]. This is not proper for high-accuracy applications which need to minimize potential damages over

regions surrounding the focal volumes. Tighter localization will be achieved if the pressure can be focused at much higher frequency range. The tight confinement of these effects may open new opportunities to explore microscopic interactions of the nonlinear ultrasound with individual cells and a single layer of tissues. Moreover, it is difficult to bring the traditional large transmitters into specific regions *in vivo* to directly deliver the high-amplitude ultrasound. High-voltage electronics and their electrical matching conditions cause additional complexity and limitation [23].

Demands for more efficient ultrasound transducers have led to developing alternate ways by using optical generation and detection. The optical generation of ultrasound is an effective approach to transmit the high-frequency ultrasound through thermo-elastic volume expansion in light-absorbing materials [24,25]. Over several decades, the optoacoustic generation modality has made significant progress continually in terms of theoretical understanding of physical mechanisms as well as experimental methods being promoted by rapid advances in pulsed laser technologies. Beyond the fundamental exploration stage of the mechanisms, the optoacoustic approach has grown as a new transmitter platform becoming a rival against the traditional transducer technologies [26,27]. It has various advantages in terms of operation and fabrication. In thin-film optoacoustic transmitters, the frequency spectra of output pressure can be determined externally by the frequency characteristics of excitation light sources. As long as optical absorption depths in the source material are very thin (compared to an acoustic transit distance during a given temporal width of laser pulse), the film thickness can be acoustically neglected. This means that the operation frequency and the bandwidth can be optically controlled using a single transmitter. The high-frequency ultrasound, even

higher than 100 MHz, has been easily obtained by using short laser pulses (*e.g.* nanosecond pulses). Also, it is easy to realize micro-scale source arrays [28]. As the individual source element is optically defined, focused laser spots on an order of several micrometers can be achieved without difficulty. Finally, they do not have any complex issues associated with the electronic connections.

However, weak output pressure has been a major issue in the optoacoustic transmitters. This is due to poor optoacoustic energy conversion process which is relevant to optical and thermal properties of the source materials. These transmitters are made using light-absorbing thin films containing specific structures designed to have high optical absorption and efficient thermo-acoustic conversion process. Various thin-film transmitters have proposed using metal coating [29], dye-doped polymer composites [26,30], and two-dimensional (2-D) gold nanoparticle (AuNP) arrays [27,28]. However, these have not fully satisfied both needs for strong pressure amplitude and high frequency spectra. Furthermore, due to the poor energy conversion issue, the optoacoustic transmitters could not achieve high enough amplitudes to induce the nonlinear acoustic effects.

Optical detection of ultrasound has been extensively studied using various approaches over several decades [31-42]. A classical passive detection method simply uses optical reflection from surface under interests. The mechanism is based on conversion of acoustic vibration on the surface into a linear optical modulation of a probing laser beam. However, its sensitivity is poor because the surface displacement is generally very tiny on the order of several nm. In order to enhance the sensitivity, various advanced configurations have been proposed using optical interferometric mechanisms,

such as Fabry-Perot structures [31-37], microring resonators [38-41], and Mach-Zehnder interferometers [42]. Among these detectors, the microring resonators have exhibited excellent characteristics in terms of frequency response, sensitivity, and spatial dimension: flat wideband response over >90-MHz at 3 dB roll-off [40]), low noise-equivalent pressure of ~21 Pa [41] over 1~75 MHz range which is far better than the other optical detectors, and small dimensions of 40~100 μm in diameter and ~2 μm in waveguide width. One of the criteria to determine the sensitivity of these structures is a quality factor Q at their optical resonance. A high Q-factor of 4×10^5 has been obtained in the microrings [41]. These values are contrasted to the other configurations (typically lower than several thousands). Due to these excellent characteristics, the microrings have extended their applications over ultrasound and optoacoustic imaging.

1.2 Motivation and Thesis Organization

The features and the advantages of the optoacoustic generation approach provide strong motivation to develop high-efficiency transmitters which can generate strong and high-frequency ultrasound and thereby open new possibilities for biomedical applications. The existing works for the optoacoustic transmitters exhibited the high-frequency capability, but their applications were simply limited to high-resolution imaging in short ranges. As mentioned previously, the high-amplitude ultrasound has already shown great potentials in the conventional transducers. If this can be realized in the high-frequency regime, it will provide numerous opportunities for a wide range of biomedical applications *in vivo* and *in vitro*, such as high-accuracy therapy and highly localized

treatment/modulation for cells, tissues, and specific regions of the body, all of which have not been achieved by the traditional transducer technologies. Note that an accurate definition or a focal confinement is always related to the short wavelength or the high frequency. Also, the high-frequency nonlinear ultrasound itself is a subject of interest in terms of fundamental understanding of physical behaviors [43].

For optical detection of ultrasound, the optical microring detectors are attractive platforms due to the superior sensitivity, frequency response, and small dimension in diameter. While the sensitivity and the frequency response of the microring detector have been investigated in various works, its geometrical response has not been studied. The microring detector has a finite dimension in its diameter (<100 μm) and waveguide width (~2 μm). For the high frequency ultrasound, the acoustic wavelength can be comparable or even smaller than the microring diameter (*e.g.* 100-μm wavelength corresponds to 15 MHz frequency in water). It is essential to evaluate the microring responses for ultrasound with a spatial scale smaller than the detector dimension.

In the optoacoustic generation using the pulsed lasers, the high-frequency amplitudes are usually weaker than the low-frequency ones. Better sensitivity in the detector means that more pressure amplitudes are available over the high-frequency components. This can make significant difference in spatial resolutions in imaging applications. Due to the high sensitivity of the microrings, they are suitable to detect weak high-frequency ultrasound and realize high-resolution imaging. We utilize such advantage to design a novel optoacoustic 4f imaging system which is capable of mapping spatial information in an object plane onto an image plane with one-to-one correspondence [44]. Two different systems are designed for long-range and short-range

optoacoustic imaging.

The optical transmitters and the optical detectors can be integrated into a single platform, and then it is possible to make all-optical transducers. Such integrated forms become exact counterparts against the conventional transducers. Moreover, the broadband and high-frequency characteristics of the optoacoustic ultrasound can be received with minimal loss by the optical detectors. This is because the optical detectors bear similar frequency responses with the spectra of the optically generated ultrasound. Particularly, the broadband properties cannot be obtained by the piezoelectric transducers for both generation and detection. The optical transmitters developed here can be integrated with the microring detectors, becoming the all-optical transducers.

In chapter 2, the thin-film optoacoustic transmitters are introduced. We theoretically estimate how to obtain high-efficiency transmitters. Using a composite film of multi-walled carbon nanotubes (MW-CNTs) and elastomeric polymers as an optoacoustic transmission source, we realize the optoacoustic transmitters which can generate strong and high-frequency ultrasound.

In chapter 3, the CNT-polymer composite films are used to develop focused transmitters by forming the films on curved substrates. The high-frequency and the high-amplitude characteristics of focused ultrasound are demonstrated. As the pressure amplitudes at lens focus are high enough to induce nonlinear driven effects such as shock distortion and acoustic cavitation, these aspects are extensively investigated by using various experimental methods.

In chapter 4, the optical detection of high-frequency ultrasound is demonstrated. Especially, we use the microring detectors and characterize their responses to focused

ultrasound with broadband and high-frequency spectra. We evaluate specific responses of the microring detector to the high-frequency components which have short wavelengths and produce tight focal spots smaller than the detector size.

In chapter 5, the optical microring detector is used for optoacoustic imaging. A novel 4f imaging configuration is proposed taking advantages of the microring detector in terms of high sensitivity, high-frequency response, and small geometrical dimension. The optoacoustic imaging results are compared for two different configurations: long-range and short-range. High-frequency performance of the imaging systems is discussed.

In chapter 6, we conclude the optical generation and detection approaches investigated in this dissertation. Future works are suggested.

References

[1] K. R. Erikson, F. J. Fry, and J. P. Jones, IEEE Trans. Sonics, Ultrason., 21, 144 (1974).

[2] W. P. Mason, IEEE Trans. Sonics, Ultrason., 23, 224 (1976).

[3] R. S. C. Cobbold, *Foundations of Biomedical Ultrasound*, Oxford University Press, New York (2007).

[4] J. M. Cannata, J. A. Williams, Q. Zhou, T. A. Ritter, and K. K. Shung, IEEE Trans. Ultrason., Ferroelect., Freq. Contr., 53, 224 (2006).

[5] E. J. Gottlieb, J. M. Cannata, C. H. Hu, and K. K. Shung, IEEE Trans. Ultrason., Ferroelect., Freq. Contr., 53, 1037 (2006).

[6] J. O. Fiering, P. Hultman, W. Lee, E. D. Light, and S. W. Smith, IEEE Trans. Ultrason., Ferroelect., Freq. Contr., 47, 764 (2000).

[7] T. A. Ritter, T. R. Shrout, R. Tutwiler, and K. K. Shung, IEEE Trans. Ultrason., Ferroelect., Freq. Contr., 49, 217 (2002).

[8] C. C. Coussios and R. A. Roy, Annu. Rev. Fluid Mech. 40, 395 (2008).

[9] E. Herbert, S. Balibar, and F. Caupin, Phys. Rev. E 74, 041603 (2006).

[10] E. A. Filonenko and V. A. Khokhlova, Acoust. Phys. 47, 468 (2001).

[11] J. E. Kennedy, Nat. Rev. Cancer 5, 321 (2005).

[12] Y.-F. Zhou, World J. Clin. Oncol. 2, 8 (2011).

[13] T. J. Dubinsky, C. Cuevas, M. K. Dighe, O. Kolokythas, J. H. Hwang, Am. J. Roentgenol. 190, 191 (2008).

[14] S. Mitragotri, Nat. Rev. Drug Discov. 4, 255 (2005).

[15] J. J. Choi, K. Selert, Z. Gao, G. Samiotaki, B. Baseri, and E. E. Konofagou, J. Cerebral Blood Flow Metabol. 31, 725 (2011).

[16] B. Krasovitskia, V. Frenkelb, S. Shohama, and E. Kimmela, Proc. Natl Acad. Sci. USA 108, 3258 (2011).

[17] S. Song, Z. Shen, L. Chen, A. A. Brayman, and C. H. Miao, Gene Ther. 18, 1006 (2011).

[18] Y. Tufail, A. Yoshihiro, S. Pati, M. M. Li, and W. J. Tyler, Nat. Protocols 6, 1453 (2011).

[19] S.-S. Yoo, A. Bystritsky, J.-H. Lee, Y. Zhang, K. Fischer, B.-K. Min, N. J. McDannold, A. Pascual-Leone, and F. A. Jolesz, Neuroimage 56, 1267 (2011).

[20] J. E. Lingeman, J. A. McAteer, E. Gnessin, and A. P. Eva, Nat. Rev. Urology 6, 660 (2009).

[21] J. J. Rassweiler, T. Knoll, K.-U. Köhrmann, J. A. McAteer, J. E. Lingeman, R. O. Cleveland, M. R. Bailey, C. Chaussy, Eur. Urol. 59, 784 (2011).

[22] C. Goldenstedt, A. Birer, D. Cathignol, and C. Lafon, Ultrasound Med. Biol. 35, 985 (2009).

[23] X. Geng, T. A. Ritter, and K. K. Shung, IEEE Ultrasonics Symposium Proceedings 1191 (1999).

[24] V. E. Gusev and A. A. Karabutov, Laser Optoacoustics, AIP Press, New York (1993).

[25] M. O'Donnell, Y. Hou, J.-S. Kim, S. Ashkenazi, S.-W. Huang, and L. J. Guo, Eur. Phys. J. Special Topics 153, 53 (2008).

[26] T. Buma, M. Spisar, and M. O'Donnell, Appl. Phys. Lett. 79, 548 (2001).

[27] Y. Hou, J.-S. Kim, S. Ashkenazi, M. O'Donnell, and L. J. Guo, Appl. Phys. Lett. 89,

093901 (2006).

[28] Y. Hou, J.-S. Kim, S. Ashkenazi, S.-W. Huang, L. J. Guo, and M. O'Donnell, Appl. Phys. Lett. 91, 073507 (2007).

[29] R. J. von Gutfeld and H. F. Budd, Appl. Phys. Lett. 34, 617 (1979).

[30] E. Biagi, F. Margheri, and D. Menichelli, IEEE Trans. Ultrason. Ferroelect., Freq. Contr., 48(6), 1669 (2001).

[31] J. P. Monchalin, Appl. Phys. Lett. 47, 14 (1985).

[32] H. Sontag, and A. C. Tam, IEEE Trans. Ultrason., Ferroelect., Freq. Contr., 33, 500 (1986).

[33] R. J. Dewhurst, and Q. Shan, J. Meas. Sci. Technol. 5, 655 (1994).

[34] P. C. Beard and T. N. Mills, Appl. Opt. 35, 663 (1996).

[35] S. Ashkenazi, Y. Hou, T. Buma, and M O'Donnell, Appl. Phys. Lett. 86, 134102 (2005).

[36] S.-W. Huang, S.-L. Chen, T. Ling, A. Maxwell, M. O'Donnell, L. J. Guo, and S. Ashkenazi, Appl. Phys. Lett. 93, 113501 (2008).

[37] E. Zhang, J. Laufer and P. Beard, Appl. Opt. 47, 561 (2008).

[38] C. Y. Chao, S. Ashkenazi, S.-W. Huang, M. O'Donnel, and L. J. Guo, IEEE Trans. Ultrason., Ferroelect., Freq. Contr. 54, 957 (2007).

[39] A. Maxwell, S.-W. Huang, T. Ling, J.-S. Kim, S. Ashkenazi, and L. J. Guo, IEEE J. Select. Topics Quantum Electron. 14, 191 (2008).

[40] S.-W. Huang, Y. Hou, S. Ashkenazi, and M. O'Donnell, Appl. Phys. Lett. 92, 193509 (2008).

[41] T. Ling, S.-L. Chen, and L. J. Guo, Appl. Phys. Lett. 98, 204103 (2011).

[42] G. Paltauf, R. Nuster, M. Haltmeier, and P. Burgholzer, Appl. Opt. 46, 3352 (2007).

[43] M. F. Hamilton and D. T. Blackstock, *Nonlinear Acoustics*, Acoustical Society of America, Melville (2008).

[44] J. W. Goodman, Fourier Optics, 3rd edition, Roberts & Company Publishers, Colorado (2004).

Chapter II

Optical Generation of High-Frequency Ultrasound from Thin-Film Transmitters

2.1 Introduction

Thin metallic coatings on solid substrates have been used as a common reference material to qualify the performance of optoacoustic transmitters [1,2]. The metal thin films (typically <a few hundreds nm in thickness) are suitable for high frequency ultrasound sources because the acoustic transit time over the thin films can be much shorter than the duration of pulsed laser. For example in 1-D structures, this allows to replicate a frequency spectrum of laser pulse to an acoustic one with minimal broadening. However, their optoacoustic conversion efficiency in the metal films is poor mainly because of low light-absorption and low thermal expansion. Also, acoustic impedances of the metals are largely different to that of surrounding liquids (*e.g.* water), which is not desirable for efficient pressure transfer. For highly efficient transmitters for strong and high frequency ultrasound generation, it is essential to have high optical absorption, high thermal expansion, fast thermal transition, acoustic impedance matching with the surrounding medium, and geometrically thin structure.

Commonly, thermal expansion in polymer is larger than those of metals and water. Acoustic impedances of polymers are usually close to water as compared with other metallic materials. These aspects have been utilized to efficiently convert thermal heating to optoacoustic pressure. An elastomeric polymer, polydimethylsiloxane (PDMS), has been used as a thermal transfer medium to interface with light-absorbers [1-4]. A composite film of PDMS with carbon black as a light-absorber has shown nearly 20 dB improvement in optoacoustic signal strength as compared to a reference Cr film alone [1]. However, high frequency response was severely limited due to the composite film thickness (~25 μm) due to the acoustic attenuation. This is a serious issue because high frequency performance is vital for optoacoustic transmitters. Moreover, it is challenging to obtain uniform mixing and dispersion of carbon black particles in the PDMS matrix. Agglomeration of carbon black can cause uneven light absorption within the same film. Significant progress has been recently made using a planar array of AuNPs with an overlying PDMS layer of several microns [4]. High frequency output was improved by ~5 dB over 70~100 MHz as compared with those carbon black-PDMS composites. However, the overall pressure strength was compromised because the optical absorption in the AuNP is usually lower than that in the carbon black-PDMS composite. In addition, the AuNP has a lower damage threshold (~1/6) than the carbon black-PDMS composite, which limits the ultimate attainable pressure [3,5].

Here, we demonstrate the use of CNTs as optoacoustic transmitters for strong and high frequency ultrasound generation. A thin film of CNT-PDMS composite (>1 μm) can absorb 40~99% of incident visible light which depends on the CNT density. We use grown multi-walled CNTs on a fused silica substrate, followed by spin-coating of PDMS.

The CNTs are distributed densely near the substrate. Therefore, most of light is absorbed over the thin CNT-rich region. The high thermal expansion of PDMS is utilized to obtain strong optoacoustic pressure. As the overall thickness is thin, acoustic attenuation and scattering across the film is negligible. Also, the acoustic impedance of the PDMS is close to the surrounding water. The output pressure of the CNT-PDMS composite was compared to a bare Cr film and a planar AuNP array. We obtained >25 dB stronger pressure in the composite film than in the Cr film used as a reference. We performed a frequency-domain analysis, confirming that the CNT-PDMS composite exhibits excellent optoacoustic conversion. The output pressure spectrum closely follows that of the laser pulse used for excitation. We note that the CNT density is uniform on the growth substrate, which gives uniform density in the composite.

2.2 Theoretical Analysis: 1-D Layered Model for Thin-Film Optical Transmitters

In this work, we use a moderate laser fluence to non-destructively generate acoustic waves. Avoiding laser ablation, we generate the optoacoustic waves through thermoelastic volume expansion process by using laser pulses. The optoacoustic generation problem can be solved by thermal diffusion and acoustic wave equations. In our configuration, the optoacoustic source area which is determined by the laser beam diameter is much larger than the film thickness. Therefore, we can consider our thin-film structure as a 1-D layered model. Fig. 2.1 shows the schematic for the model.

In order to identify the optoacoustic process in the given structures, it is essential

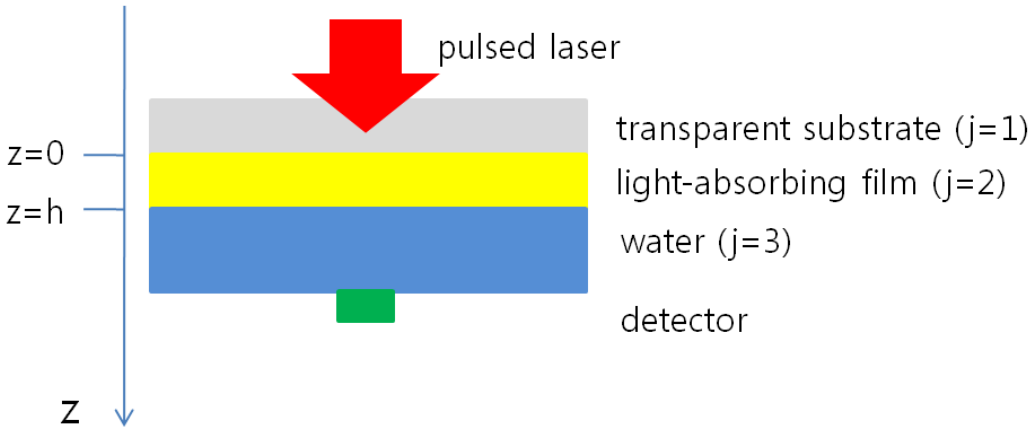

Fig. 2.1 1-D layered structure for optoacoustic generation.

to determine the characteristic spatial scales. First, the optical absorption depth (< 1~2 μm) is very short compared to the acoustic wavelengths in the range of interest. Over the optical absorption depth, the acoustic transit time is much smaller than the temporal duration of the laser pulses. Consequently, acoustic pulse broadening is negligible. For a 500-nm thick metal layer, the acoustic transit time is on the order of 0.1 ns (<< 6-ns pulse width of laser). This assumption is valid because we use thin-film absorbers such CNT and gold nano-structure in our work. The second scale is the thermal diffusion depth. For 6-ns laser pulse duration, the optically induced heat can diffuse in the range of 20~30 nm in polymer and water. Meanwhile, the acoustic waves propagate on the order of 5~10 μm which is much larger than the thermal diffusion depths. This justifies the mechanism of optoacoustic generation in which the generated heat is spatially confined to a small volume of the optical absorption source. Therefore, the contribution of thermal waves is neglected in our model.

Theoretical analysis for the 1-D layered model has been investigated by Kopylova *et al* [6,7]. For the layered media shown in Fig. x, thermal diffusion process is described by

$$\frac{\partial T_j}{\partial t} = \frac{\kappa_j}{\rho_j c_{p_j}} \frac{\partial^2 T_j}{\partial z^2} \tag{2.1}$$

where T_j is the temperature field, κ_j is the thermal conductivity, ρ_j is the density, and c_{pj} is the specific heat capacity for each medium. At each boundary, temperature is continuous, but heat flux is not continuous at the position of optical source layer. As we neglect the spatial dependence of optical absorption in the z-direction, the optothermal source exists only at the boundary. The boundary conditions are given as

$$T_1\big|_{z=0^-} = T_2\big|_{z=0^+} \tag{2.2}$$

$$T_2\big|_{z=h^-} = T_3\big|_{z=h^+} \tag{2.3}$$

$$-\kappa_1 \frac{\partial T_1}{\partial z}\bigg|_{z=0} + \kappa_2 \frac{\partial T_2}{\partial z}\bigg|_{z=0} = I_\alpha L(t) \tag{2.4}$$

$$\kappa_2 \frac{\partial T_2}{\partial z}\bigg|_{z=h^-} = \kappa_3 \frac{\partial T_3}{\partial z}\bigg|_{z=h^+} \tag{2.5}$$

where I_α is the absorbed laser intensity and $L(t)$ is the time profile of laser pulse. Then, the acoustic wave equation for the velocity potential can be solved by using a source term which is obtained from the above thermal diffusion problem. This is written as

$$\frac{1}{c_{Lj}^{\ 2}}\frac{\partial^2\phi_j}{\partial t^2}-\frac{\partial^2\phi_j}{\partial z^2}=-\beta_j^{\ *}\frac{\partial T_j}{\partial t} \tag{2.6}$$

Here, ϕ_j is the velocity potential which is a function of time and distance, c_{Lj} is the longitudinal sound velocity, and β_j^* is the effective thermal coefficient of volume expansion in solid [8]. Using the spectral decomposition in frequency-domain, we can obtain the solution for the velocity potential. Finally, the generated pressure for the 1-D layered model can be represented by

$$P_3(w)=\frac{Z_1Z_3}{Z_1+Z_3}\left\{\frac{\beta_2^{\ *}}{\rho_2 c_{p2}}\left(\kappa_2\frac{\partial T_2}{\partial z}\bigg|_{z=0}-\kappa_2\frac{\partial T_2}{\partial z}\bigg|_{z=h}\right)+\frac{\beta_3^{\ *}}{\rho_3 c_{p3}}\left(\kappa_3\frac{\partial T_3}{\partial z}\bigg|_{z=h}\right)\right\}I_\alpha L(w) \tag{2.7}$$

where Z_j is the acoustic impedance. The term $\beta_j^*/\rho_j c_{pj}$ determines the thermal expansion effect for the given heat capacity and density of each medium. Multiplication of this term with the heat flux gives the unit of [m/s] which corresponds to the particle vibration velocity induced by heat. In this derivation, we did not consider the frequency-dependent acoustic attenuation and the frequency dependence of thermo-physical parameters (β_j^* and κ_j). In most of the thin-film transmitters, we can assume the optical absorption occurs near the substrate/film interface. Then, the first-term is dominant in the eq. (2.7). The temperature increase can be described as [9],

$$\Delta T_2\big|_{z=0}=\frac{F\mu}{\rho_s c_{ps}}\times\frac{\tau_{HD}}{\tau_L}\times\left\{1-\exp\left(-\frac{\tau_L}{\tau_{HD}}\right)\right\} \tag{8}$$

where ρ_s and c_{ps} are the density and the specific heat capacity of the optical absorption source. Also, F is the optical fluence, μ is the optical absorption (normalized to source′s volume), τ_L is the temporal width of the laser pulse, and τ_{HD} is the heat diffusion time into the surrounding medium.

2.3 CNT-Polymer Composite Films as Efficient Transmitters

The CNTs are known to efficiently transform absorbed light into thermal energy [10], which is attractive for optoacoustic generation. For example, CNTs conjugated with peptides have been used as high contrast optoacoustic agents for tumor imaging in living mice [11]. However, CNTs have not been exploited as optoacoustic transmitters for ultrasound imaging. More importantly, CNTs have not been demonstrated as high-frequency ultrasound sources. The CNTs are attractive as sources for high-frequency ultrasound generation due to the following reason. Their nano-scale dimension inherently allows fast heat transition to the surrounding medium. The heat diffusion time in the eq. (2.8) can be <1 ns as it decreases approximately with $d^2/16\chi$ (assuming the CNT as a solid cylinder of the diameter d, being surrounded by a medium with thermal diffusivity χ [12]. This becomes a crucial motivation for high-frequency ultrasound generation. While this dimensional feature is shared with other metallic nanoparticles [13], the CNTs have extraordinary thermal conductivity (20~30 times larger than that of typical metal)

facilitating heat conduction within the structure [14]. Moreover, the CNT has significant advantages in terms of material preparation, than the gold nanoparticles. As we grow the CNTs in a vapor phase on substrates in a controlled manner, we can fabricate highly packed CNTs to have the optical absorption up to 100%. Such high absorption is not easy to be achieved in the gold nanoparticles. Also, the vapor-phase growth means that the CNTs can be grown on substrates with arbitrary geometries: for example, highly curved lenses.

2.3.1 Experimental setup

Figure 2.2 shows the experimental setup to generate and measure optoacoustic signal. A 6-ns pulsed laser beam with 532 nm wavelength (Surelite I-20, Continuum, Santa Clara, CA) was directly irradiated onto the transparent substrate. We note that the laser beam size is two orders of magnitude larger than the dimension of microring detector. Also, the beam diameter is >10 times larger than the distance between sample and detector. This approximately satisfies a plane wave configuration where the acoustic wave is incident onto the detector. It is important to minimize diffraction-induced errors, especially for high frequency characterization. Such arrangement allows the temporal waveforms of the acoustic pulse to replicate the laser pulse shape [15].

We used a polymer microring resonator to characterize broadband and high frequency acoustic signal [16-18]. The polystyrene microring was fabricated on a SiO_2/Si substrate by using an imprint technique. The microring has a diameter of 100 μm and a waveguide width of 2 μm. The optical detection with a probe laser beam and data

acquisition processes are similar to the previously reported [18]. An erbium-doped fiber amplifier was used to increase the optical output from a tunable laser. For ultrasound detection, the wavelength of the probe beam was fixed at the maximum slope of the resonance dip in the optical transmission spectrum.

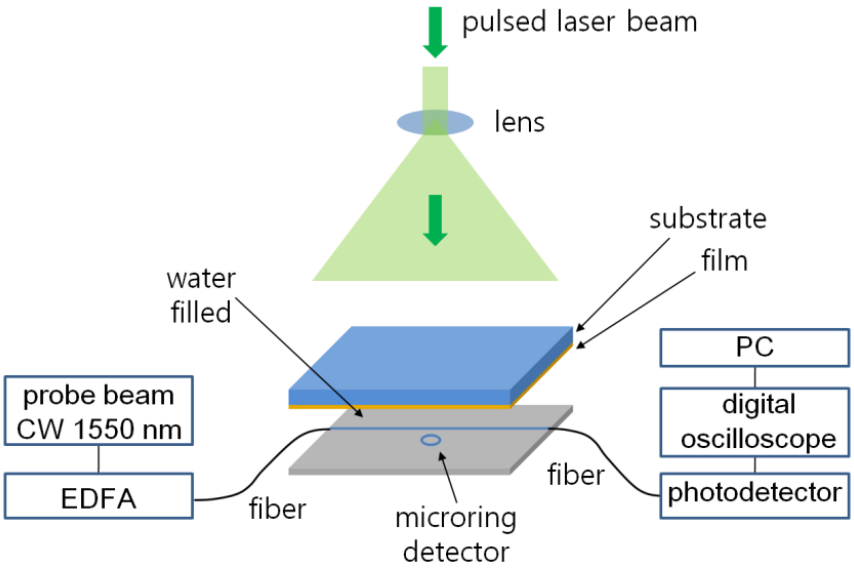

Fig. 2.2 Experimental setup to generate and measure optoacoustic signal.

2.3.2 Preparation of CNT-Polymer Composite Films

We prepared three light-absorbing films as optoacoustic transmitters: Cr, CNT with PDMS, and AuNP array with PDMS. A 100 nm thick Cr film was used as a reference. The multi-walled CNTs were grown on a fused silica substrate coated with a catalyst layer of Fe (≈1 nm thickness). Detailed growth process is described in Appendix A. Next, the as-prepared CNTs were spin-coated with PDMS (4000 r.p.m. for 1 min.)

which has a modified composition to enhance elastic modulus [19]. Figure 2.3 shows scanning electron microscopy (SEM) images for the as-grown CNTs and the CNT-PDMS composite film. Originally, some of the CNT strands in the grown CNTs were directed normal to the substrate. However, after PDMS coating, all CNT strands are squeezed in plane within the PDMS film. The cross-sectional view in Fig. 2.3(a) confirms that the PDMS is well mixed with the nanoscale CNT strands. It is also shown that the CNT strands are dense near the substrate. Therefore, the optical absorption and the consequent optoacoustic generation would occur predominantly near the substrate. Final thickness of the composite films could be controlled in the range of 1~10 μm by changing initial densities of CNTs and spin-coating conditions. Fig. 2.3(b) shows an example of the denser CNTs and the thick PDMS film. The planar AuNP array in Fig. 2.3(c) was fabricated by using a metal transfer method onto the fused silica substrate [20]. The dimension of a single AuNP dot is 110 nm × 110 nm × 30 nm. The AuNP array was then spin-coated with 800-nm thick PDMS layer. In the case of the AuNP array with PDMS, a significant portion of incident light is reflected and scattered, which does not contribute to the optoacoustic generation process.

2.3.3 Optoacoustic Generation of Strong and High-Frequency Ultrasound

Figure 2.4 shows the output pressure waveforms generated from three samples under the same laser fluence. Each curve was obtained by averaging 200 waveforms. The signal amplitude from the CNT-PDMS composite film shown in Fig. 2.3(b) was 18-fold (25 dB) stronger than that of the Cr, and 5-fold (14 dB) stronger than that of the PDMS-

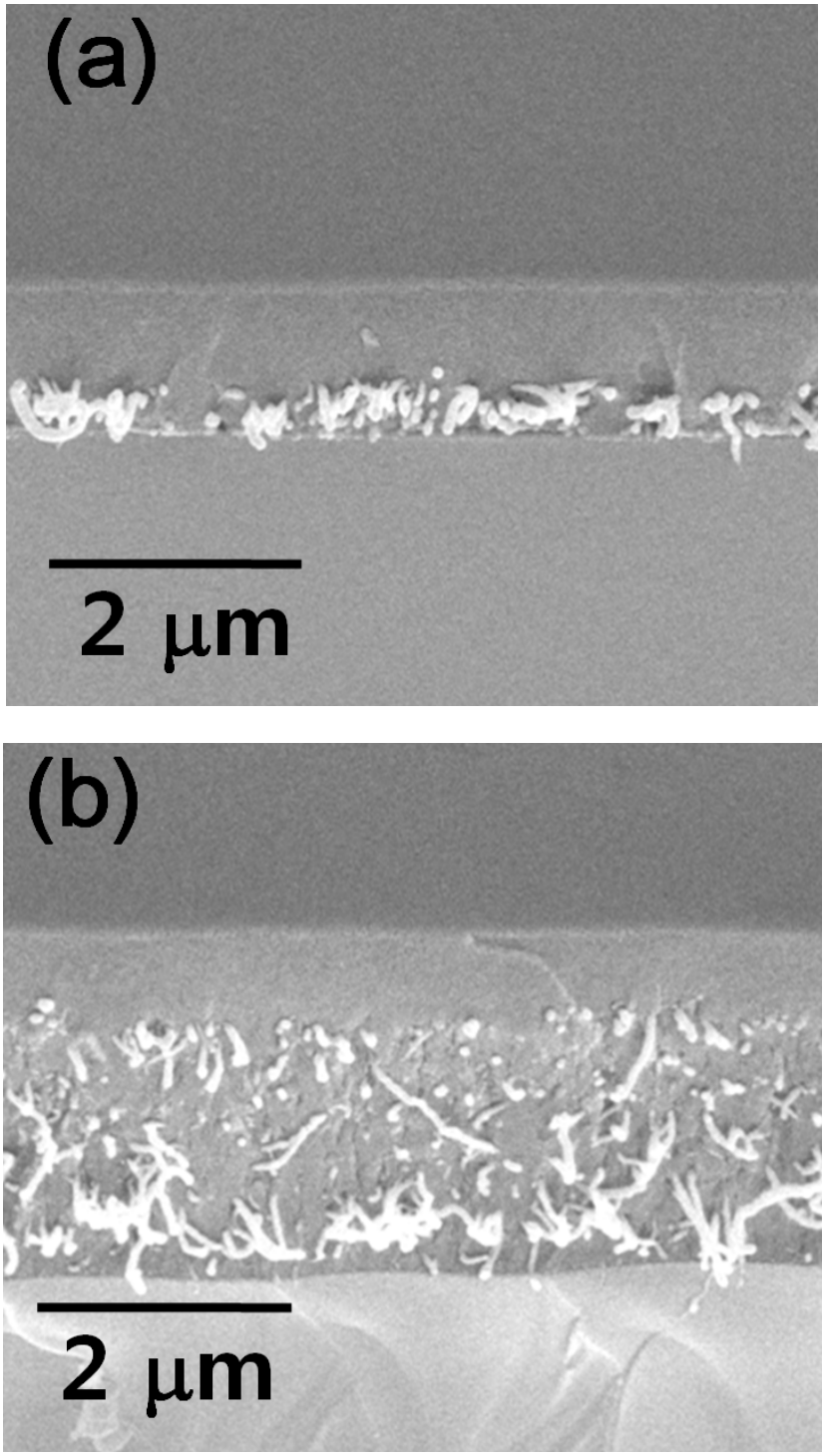

Fig. 2.3 SEM photographs of the CNT-PDMS composite films where the CNT growth time was 1 min in (a) and 3 min in (b), and the AuNP array before PDMS coating in (c). Fused silica substrates were used for all cases. The composite thickness is 1.2 μm in (a) and 2.6 μm in (b), both obtained under the same spin-coating condition of PDMS.

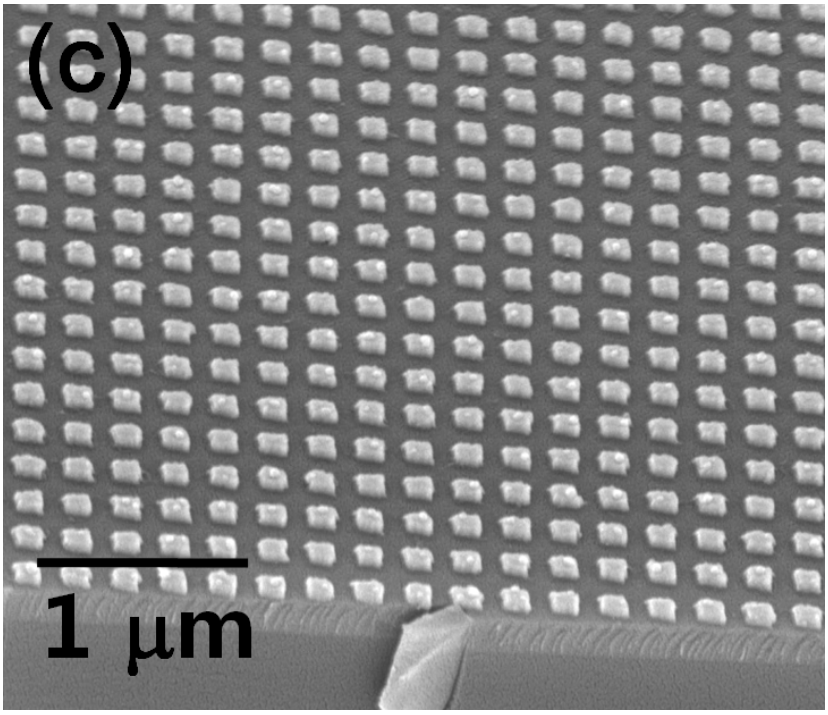

(Fig. 2.3 *continued*)

coated AuNP array. The CNT-PDMS film had 80% light extinction (mostly absorption + slight scattering). The strong pressure originates from the high optical absorption and consequent heating of the CNTs, and the large thermal expansion of the PDMS. The pressure strength could be further enhanced by growing denser CNTs to increase optical extinction, which can approach up to 99%. However, we found that the dense CNTs increase the film thickness (>5 μm) causing significant attenuation of high frequency ultrasound. We chose the composite film of 2.6 μm for measurement which has sufficiently high optical absorption (~80%) for strong pressure generation and efficient high frequency performance. The AuNP array in this measurement had 33% light extinction. Even if the AuNPs can be designed to have equal level of optical extinction to

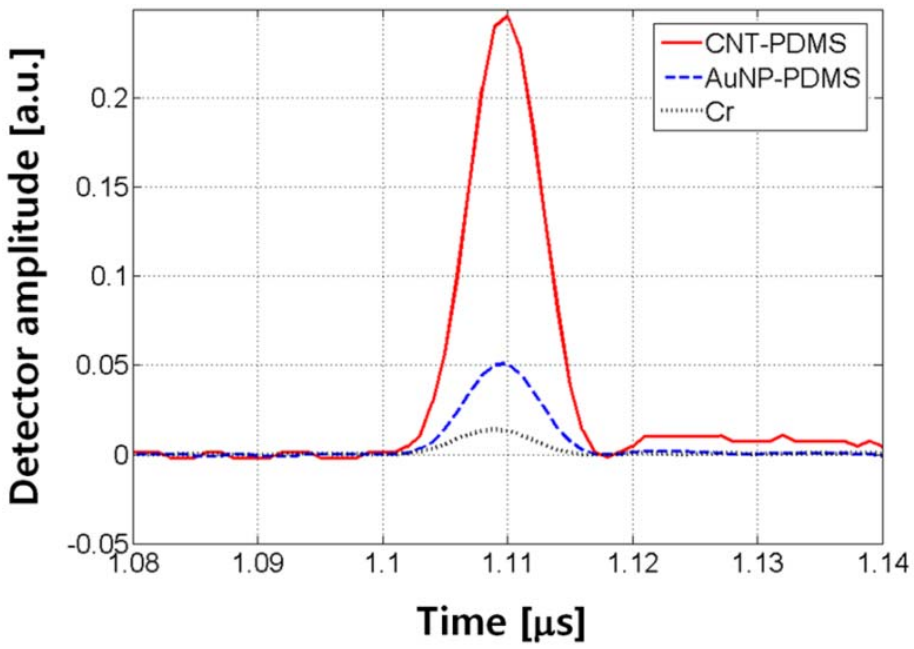

Fig. 2.4 Optoacoustic signal waveforms from Cr, AuNP coated with PDMS, and CNT coated with PDMS.

CNTs (*e.g.* nanorods [13]), the pressure will only be improved by 2.4-fold assuming a linear relationship between light extinction and pressure strength.

Next, we investigate the frequency-domain performance of the CNT-PDMS composite optoacoustic transmitter over broadband frequency. Based on the measured waveforms in Fig. 2.4, we obtained the corresponding frequency spectra as shown in Fig. 2.5(a). The spectra of three types of optoacoustic transmitters were normalized to the maximum value (low frequency asymptote, *i.e.* DC value) from the CNT-PDMS composite. It is shown that the magnitude of frequency spectrum of the CNT-PDMS composite has a 25 dB enhancement relative to the Cr reference, and this enhancement persists up to 120 MHz.

The high-frequency efficiency of each optoacoustic transmitter was also

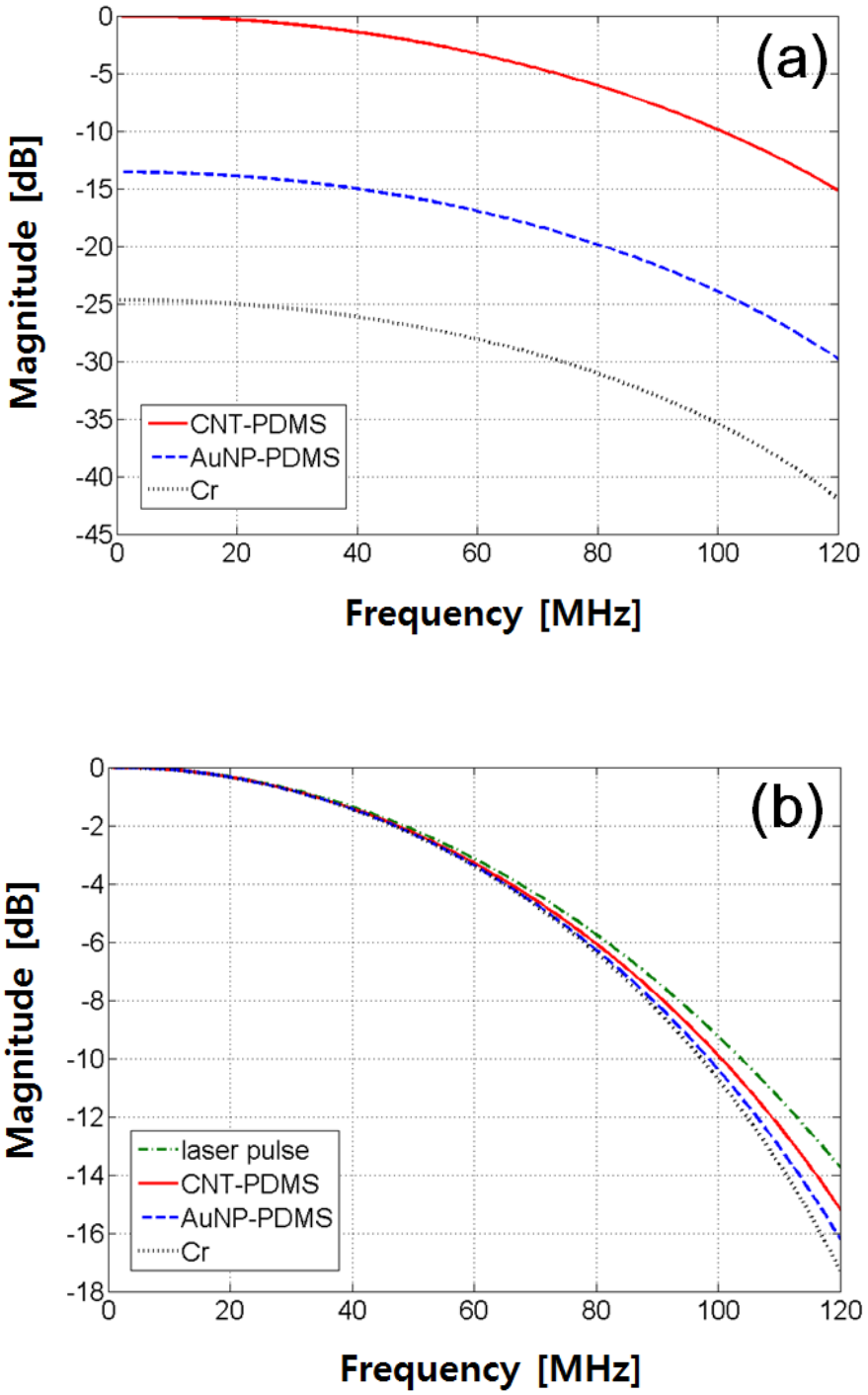

Fig. 2.5 (a) Frequency spectra for the time-domain optoacoustic waveforms of Fig. 2.4. The amplitude enhancement is clear, up to 120 MHz. (b) The same frequency spectra shown after normalization to each maximum (DC value). They are compared with the ideal spectrum of laser pulse (top trace; green color).

investigated by comparing the frequency spectra to the laser pulse spectrum, as shown in Fig. 2.5(b). Each spectrum was normalized to its DC value. The laser pulse spectrum was directly measured by the photo-detector. Ideally, the optoacoustically generated ultrasonic wave should replicate this frequency spectrum exactly. As shown in Fig. 2.5(b), the frequency spectrum of the CNT-PDMS composite closely follows that of the laser pulse. It is shown as even better than the Cr film which is already a good high frequency source, as the duration of laser pulse (6 ns) is much longer than the acoustic transit time across the film (~0.02 ns). This efficient high frequency generation from the composite is due to fast heat transfer from the nanoscale absorbers to the surrounding media.

Note that in these results, we compensated for acoustic attenuation in water for all frequency spectra. However, we did not include (1) attenuation through the PDMS layer, (2) the frequency response of microring detector, and (3) the electronic bandwidth of the photo-detector (3-dB roll off around 125 MHz). We confirmed that the acoustic attenuation in the current PDMS film without the CNTs is <0.1 dB/μm at 100 MHz, which is negligible for our evaluation. As the effect of the detector bandwidth is common to all spectra, the relative comparison among them is still valid. Also, the frequency bandwidths of the microring and photo-detector are almost flat up to 100 MHz. If we compensate these effects of (1)~(3), the optoacoustic frequency spectra will be even closer to the laser pulse spectrum.

2.3.4 Theoretical Evaluation by 1-D Layered Model

The strong optoacoustic generation in the CNT-PDMS was also confirmed by

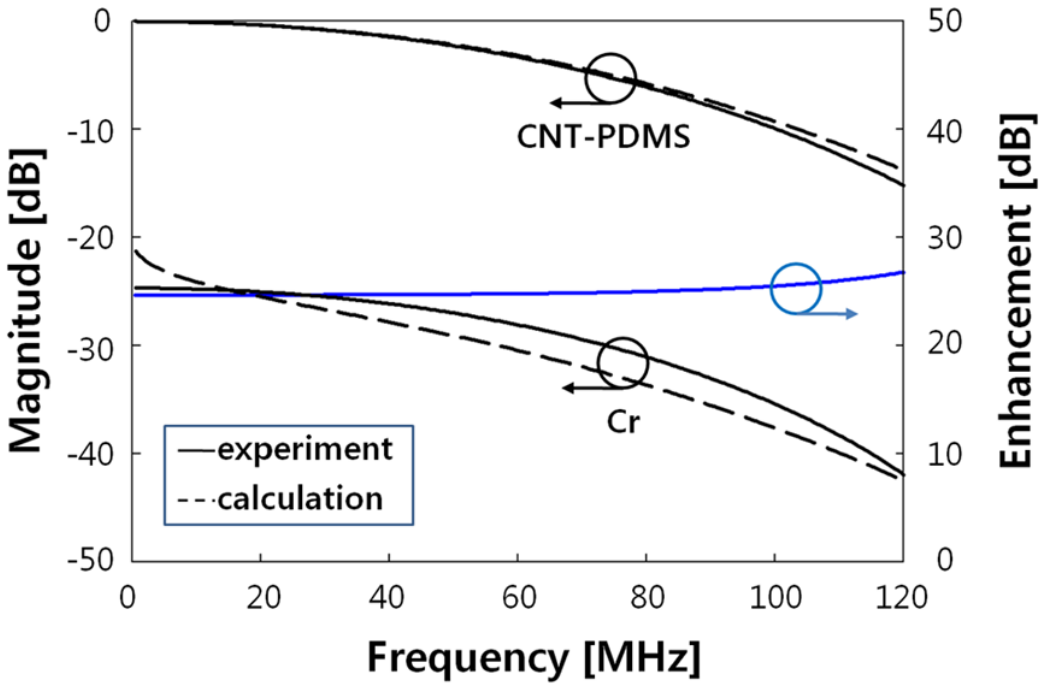

Fig. 2.6 Experimental frequency spectra (solid) compared with the calculated results (dashed) which were obtained by using the 1-D layered model, following the left axis. The difference in the experimental spectra is shown as pressure enhancement, following the right axis.

theoretical calculations. Based on a 1-D layered model for optoacoustic generation, we calculated the frequency spectra for the CNT-PDMS composite and the Cr film. For the thermophysical parameters of CNT-PDMS, we took the values of PDMS except for the optical absorption. This is based on the assumption that the acoustic property is dominated by the PDMS matrix. The assumption is reasonable because the CNT strands occupy less than a few % in volume fraction in the CNT-PDMS composite. As shown in Fig. 2.6, the calculation results match well with the experimentally obtained frequency spectra. The optoacoustic pressure enhancement near 25 dB is quite consistent over broadband frequency, which is referred to the right axis. This agreement between the

experiment and the calculation suggests that the CNT-PDMS composite behaves essentially like the polymer but with high optical absorption due to the inclusion of the CNTs.

As confirmed by both experiment and calculation, the optoacoustic frequency spectrum of the CNT-PDMS composite is almost the same as the spectrum of the laser pulse. This implies that the optoacoustic conversion process is frequency-independent. This is explained by a localized thermal volume of the optoacoustic sources [6,7]. Within the PDMS, the thermal penetration depth is less than 30 nm for the duration of the laser pulse. Then, a characteristic volume of thermoacoustic excitation is still close to that of the CNT itself. The PDMS thickness of 1~2 μm does not allow thermal waves to reach to the water-composite interface. As the water is not directly heated, the output signal spectrum is purely contributed by thermoacoustic transients of the CNTs. The laser-induced heating process is essentially instantaneous in the CNTs due to their nanoscale volume and large thermal conductivity. As a result, the optoacoustic transient from the composite should follow that of the laser pulse without distortion caused by the heating of water.

2.3.5 Comparison of Optoacoustic Generation Performance for Various Polymers as Thermal Transfer Media (Simulation)

Based on the 1-D layered model, we compared the optoacoustic conversion efficiencies (here defined as the ratio of the generated pressure to the incident laser intensity) and the output pressures from various polymers such as PDMS, poly(methyl

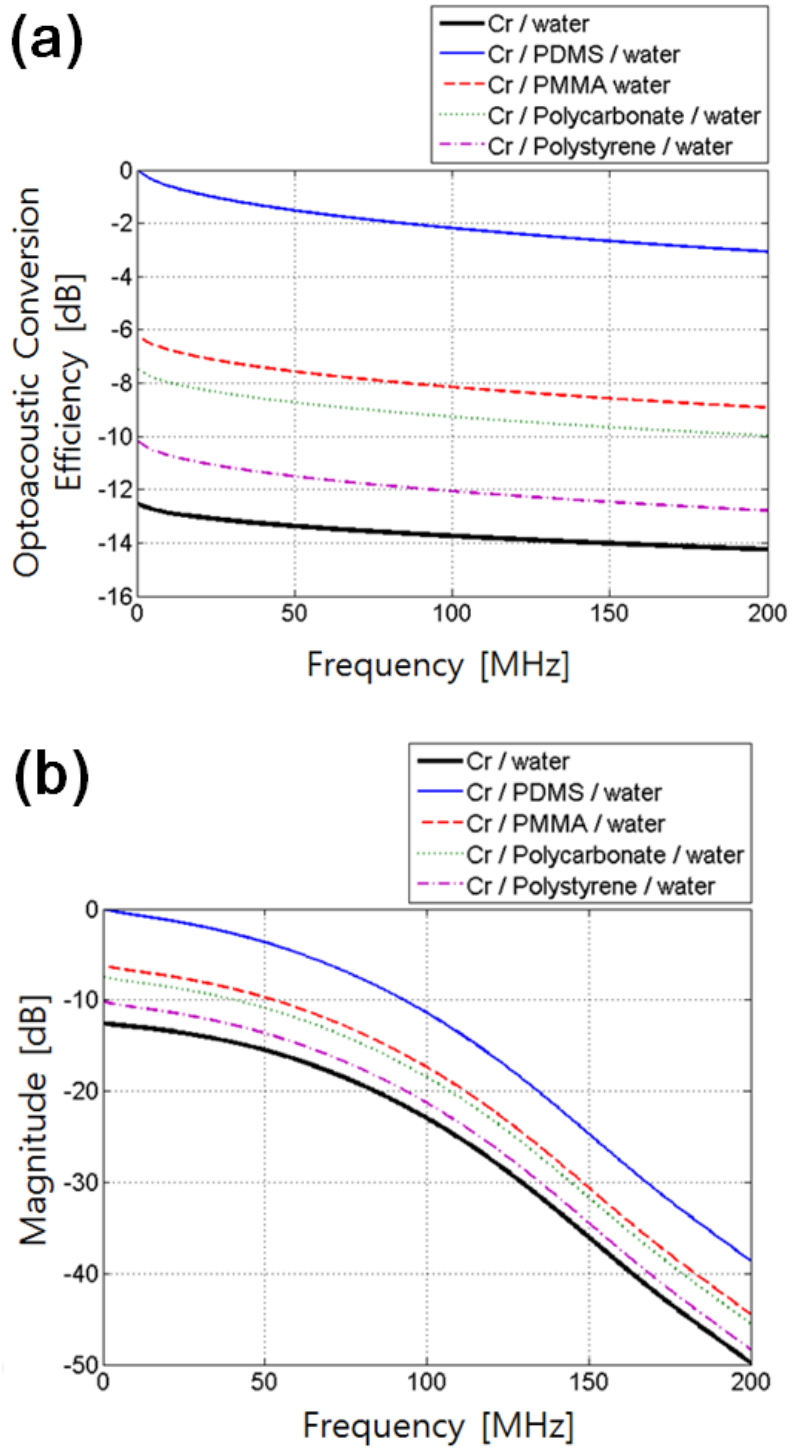

Fig. 2.7 Comparison of optoacoustic conversion efficiencies in (a) and output pressure spectra in (b) for various polymers.

methacrylate) (PMMA), polycarbonate, and polystyrene. Our calculation shows that the PDMS works as the most efficient thermal transfer medium among the compared materials (Fig. 2.7). Over the broadband frequency spectrum up to 200 MHz, the efficiency with the PDMS layer is >12 dB more efficient than the bare Cr film. Among the thermo-physical parameters included in the calculation, the thermal expansion coefficient of the PDMS was several times higher than those of other polymers, which made the elastomeric polymer, PDMS, most efficient. The PDMS has higher thermal expansion by 4.5-fold than water and >20-fold than typical metals.

2.3.6 Damage Thresholds for Laser-Induced Thermal Ablation

For strong optoacoustic generation, it is desirable to use source materials which can withstand high temperatures. A high damage threshold on the materials means that we can use high laser energies for optoacoustic generation increasing output pressure amplitudes. Fig. 2.8 shows an example of laser-induced thermal damage (Cr film exposed to 6-ns pulsed laser). The acoustic signal in Fig. 2.8(a) was measured by using a piezoelectric transducer). As the Cr film was physically detached from the substrate (shown as a bright color in Fig. 2.8(b)), the optoacoustic generation process was directly deteriorated. This caused the distortion of acoustic waveform in terms of the amplitude and the shape. We compared the damage thresholds for several optoacoustic sources: bare Cr film, Cr film coated with PDMS, AuNP coated with PDMS, and CNT with PDMS. We confirmed that the metal-based optoacoustic sources (Cr and AuNP) have similar thresholds of <20 mJ/cm^2 while the CNT-PDMS composite has much higher threshold of

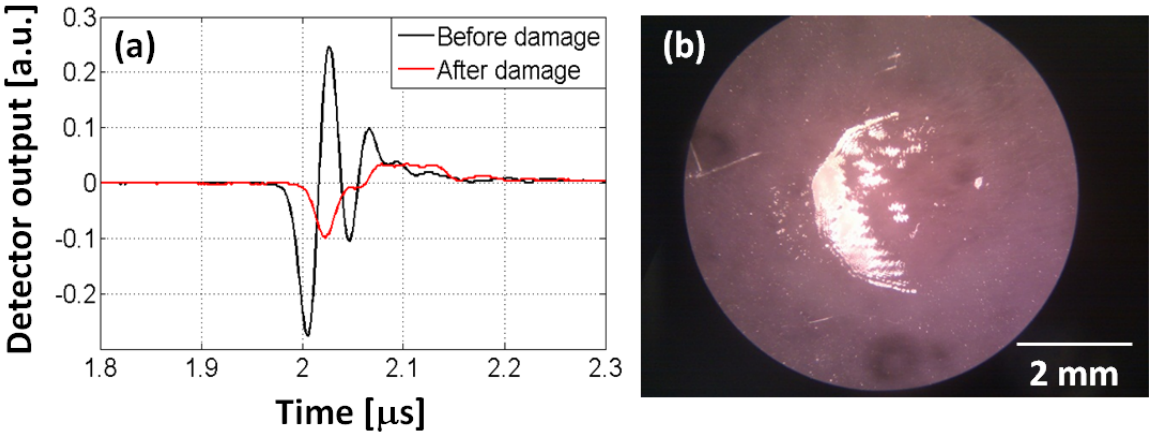

Fig. 2.8 (a) Acoustic waveform distortion and (b) physical deformation induced by high laser energy. The bare Cr film was used. The physical removal of Cr was observed through the optical microscope as shown in (b).

~170 mJ/cm^2. As the damage is determined visually through an optical microscope, we do not have a quantitative criterion (*e.g.* damage area, distortion of pressure amplitudes, and etc.). However, we note that the CNT-PDMS composite could endure the high laser energy by almost an order of magnitude for the physical damage. This is possibly associated with the adhesion issues among the CNTs, the PDMS, and the substrate. In terms of thermal damage in the polymer, the PDMS itself is very durable. Once a pre-polymer liquid of the PDMS is polymerized and then becomes thermally stable, it can withstand high temperature (>300 °C) without breakage. Therefore, the CNT-induced thermal energy can be efficiently converted into the acoustic one without losing into other forms (*e.g.* cavitation in water at 100 °C).

2.4 Gold-Coated CNT-Polymer Composite Films for Improved Optoacoustic Generation

The optoacoustic generation in the thin-film transmitters was further improved by depositing a thin-gold layer on the CNTs. The gold-coated CNTs have been used for high-contrast optoacoustic imaging [11]. It is expected that the CNT strand with the gold would form a combined nanowire structure. Therefore, depending on the gold thickness, an absorption cross-section of each CNT will be significantly enhanced. Over this primary enhancement mechanism, the gold deposition gives an additional benefit in the thin-film configuration. As the gold is deposited by an evaporation process over the CNT-grown substrate, shown in Fig. 2.9, some portion of gold is directly deposited on the substrate. This gold layer on the substrate forms a random network in the sub-micron scale. As the incident light is absorbed by the random nano-structure of the gold, the optical absorption can be further enhanced through the whole composite film. Moreover, the specular reflection of the incident light can be significantly reduced because the gold layer has the nano-structure. Being related to the frequency characteristics, we have

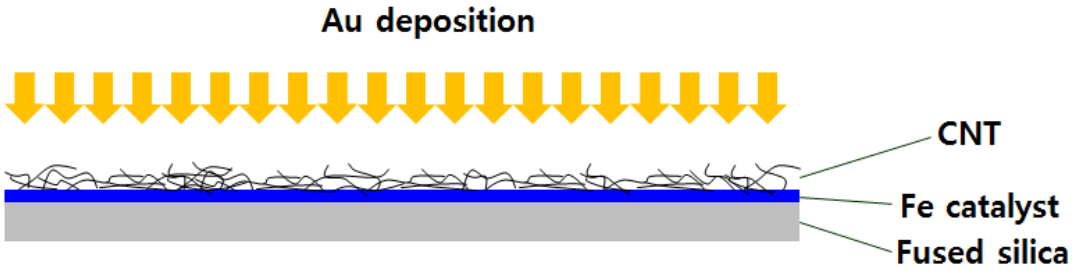

Fig. 2.9 Schematic of the gold deposition through the CNTs grown on the fused silica substrate.

another important reason why we prefer the gold deposition over the CNTs, instead of heavily growing CNTs. If the optical absorption enhancement is only a goal, we can grow the CNTs to be highly packed on the substrate. This can increase the optical extinction up to 100%. However, this also increases the thickness of composite films. This is already confirmed in Fig. 2.3. As the CNTs are grown heavily, they are distributed over several μm from the substrate boundary which effectively increases the optical penetration depth. This can broaden the temporal pulse width in the generated optoacoustic waveform and then degrade the high-frequency characteristics.

Fig. 2.10 compares two composite films with and without the gold deposition on the CNTs. In Fig. 2.10(a), it clearly shows that the gold pattern exists on the substrate which is deposited among the CNT strands (scale bar = 2 μm). Due to the sub-micron dimension, they contribute as light-absorbers reducing the mirror-like reflection by the gold layer.

The enhancement of the optical absorption was confirmed by the optical spectroscopy. Fig. 2.11(a) shows the enhancement effect at 532-nm wavelength for various composite samples with different CNT densities. For the given sample number, initially a single substrate with the grown-CNTs was divided into two pieces. We deposited the gold over one piece and then coated the PDMS (shown as filled circles in Fig. 2.11(a)) while the other piece was directly coated with the PDMS without the gold (shown as empty circles). The gold thickness was 20 nm (#1, #2, #5, and #6) and 30 nm (#3 and #4). Their enhancement in the extinction was more pronounced for the samples of the low-density CNTs. The overall spectra of optical transmission were shown in Fig. 2.11(b). Two opposite cases of low-density and high-density CNTs were compared. The

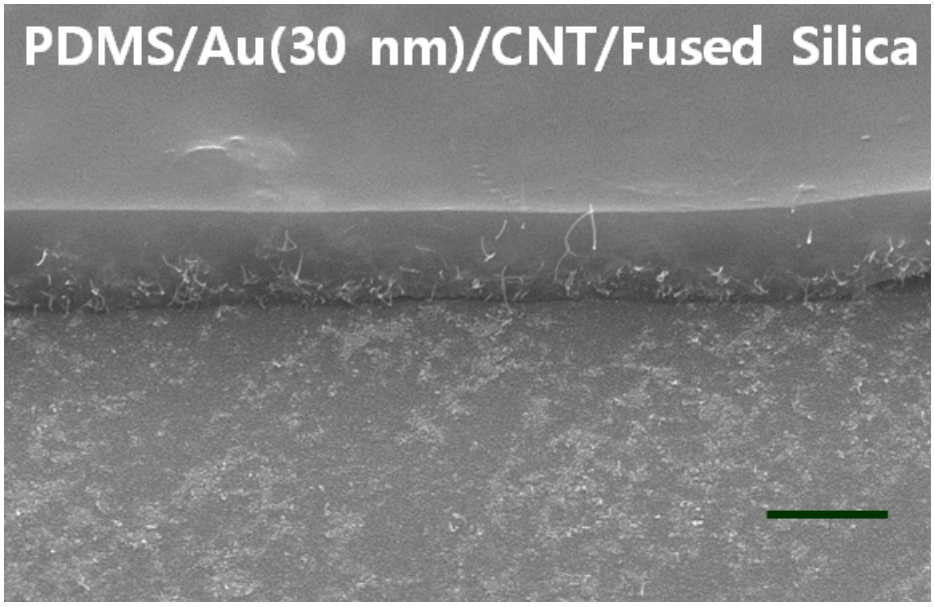

(a)

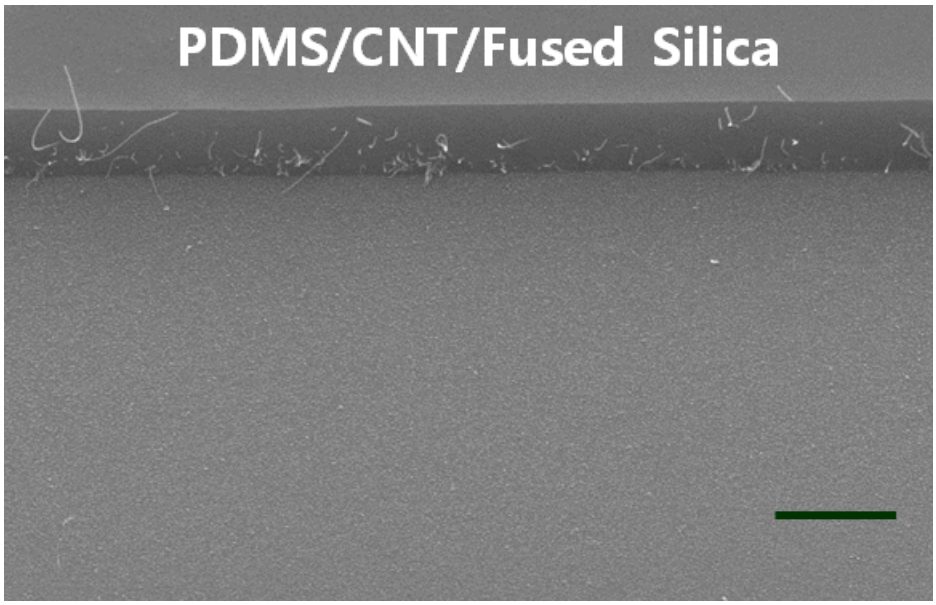

(b)

Fig. 2.10 SEM photographs of CNT-PDMS composite films. The cross-sections are shown for two cases with and without gold deposition in (a) and (b). As the gold was initially deposited through the CNT forests, they formed nano-scale islands randomly on the substrate (scale bar = 2 μm).

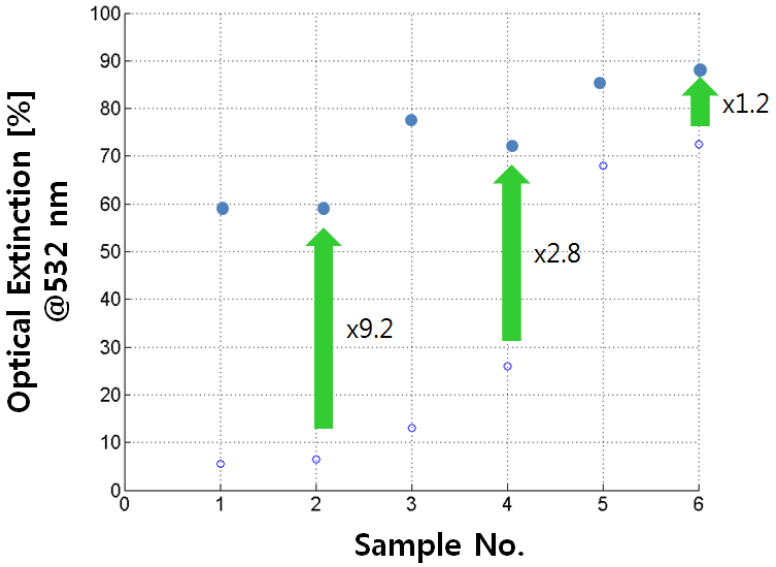

(a)

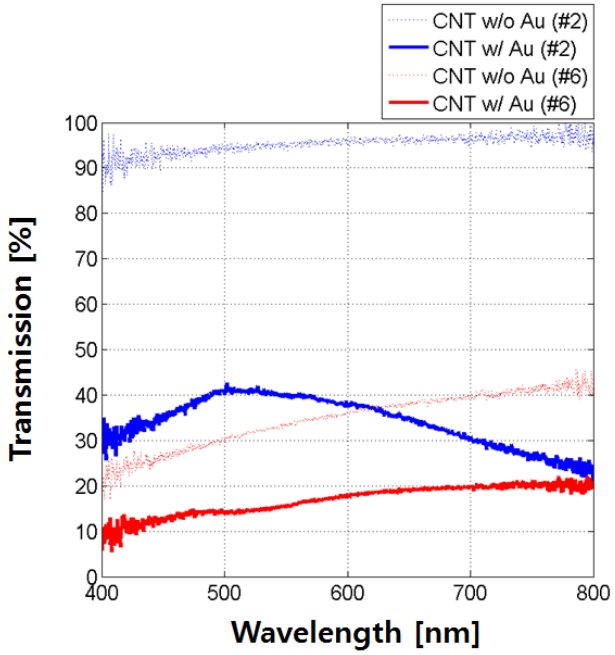

(b)

Fig. 2.11 Optical characteristics of CNT-PDMS composite films before and after gold deposition. (a) Optical extinction in six composite films. Each has an index shown in the horizontal axis (empty circle without gold; filled circle with gold). The extinction enhancement is indicated by the arrows. (b) Transmission spectra are shown in visible wavelengths. Significant enhancement is observed over broad wavelength spectra.

gold thickness is same for both samples and then leads to the identical enlargement in the cross-section of CNTs. Without the gold deposition, the MW-CNTs exhibited uniform absorption over the broad spectral range. Such behavior is maintained for the high-density CNTs after the gold deposition. The enhanced extinction in this case is primarily due to the enlarged cross-section of the CNTs. For the low-density CNTs, more amount of gold would be directly deposited onto the substrate among the CNT strands. Consequently, we could observe the distortion of the optical spectrum because of the random nano-structure of gold formed on the substrate.

For bare gold films with 30-nm thickness, about half of the incident light is transmitted and about 38% is reflected at 532-nm wavelength. However, in the gold-coated CNTs, such optical loss could be greatly reduced. The reflection was reduced to <1% for the sample #4 and <5% for the sample #3. This is due to the enlarged cross-section of the CNTs and the nano-scale gold network on the substrate. For example, the sample #3 had reflection (5%), transmission (17%), and extinction (78%). This is significant improvement, as compared to the initial extinction of 17%, just by using the low-density CNTs instead of heavily growing them.

Finally, we investigated the optoacoustic pressure amplitudes. The measurement setup of Fig. 2.2 was used. Fig. 2.12(a) and (b) compare the pressure waveforms with and without the gold in the low-density sample (#2) and the high-density (#6). Similarly with the optical absorption characteristics, the relative enhancement in the pressure was more pronounced in the low-density sample (#2). The linear behavior between the pressure amplitudes and the optical extinction was confirmed in Fig. 2.12(c) by taking the peak amplitudes from Fig. 2.12(a) and (b). The gold-coating approach is more effective for the

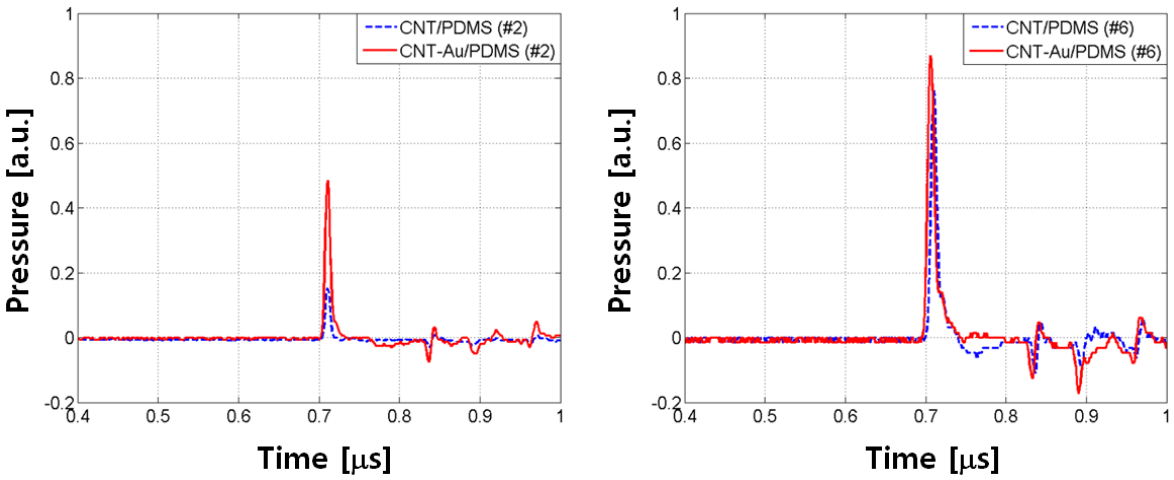

(a) (b)

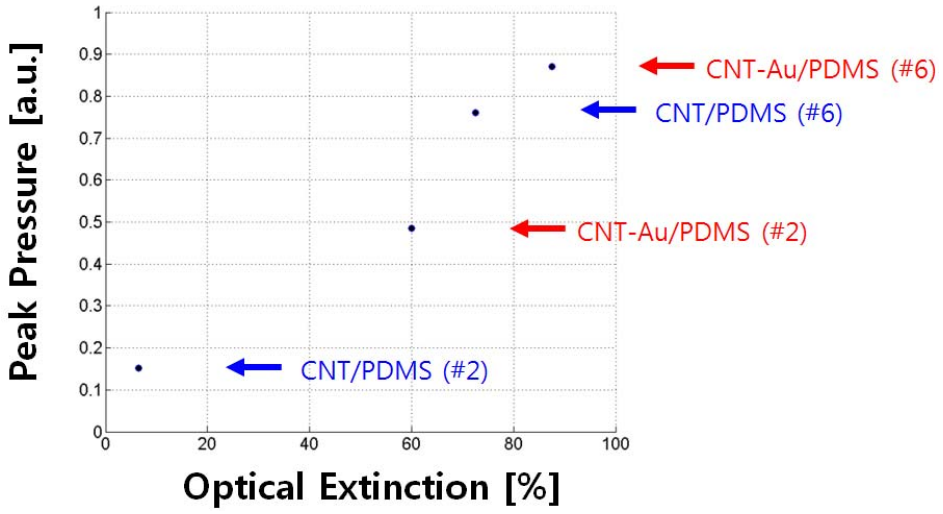

(c)

Fig. 2.12 Pressure enhancement in the gold-deposited CNT-polymer composite films. (a) Enhancement result in the sample #2 (initially, low optical extinction). (b) Enhancement in the sample #6 (initially, high extinction). (b) Linear behavior between the pressure amplitudes and the optical extinction. The four dots are taken from the peak amplitudes shown in (a) and (b).

CNTs initially grown in low density. But we note that this can be applied for any densities of CNTs to boost the output optoacoustic pressure simply by depositing the gold on the

CNTs.

2.5 Conclusion

We demonstrated the thin-film optoacoustic transmitters by using CNT-polymer composite films capable of generating strong and high frequency ultrasound. The CNT-PDMS composite film generated 18-fold stronger pressure than that of the Cr film case and 5-fold stronger than that of the AuNP composite with the same polymer. This enhancement persisted over a broadband frequency range up to 120 MHz, which was verified by the analytical modeling. We could further enhance the pressure amplitudes by depositing the thin gold of 20~30 nm over the as-grown CNT forest. The enhancement is due to the increased absorption cross-section in the CNTs and the gold layer directly formed on the substrate.

References

[1] R. J. von Gutfeld and H. F. Budd, Appl. Phys. Lett. 34, 617 (1979).
[2] T. Buma, M. Spisar, and M. O'Donnell, Appl. Phys. Lett. 79, 548 (2001).
[3] Y. Hou, S. Ashkenazi, S.-W. Huang, and M. O'Donnell, IEEE Trans. Ultrason. Ferroelectr. Freq. Control 54(3), 682 (2007).
[4] Y. Hou, J.-S. Kim, S. Ashkenazi, M. O'Donnell, and L. J. Guo, Appl. Phys. Lett. 89, 093901 (2006).
[5] Y. Hou, J.-S. Kim, S. Ashkenazi, S.-W. Huang, L. J. Guo, and M. O'Donnell, Appl. Phys. Lett. 91, 073507 (2007).

[6] D. S.Kopylova, I. M. Pelivanov, N. B. Podymova, and A. A. Karabutov, Acoust. Phys. 54(6), 783 (2008).
[7] I. M. Pelivanov, D. S.Kopylova, N. B. Podymova, and A. A. Karabutov, J. Appl. Phys. 106, 013507 (2009).
[8] V. E. Gusev and A. A. Karabutov, Laser Optoacoustics, AIP Press, New York, Chap. 3 (1993).
[9] J. A. Copland, M. Eghtedari, V. L. Popov, N. Kotov, N. Mamedova, M. Motamedi, and A. A. Oraevsky, Mol. Imaging Biol. 6, 341 (2004).
[10] P. M. Ajayan, M. Terrones, A. de la Guardia, V. Huc, N. Grobert, B. Q. Wei, H. Lezec, G. Ramanath, and T. W. Ebbesen, Science 296, 705 (2002).
[11] A. de la Zerda, C. Zavaleta, S. Keren, S. Vaithilingam, S. Bodapati, Z. Liu, J. Levi, B. R. Smith, T.-J. Ma, O. Oralkan, Z. Cheng, X. Chen, H. Dai, B. T. Khuri-Yakub, and S. S. Gambhir, Nature Nanotech. 3, 557 (2008).
[12] A. L. McKenzie, Phys. Med. Biol. 35, 1175 (1990).
[13] A. A. Oraevsky, Photoacoustic Imaging and Spectroscopy, edited by Lihong V. Wang, CRC Press, Boca Raton, Chap. 30 (2009).
[14] S. Berber, Y.-K. Kwon, and D. Tomanek, Phys. Rev. Lett. 84, 4613 (2000).
[15] G. J. Diebold. T. Sun, and M. I. Khan, Phys. Rev. Lett. 67, 3384 (1991).
[16] C. Y. Chao, S. Ashkenazi, S.-W. Huang, M. O'Donnel, and L. J. Guo, IEEE Trans. Ultrason., Ferroelect., Freq. Contr. 54, 957 (2007).
[17] A. Maxwell, S.-W. Huang, T. Ling, J.-S. Kim, S. Ashkenazi, and L. J. Guo, IEEE J. Select. Topics Quantum Electron. 14, 191 (2008).
[18] S.-W. Huang, S.-L. Chen, T. Ling, A. Maxwell, M. O'Donnell, L. J. Guo, and S. Ashkenazi, Appl. Phys. Lett. 93, 113501 (2008).
[19] C. Pina-Hernandez, J.-S. Kim, and L. J. Guo, Adv. Mater. 19, 1222 (2007).
[20] M.-G. Kang and L. J. Guo, J. Vac. Sci. Technol. B 26(6), 2421 (2008).

Chapter III

Optical Generation of High-Frequency Focused Ultrasound

3.1 Introduction

Focused ultrasound has made a wide range of impacts in modern acoustics because of its nonlinear characteristics [1] and secondary effects such as acoustic cavitation and heat deposition [2-4]. These have inspired emerging interests over broad disciplines in terms of scientific understanding of physical mechanisms [5,6], device physics and engineering for acoustic focusing [7,8], and biomedical applications both *in vivo* and *in vitro* [9-20]. As a non-invasive modality, the focused ultrasound and its induced effects have already come out with remarkable results in cancer therapy [9-11], intra-membrane drug delivery (*e.g.* blood-brain barrier opening) [12-15], brain activity modulation [16,17], kidney-stone fragmentation [18,19], and thrombolysis [20]. These could be realized as the nonlinear induced effects are spatially localized by high-amplitude or high-intensity focused ultrasound (HIFU).

In order to generate such strong ultrasound, piezoelectric transducers have been mostly used as ultrasonic transmitters. While they can generate sufficient pressure amplitudes, their focal spots have bulky dimensions (a few mm in diameter and several to

tens of mm in depth) because of low operation frequency ranges typically over a few MHz [10]. This is not proper for high-accuracy applications which minimize potential damages over regions surrounding the focal volumes. Better localization will be achieved if the pressure can be tightly focused using much higher frequency ultrasound. Moreover, this may open new opportunities to explore microscopic interactions of the nonlinear ultrasound with individual cells and a single layer of tissues. Moreover, since the traditional transducers have large sizes and require complex electrical connections for impedance matching and high driving voltages, it is difficult to bring them and deliver such strong pressure directly into specific regions *in vivo*. In this sense, it is valuable to develop new modalities to generate therapeutic ultrasound in a compact dimension of several mm which can fit to stents or optical fibers.

Optoacoustic generation of ultrasound has an advantage in obtaining high-frequency acoustic waves. As the mechanism is based on light-absorption and thermo-elastic volume deformation [21-25] rather than based on thickness-dependent resonance, acoustic frequency spectra are primarily determined by frequency characteristics of excitation light sources. However, weak output pressure has been a major drawback in optoacoustic transmitters. This is due to poor optoacoustic energy conversion process which is relevant to optical and thermal properties of the source materials. The weak pressure amplitude can be compensated by externally increasing the excitation laser energies. But these energies are fairly limited not to cause thermal damages on the optoacoustic sources. Due to these limitations, the optoacoustic generation could not achieve high amplitudes enough for the nonlinear acoustic effects.

We have significantly enhanced the optoacoustic energy conversion efficiency by

using CNTs and gold-coated CNTs. The pressure amplitude could be 18-fold higher than reference metal films, still maintaining all the high-frequency characteristics of original laser pulses [26]. Here, we adopted MW-CNT-polymer composite films again to generate strong optoacoustic pressure. More importantly, we generated and simultaneously focused the output pressure by locating the nano-composite films on concave surfaces. In this manner, we introduce laser-generated focused ultrasound (LGFU) which can deliver unprecedented optoacoustic pressure on both positive (>50 MPa) and negative (>20 MPa) peaks. Interestingly, these amplitudes were strong enough to involve formation of pronounced shock waves and acoustic cavitation as the negative peak pressure goes far beyond a cavitation threshold, which has not been achieved so far. Due to the high-frequency nature over tens of MHz, we could demonstrate tight focal spots of 75 μm in lateral and 400 μm in axial directions at a focal distance of 5.5 mm. The shock-wave and acoustic cavitation behaviors were experimentally verified in several ways by monitoring micro-bubbles and performing lithotripsy. Collapse times and physical sizes of the bubbles were also determined. We note that the focusing performance of the LGFU is not limited by the above values because the current lens specification is an example as one of the possible designs. We discuss potential impacts of the LGFU providing possible variations in the lens design and the excitation laser.

3.2 Lens Characteristics: Theoretical Estimation of Focal Gain and Shock Parameter

3.2.1 Focal Gain

High-frequency availability is a key feature of the optoacoustic generation. This enables high focal gain and short distance for shock formation in our configurations. If we define the focal gain in spherical lenses as a ratio of the pressure at the focus to that on the spherical surface where the source layer is located, a gain G for a given harmonic frequency component can be represented as [27],

$$G = \frac{2\pi f}{c_0} r\left(1 - \sqrt{1 - \frac{1}{4 f_N{}^2}}\right) \tag{3.1}$$

where f, c_o, r, and f_N are the acoustic frequency, the ambient sound speed, the radius of curvature, and the f-number which is a ratio of the radius of curvature to the lens diameter. For acoustic focusing, we used concave substrates, basically optical lenses made of fused silica, where the CNTs were uniformly and densely grown. As the CNTs are grown in a gas phase, optoacoustic transmitters with arbitrary geometries can be prepared in principle [28]. Therefore, it is easy to make highly curved transmitters even in the order of several millimeters in the lens diameter. We fabricated various dimensions of the CNT-grown lenses with focal lengths from 4.7 mm to 18 mm and diameters from 6 mm to 21 mm. Among these, here we chose two specifications for optoacoustic focusing experiment. The first one has 5.5 mm in the radius of curvature and 6 mm in the diameter (named as type I, f_N = 0.92), and the second has 11.46 mm and 12 mm (type II, f_N = 0.96).

As we compare the gain with those of the common HIFU transducers, the optoacoustic transmitters have significantly higher gains due to the factors of high frequency and low *f*-number. In the current lens design, the gain enhancement by the high frequency is compromised to some extent by realizing small-dimension devices. However, an order of magnitude enhancement can be still made by low *f*-numbers ($f_N < 1$) as compared to high values ($f_N > 3$) of the usual piezoelectric transducers. We estimated the geometrical gains, taking a frequency-dependent attenuation into consideration. The gains for two examples are shown in Fig. 3.1. These correspond to the optoacoustic focusing lens (type I) and an example of the conventional low-frequency HIFU transducer which has r = 55 mm and *f*-number = 2.5. This means that the lens diameter would be ~29λ for a center frequency of 2 MHz, which is reasonable. The calculation result suggests that the optoacoustic configuration has higher gains over most of the frequency ranges. In the piezoelectric transducer case, the gain over the high frequency range (>20 MHz) is severely compromised by the acoustic attenuation in water, but the gain in the optoacoustic configuration is maintained over a broad range of frequency due to the short focal distance ($\approx r$). This shows that the optoacoustic transmitter platform is suitable for high-frequency focusing. Moreover, the low *f*-number is an attractive feature which cannot be easily achieved in the conventional piezoelectric transducers. However, although the theoretical gain in the optoacoustic transmitter is estimated as large as >70-fold for >20 MHz frequency range, this may be reduced during device fabrication process. Possible distortion in the focusing alignment can be incorporated due to non-uniform polymer thickness on the lens. As we spin-coat the polymer on the curved surface, the

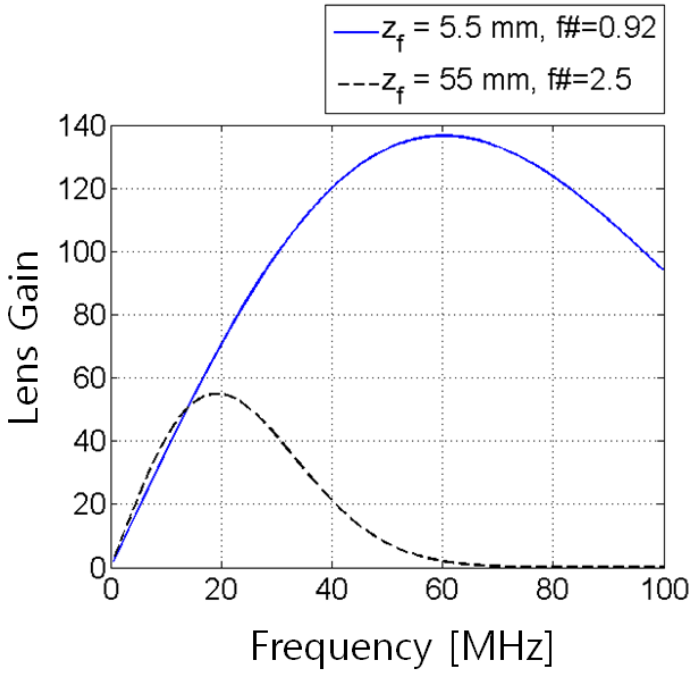

Fig. 3.1 Comparison of geometrical gain of the lens. The frequency-dependent gains were calculated for two cases: the type I optoacoustic focusing lens (solid) and an example of the conventional low-frequency HIFU transducer (dotted).

thickness may be slightly varied over the position on the lens (thick at the center and thin around the edge). Such non-uniformity is tolerable and somewhat reduced by increasing the spin-coating speed because the overall polymer thickness becomes thin. The polymer thickness could be adjusted from several μm (<3000 r.p.m.) down to a few μm (>6000 r.p.m.).

3.2.2 Shock Parameter

In the LGFU, high-amplitude pressure is obtained at the focal spot. Such strong pressure in the positive phase makes the positive phase move faster than the ambient

sound speed c_0 in water. This causes the waveform distortion as a form of sudden increase of the pressure field in time-domain [1], which becomes a shock wave. In physical sense, the shock is formed where $\frac{\partial v}{\partial t} \to \infty$ (v is the vibration velocity). Since the solutions of the wave equations for pressure, velocity, and velocity potential have identical form of $f\left(t - \frac{x}{c_0 + \beta v}\right)$ where β is nonlinearity, the time-derivative of the vibration velocity can be represented as

$$\frac{\partial v}{\partial t} = \frac{f'}{1 - \beta x f' / (c_0 + \beta v)^2} \tag{3.2}$$

which includes the time-derivative of the function *f*. Under the condition of $\frac{\partial v}{\partial t} \to \infty$, we get the distance $x = \frac{(c_0 + \beta v)^2}{\beta f'}$. As the nonlinearly induced vibration speed βv is much smaller than c_0, we obtain the shock formation distance as $x = \bar{x} \approx \frac{c_0^{\,2}}{\beta f'}$. For $x < \bar{x}$, the shock waveform is not evolved significantly. This corresponds to a pre-shock regime. For $x > \bar{x}$, the waveform has the shock-induced distortion. As the shock is further evolved for $x >> \bar{x}$, the acoustic energy becomes rapidly dissipated at the front. In this regime, the pressure amplitude is not increased any more (*i.e.* acoustic saturation).

In the LGFU, the shock wave can be rapidly evolved in short propagation distances, compared to the traditional transducer case. This can be quantified by a large

shock parameter. A normalized shock parameter $\sigma(z) = \frac{x}{\bar{x}}$ for a given distance *z* along the axial direction has been derived for spherical focusing configurations, which is represented as [6]

$$\sigma(z) = 2\pi \frac{\beta f p_0 z_f}{\rho c_0^{\,3}} \frac{G}{\sqrt{G^2 - 1}} \ln\left(G + \sqrt{G^2 - 1}\right)\left(R + \sqrt{1 + R^2}\right) \tag{3.3}$$

where p_o and z_f are the surface pressure and the focal distance. The large values of σ mean strong distortion in acoustic signal waveforms for a given propagation distance *z* from the lens surface. In general, σ = 1 is regarded as a beginning point of shock distortion. We estimated the normalized shock parameter for the optoacoustic lens condition of z_f = 5.5 mm (we assume $z_f \approx r$) and p_0 = 1 MPa. Fig. 3.2 shows the calculation results for several harmonic frequency components. The shock distortion begins (σ = 1) at 4.7-mm distance from the lens surface for 15-MHz harmonic frequency and at 3.4 mm for 30 MHz. The strong shock distortion for these high-frequency components is contrasted to the other low-frequency conditions which are in the pre-shock regime in this short distance. In the LGFU, the shock formation is possible even in shorter focal distances (3~4 mm). Similar focal gains can be obtained together with low acoustic attenuation over the short propagation which is favorable for the high-frequency components. The short distance for shock formation is one of the main features in the LGFU because of high focusing gains, high surface pressure, and rapid temporal transition of the source function [6].

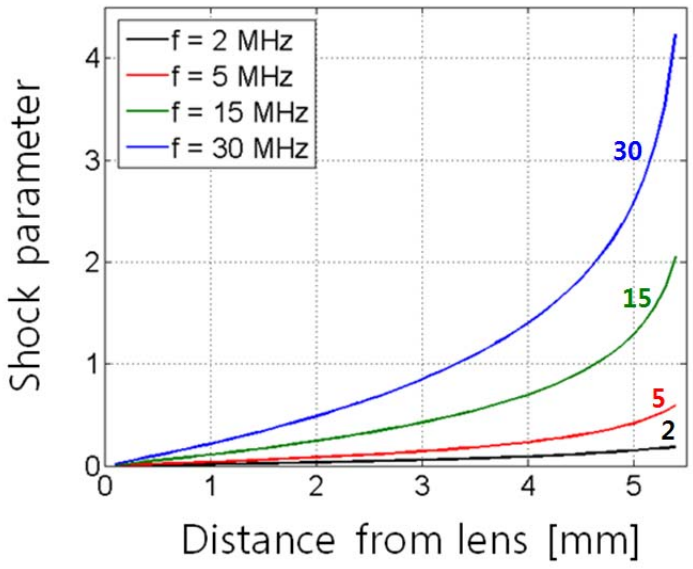

Fig. 3.2 Shock parameters calculated for several frequency components. In the calculation, we assume the focusing geometry of the type I lens. The shock distortion is expected where the shock parameters are higher than 1.

3.3 Optoacoustic Generation of High-Amplitude and High-Frequency Focused Ultrasound

Pressure amplitudes of the nonlinear regime could be achieved in the optoacoustic focusing due to efficient optoacoustic source materials and unique lens designs enabling high geometrical gain. In the CNT-polymer composite film, the efficient optoacoustic energy conversion is primarily due to high optical absorption and low material density of the CNT, and high thermal expansion coefficient of the surrounding elastomeric polymer [26]. We confirmed that a laser damage threshold to induce thermal ablation was 9-fold higher in the CNT-polymer composite as compared to common metal films. This is significant to increase available laser energies and maximize pressure

amplitudes.

3.3.1 Experimental Configurations

Fig. 3.3(a) shows the experimental schematic used for generation and characterization of the focused ultrasound. A 6-ns pulsed laser was used with a repetition rate of 20 Hz. The laser beam initially has 5 mm in diameter. The laser beam was first attenuated by the neutral density filters and then expanded (×5). The collimated beam was illuminated to the transparent (planar) side of the lens. The focused acoustic waves were detected by the single-mode fiber-optic hydrophone (6-μm core and 125-μm cladding in diameters) positioned at the focal zone. Both the lens and the optical fiber were mounted on 3-dimensional motion stages for accurate alignment. The optical output was 3-dB coupled and transmitted to the photodetector. The photodetector has a broad electronic bandwidth over 75 MHz. Detailed hydrophone operation is similar with the reported elsewhere [29]. Both dc and ac signals were monitored by using a digital oscilloscope (WaveSurfer 432, LeCroy, Chestnut Ridge, NY). The waveforms in Fig. 3.4(a) are the result of averaging 20 signal traces in time-domain. For the passive detection measurement of the acoustic cavitation (Fig. 3.3(b)), we used a separate piezoelectric transducer with a center frequency of 15 MHz (Model V319, Panametrics, Waltham, MA). The transducer was oriented in perpendicular to the fiber hydrophone as shown in Fig. 3.4(b). The transducer output was directly recorded by using the digital oscilloscope.

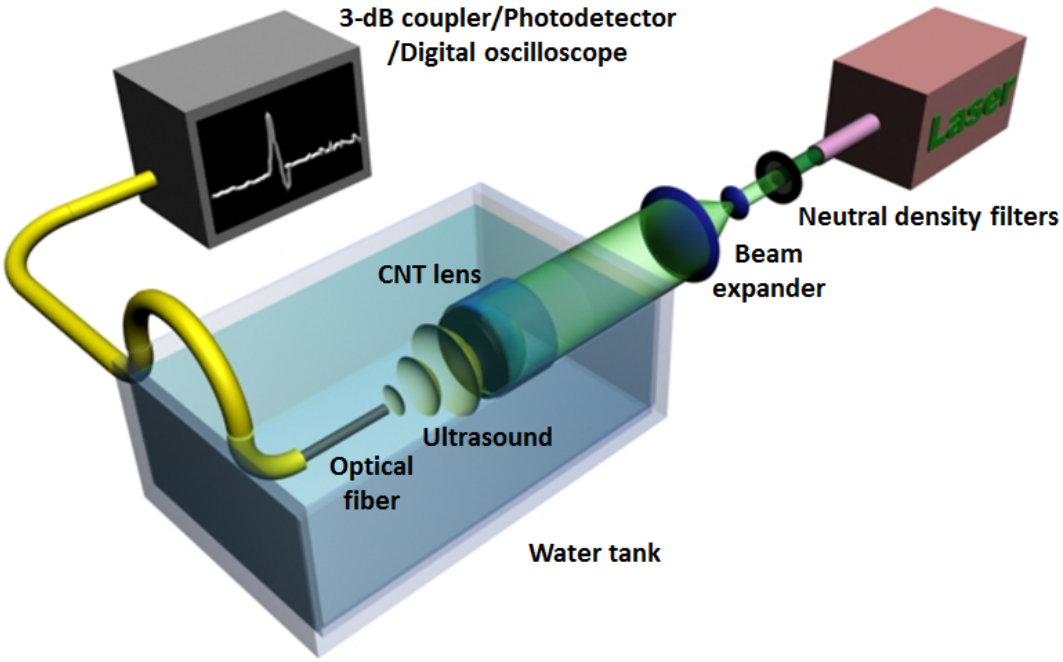

(a)

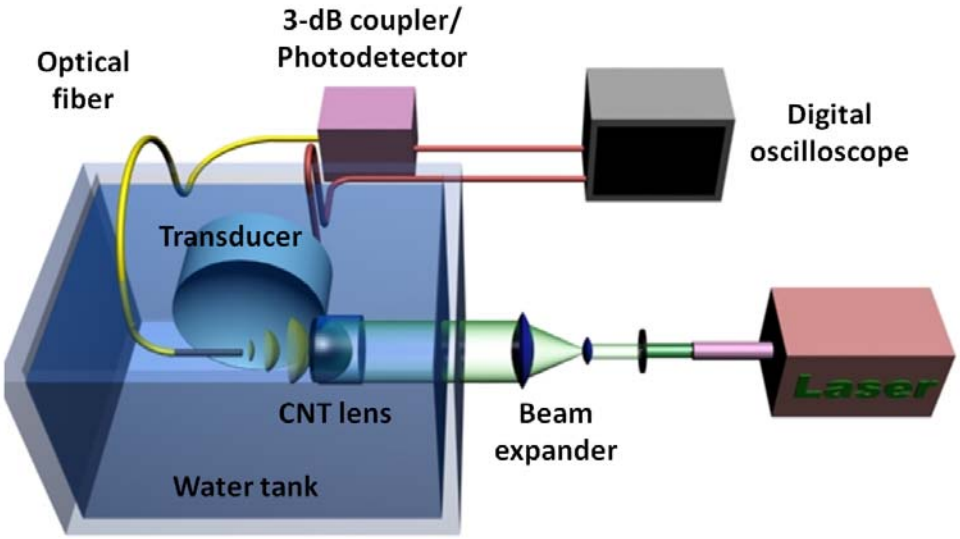

(b)

Fig. 3.3 Experimental schematics used for the LGFU characterization. The configuration shown in (a) was used to characterize the general profiles of LGFU. The configuration shown in (b) includes the additional transducer used to sensitively detect acoustic cavitation signal from the focal zone.

3.3.2 Characterization of Temporal and Spatial Profiles at Lens Focus

The experimental results of the LGFU are shown in Fig. 3.5. These results were obtained from the type I lens. In a far-field regime, the acoustic waveform is close to a time-derivative of the original excitation source (*i.e.* Gaussian laser pulse) [30], shown as the bipolar shape in Fig. 3.4(a). We observed asymmetric waveforms with pronounced positive amplitudes around the focal point ($z = f = 5.5$ mm) due to shock wave evolution. The waveform is compared with the relatively symmetric one which was measured in front of the focal plane ($z = f–0.3 = 5.2$ mm). Due to the shock evolution, the acoustic energy transition to higher frequency components was observed (Fig. 3.4(b)).

A sensitivity of the fiber hydrophone was confirmed by using a calibrated piezoelectric transducer which has a focused design and a center frequency of 3.5 MHz. The estimated value was 4.5 mV/MPa at this frequency. However, transfer functions of the fiber-optic hydrophone depend on the acoustic frequency which is primarily due to acoustic diffraction. This causes the hydrophone to give 1.5-fold enhanced output at 3.5 MHz and 2-fold above 10 MHz [7, 31]. In this regard, the hydrophone output may be over-estimated by ~30%. Whereas, the transfer function is gradually attenuated due to electronic bandwidth issues over the high-frequency range. This will reduce the high-frequency output to lower than 2-fold. In a conservative manner, we use 5.85 mV/MPa as a nominal value of the fiber sensitivity (~4.5 mV × 30%). This gives pressure amplitudes without the enhancement effect over the high-frequency range. For example, the positive peak amplitude in Fig. 3.4(a) corresponds to ~22 MPa and the negative one ~10 MPa at the focus, according to this sensitivity.

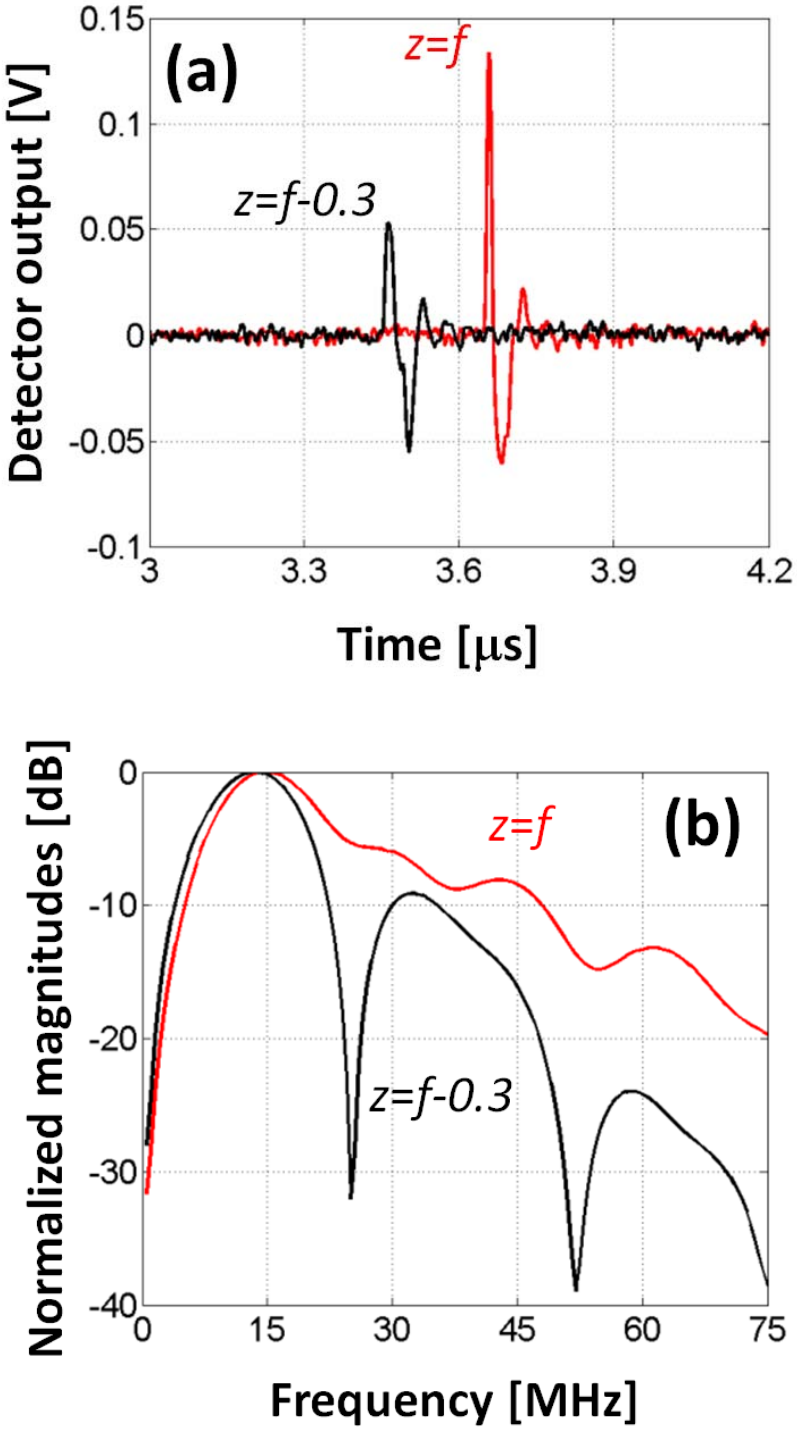

Fig. 3.4 Experimental results of the LGFU. (a) Time-domain waveforms at the focal point (z = f) and slightly in front of the focal point (z = f-0.3) measured by the fiber-optic hydrophone. (b) Corresponding frequency spectra.

The pressure amplitudes could be increased with the excitation laser energy. For the positive peaks shown in Fig. 3.5, the amplitudes were saturated at high laser energy level to ~340 mV (or ~58 MPa). In the high laser energy regime, the shock wave formation at the front is balanced by quick energy dissipation into heat [27]. For the negative amplitudes, the acoustic cavitation was involved when the laser energy was higher than 14 mJ/pulse. In this laser energy, the negative pressure amplitude was ~13.7 MPa, corresponding to a cavitation threshold. For the over-threshold regime, the negative peaks could not be accurately determined as the signal waveform was distorted by the cavitation. However, higher than 25 MPa in the negative peak would be reached over the high laser energy if the pressure amplitude is extrapolated in Fig. 3.5. We note that all these high-amplitudes in both polarities were generated just by using the small lens dimension of 6 mm in diameter. For the type II lens with 2-fold larger diameter, the cavitation threshold was reduced to <10 mJ/pulse in the laser energy. This is due to an increased focal gain from the type II lens. While the current results show the maximum amplitude of ~58 MPa in the type I lens of 6-mm diameter, the optoacoustic focusing approach would easily allow much stronger amplitudes by increasing the lens sizes.

The measured frequency spectra were significantly affected by the detector bandwidth. The pressure field at the detector is distorted by acoustic diffraction effects due to the finite dimension of the optical fiber and the possible tilt angles between the fiber direction and the lens axis [31]. The fiber diameter of 125 μm enforces the detector transfer function to have its peak response around 12 MHz. In our measurement, both frequency spectra in Fig. 3.4(b) show the first peaks around ~15 MHz (this was increased to 16~17 MHz with larger pressure amplitudes). Therefore, before the application of the

detector transfer function, the frequency spectra of the focused ultrasound originally have the frequency peaks higher than 15~17 MHz. This will be discussed again in the following section, being related to the focal spot sizes. In the frequency spectra of Fig. 3.4(b), we note that the higher order peaks also appear up to the fifth order. The peak frequencies agreed with nonlinear harmonic components of $2f_C$, $3f_C$, $4f_C$, and $5f_C$ for the first-order center, f_C = 15 MHz.

The spatial profiles of the LGFU are shown in Fig. 3.6 (focal plane) and Fig. 3.7 (axial direction of the lens). The full-width half-maximum (FWHM) of the positive peak profile was 75 μm in the lateral and 400 μm in the axial directions. The width of the negative peak profile was broader than the positive one. This is because the peaks in the

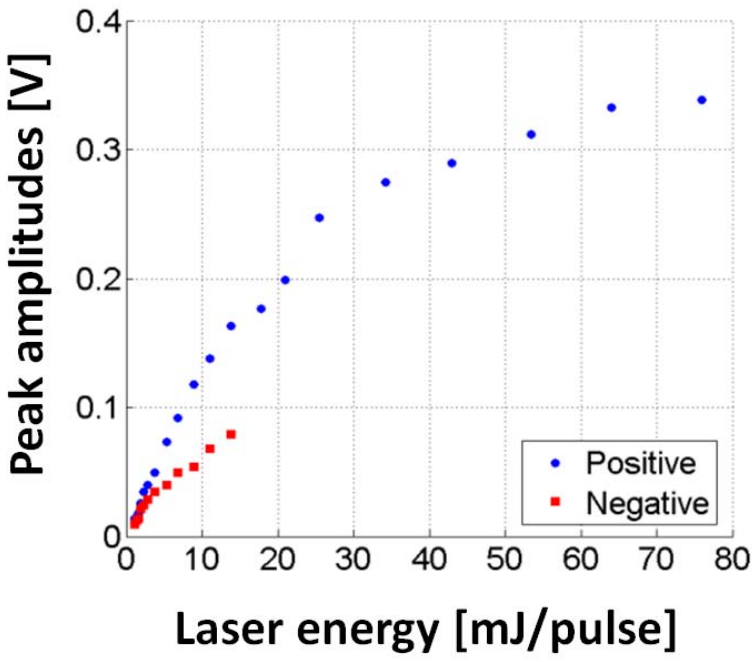

Fig. 3.5 Laser energy versus pressure amplitudes. The pressure value can be obtained by using the detector sensitivity (~5.85 mV/MPa, conservatively defined; detail explanation in the main text).

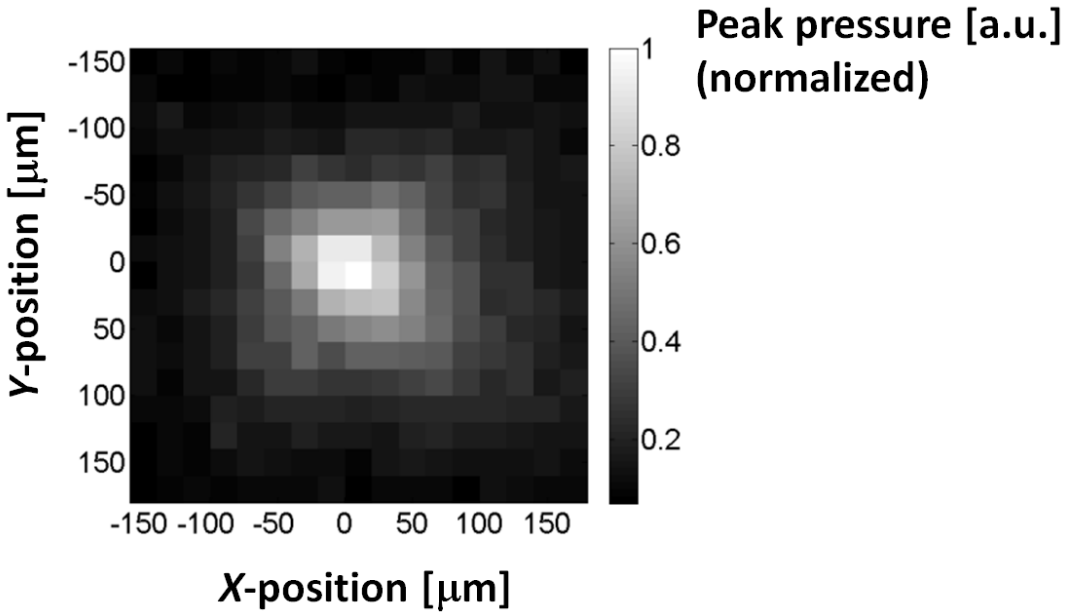

Fig. 3.6 Spatial profile at the focal plane which is characterized by the positive peak pressure (scanning step or interval between pixels = 20 μm).

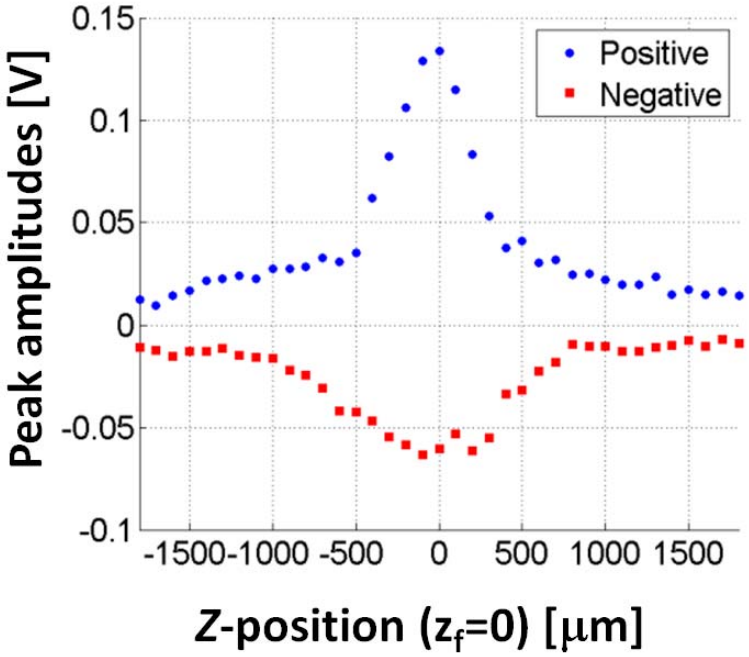

Fig. 3.7 Spatial profiles along the axial direction which are characterized by both positive and negative peaks. The *z*-position is relative to the focal distance z_f (scanning step or interval between dots = 100 μm).

positive phases are determined by the shock waves which have sharp leading profiles and therefore higher frequency components than the ones in the negative phases.

The focal width can be intuitively associated with the acoustic wavelength and frequency. As the acoustic wavelength becomes shorter in higher frequency, we can achieve tight focal spots in space. In Fraunhofer diffraction theory, a finite circular aperture gives limitation on the focal spot dimension. For the pressure field, the focal diameter D defined at the FWHM can be represented as

$$D \approx 0.7 \frac{\lambda}{\sin\phi} \tag{3.4}$$

where λ is the acoustic wavelength and ϕ is the half-angle subtended to the lens aperture (ϕ = 33° for the type I lens). For D = 75 μm measured in the experiment, we have λ = 58.4 μm which corresponds to the acoustic frequency f = 25.7 MHz. Therefore, we estimate that the focused ultrasound has the high-frequency center around 25.7 MHz. But this value was shown as down-shifted to 15~17 MHz range in Fig. 3.4(b), due to the detector bandwidth effect.

We also characterized the focal widths of the type II lens with 2-fold longer focal length but the similar *f*-number. Its lateral and axial FWHMs were broadened to 100 μm and 650 μm. This lateral focal width gives f = 20.1 MHz according to eq. (3.4) which is lower than that of the type I lens. This is due to the acoustic attenuation in the high-frequency components over the long propagation distance. Using the fiber hydrophone, we obtained similar frequency spectra for the type II lens (not shown here) which have

center frequencies around 14~15 MHz. Again, this means that the frequency peaks around the 15 MHz are due to the fiber hydrophone, rather than the focused ultrasound. From the focal spot characterization, we could confirm that both the type I and II lenses exhibit tight focal spots which are an order of magnitude smaller than those of the common HIFU transducers.

3.4 Acoustic Cavitation and Shock Waves Induced by Optoacoustic Focusing

3.4.1 Acoustic Cavitation

The strong negative pressure has an especial importance because the acoustic cavitation can be induced. The collapse of bubbles gives mechanical and thermal impacts to adjacent structures over localized focal volumes. It is valuable to characterize the LGFU-induced cavitation bubbles because our approach provides a novel environment for the acoustic cavitation in terms of a tightly focused high-frequency regime and a single pulse-induced cavitation. In our measurement, we could obtain the acoustic cavitation with heterogeneous boundaries. As the fiber hydrophone provides a solid boundary, the signature of acoustic cavitation appears as the distortion of signal waveforms in the negative pressure phase. Typically, the cavitation-induced distortion immediately follows the negative peak because the pressure goes beyond the cavitation threshold. However, this does not provide sufficient information to analyze the cavitation

behavior. Therefore, we verified the existence of the cavitation bubbles by using the high-speed camera together with the fiber-optic hydrophone.

In order to observe the fast transient cavitation on the fiber surface, we used a high-speed camera (V210, Vision Research, Wayne, NJ, USA) which was integrated into an inverted optical microscope (Fig. 3.8). Instead of the large glass water tank, a 6-inch plastic petri-dish was used as a water chamber to make the setup on the microscope

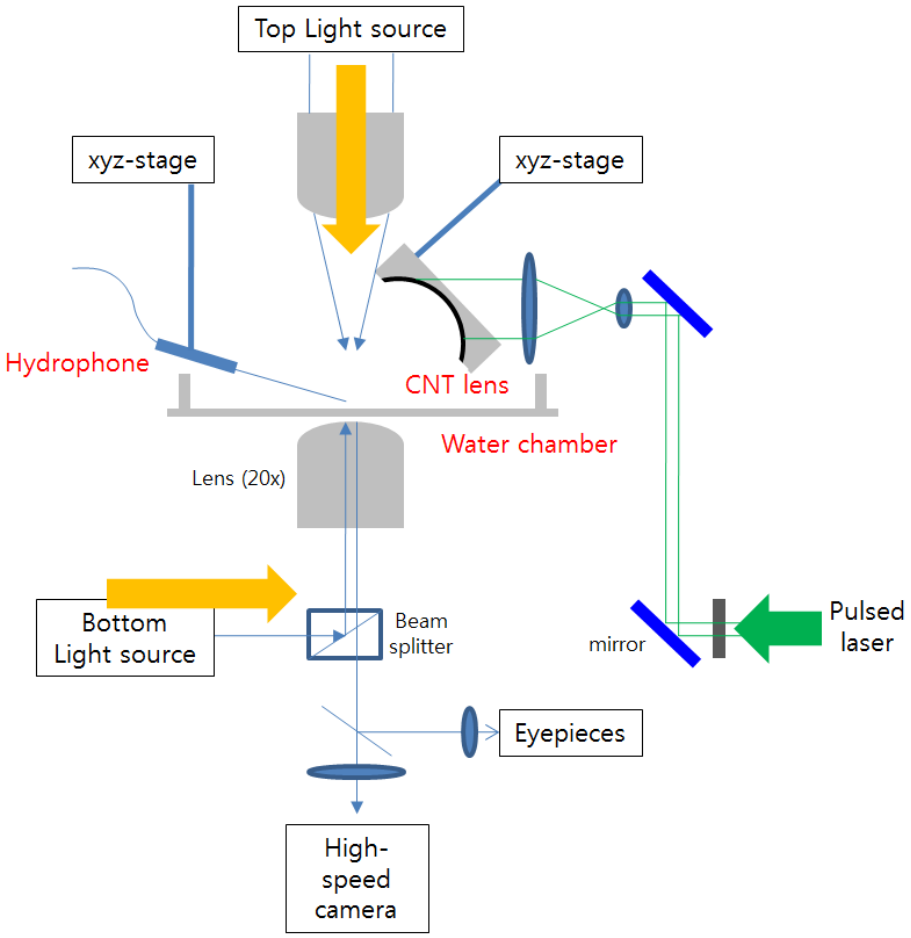

Fig. 3.8 Experimental schematic for simultaneous monitoring of acoustic cavitation by using high-speed camera and fiber-optic hydrophone. The whole optoacoustic setup was built on the stage of optical microscope.

stage. From the top-side of the microscope, a halogen light source was illuminated to the sample stage. Within the water chamber, the fiber hydrophone was positioned near the bottom surface. The focused ultrasound was incident with an angle of ~45° onto the fiber surface. This is due to space limitation associated with the fiber positioning and a short focal distance of an optical lens (×20) located below the water chamber. The type II lens was used for convenience in the arrangement. Using the eyepieces, we first found the optical focus on the sample stage which includes the ultrasonic focus and the hydrophone. As we monitor the short transient bubbles, short exposure time was required in the high-speed camera. Such short exposure time and the microscopic view in the optical microscope needed bright illumination sources. For this purpose, we provided two light sources: one from the top and the other from the bottom. The high-speed camera was connected to the computer. Simultaneously, the output of the fiber-optic hydrophone was sent the same computer through the digital oscilloscope.

The simultaneous monitoring provides clear evidence of the acoustic cavitation and its correlation with the measured waveforms. In Fig. 3.9, the high-speed captured images are shown in the monitor screen located in the left side of each figure. The acoustic waveform, measured at the same time, appears on the digital oscilloscope located in the right. In the oscilloscope screen, the waveform shown at the center is the ac signal while the dc is also shown in the slightly upward location as a straight line. The camera exposure time was 20 μs. Note that the fiber has 125 μm in diameter. In Fig. 3.9(a), as we positioned the fiber out of the focal zone, the acoustic cavitation was not observed. The corresponding pressure amplitude was small in this case. The cavitation bubbles appeared as we moved the fiber around the focal zone in Fig. 3.9(b) ~ (f) (each

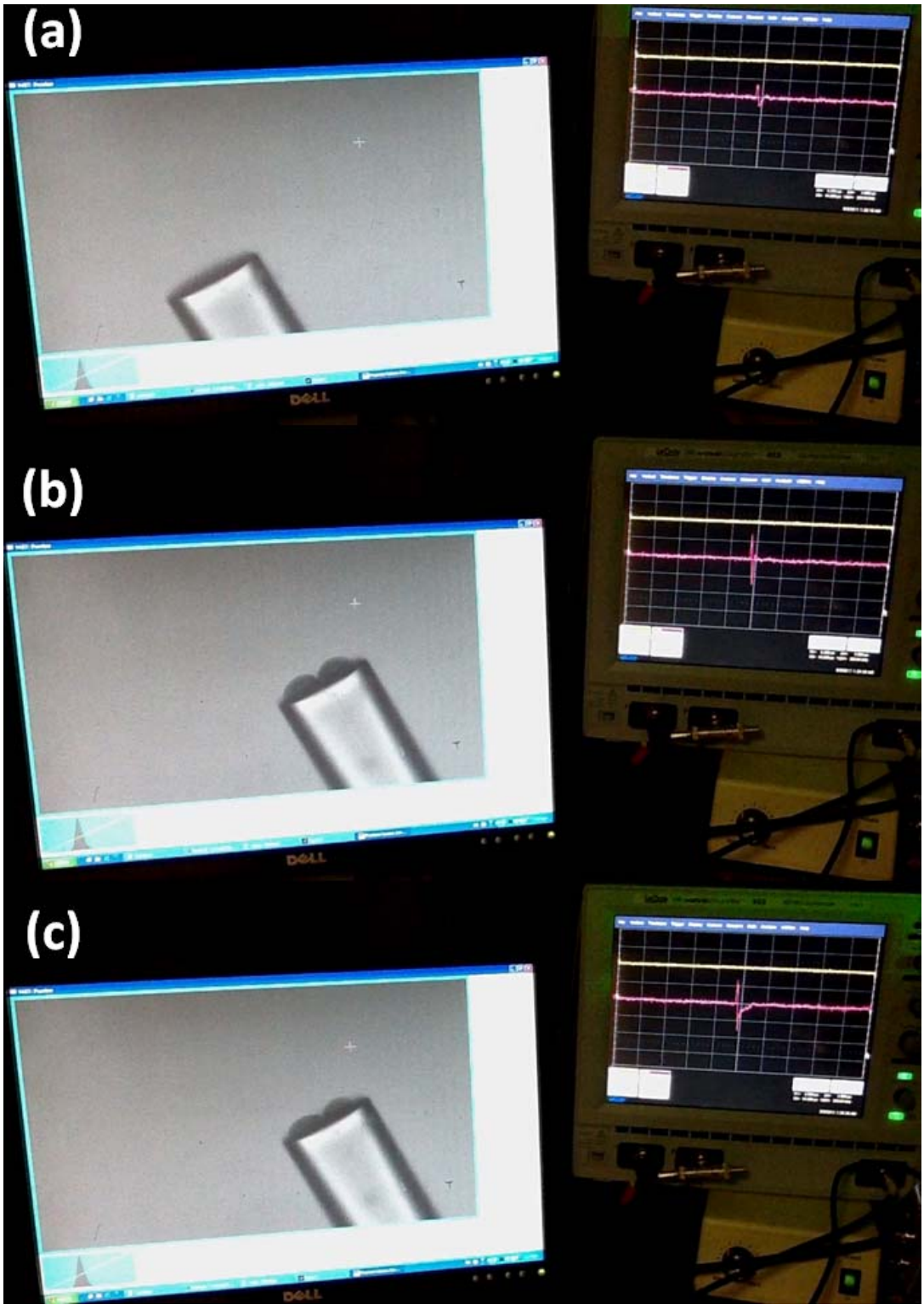

Fig. 3.9 Simultaneous monitoring of acoustic cavitation by using high-speed camera (left on screen) and fiber-optic hydrophone (right on oscilloscope). The results are shown for various positions of the fiber from (a) to (f).

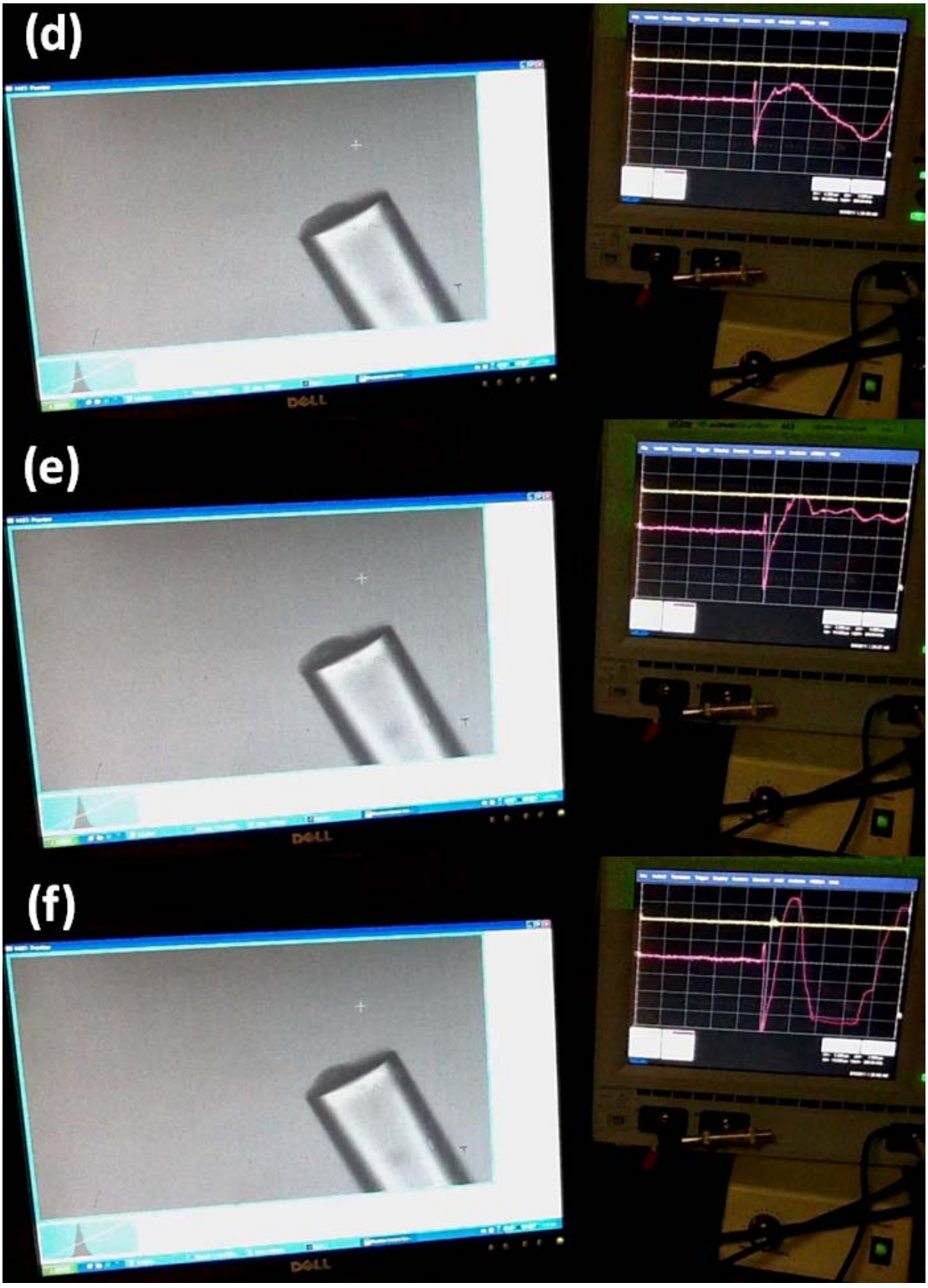

(Fig. 3.9 *continued*)

fiber position is slightly different). All of the bubbles have micro-scale dimensions smaller than the fiber diameter. We could confirm that the fiber boundary is required to induce the bubbles. Moreover, as they are adhered on the surface, we could observe the signal distortion right after the negative phase of the original waveform. Interestingly, the fiber hydrophone output in the oscilloscope has no signature of the acoustic cavitation in the case of Fig. 3.9(b), although we can clearly see the bubbles on the fiber surface. This is because the substantial sensor area is determined by the core (6-μm diameter) which is located at the center of the fiber surface. The micro-bubbles should sweep over the core area to be detected as the fiber-optic response. We believe that the bubbles shown in Fig. 3.9(b) do not have direct overlap with the core area. This is compared with Fig. 3.9(d), (e), and (f), all of which have violent oscillatory phases due to the acoustic cavitation. Fig. 3.9(c) corresponds to the moment that the cavitation bubbles begin to sweep. The slight distortion follows the negative phase of the waveform. Such distortion became more pronounced as we moved the fiber to the exact focal point (from (d) to (f)).

3.4.2 Collapse Time of Transient Micro-Bubbles

From the previous experiment of simultaneous monitoring, we could confirm that multiple bubbles with different sizes are formed on the fiber surface, usually smaller than the fiber diameter. However, we could not distinguish such multiple bubbles, just from the fiber output shown in the oscilloscope. We further characterized the multiple bubbles in terms of their collapse time (or lifetime). Using the setup shown in Fig. 3.3(b), we introduced the separate transducer to have the same focus with the optoacoustic

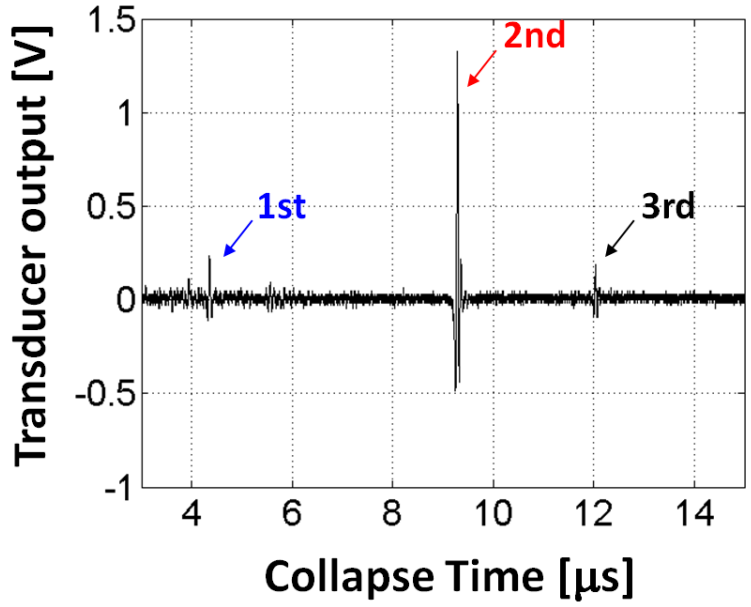

(a)

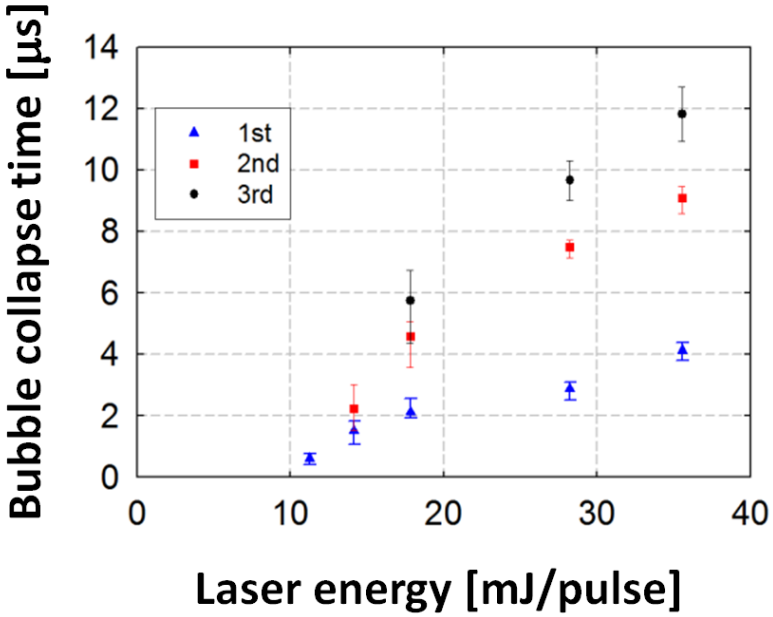

(b)

Fig. 3.10 Measurement of the acoustic cavitation induced by the LGFU. (a) Bubble collapse events are shown in the time-domain. Three arrows indicate the pressure signal radiated from the bubble collapse. (b) The bubble collapse times are plotted as a function of the laser energy. The bubble collapse events were categorized as three types according to their evolution trend. No cavitation signal was monitored under ~10 mJ/pulse.

focusing lens. Fig. 3.10(a) shows a time-domain signal trace obtained by the additional detector. We define the collapse time as the relative time difference between the reference (*i.e.* 33 μs) and the actual collapse moment. At the temporal reference of the transducer at 33 μs, the large signal peak is shown due to acoustic reflection of the LGFU from the fiber hydrophone. Under a single LGFU pulse, we could observe 1~3 cavitation bubbles with different collapse times. The number of bubbles depended on the laser energy and the focused pressure. Fig. 3.10(b) shows that the bubble collapse time increases with the laser energy. For the laser energy of <40 mJ/pulse, the collapse time was usually shorter than 15 μs.

3.4.3 Solid Material Fragmentation

Shock-wave lithotripsy has been used as an effective approach for fragmentation of kidney stones [19] and disruption of blood clots in vessels [20]. As the LGFU can induce the strong shock waves and the acoustic cavitation at the tight focal spots, we performed fragmentation experiments using an artificial kidney-stone [32] and a polymer film (PMMA) coated on a glass substrate. Fig. 3.11 shows the treatment result on the artificial stone. A single pulse of LGFU created a treatment dimension of 300~500 μm. The line patterns were generated by rapidly moving the LGFU spot which delivers just a few pulses in each position. The dot patterns were generated over an exposure time of 1~2 minutes without moving the LGFU spot. The spatial scale could be controlled by changing the pressure amplitudes and the exposure time. This is because the region of strong shock and acoustic cavitation can be increased (or decreased) by the pressure

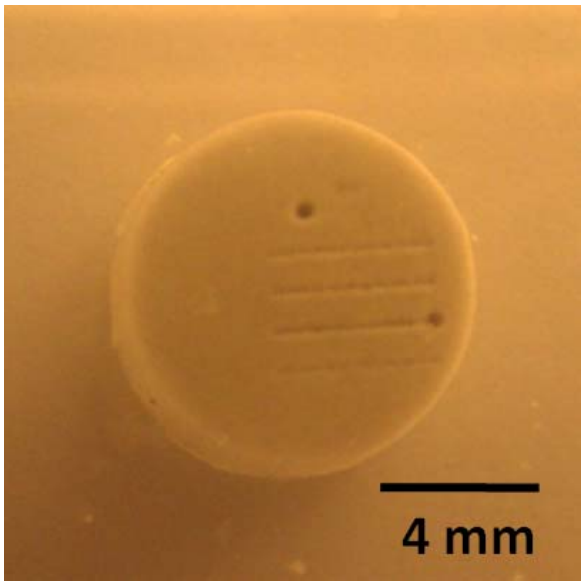

Fig. 3.11 LGFU treatment on the artificial stone. The dots and the lines on the sub-millimeter scale were created by the shock waves and the acoustic cavitation.

amplitudes on the focal plane, and the exposure time is associated with the accumulated energy. Here, we used the model stone for demonstration of the LGFU-induced impact, but this elaborate control in the fragmentation would be more suitable for high-accuracy applications such as blood vessels and tissue layers.

The acoustic cavitation can contribute to the fragmentation process by a variety of mechanisms such as erosion, spallation, shear, and dynamic fatigue [33]. But these mechanical and thermal impacts from the LGFU-induced bubbles are not clear because they are characteristically distinguished from the low-frequency HIFU bubbles in radius and lifetime. We confirmed how the LGFU-induced cavitation can enhance the fragmentation by microscopic monitoring. The LGFU setup was prepared on a stage of an optical microscope with the high-speed camera. As a treatment sample, the polymer film was used for convenience in the arrangement. The cavitation bubbles were generated

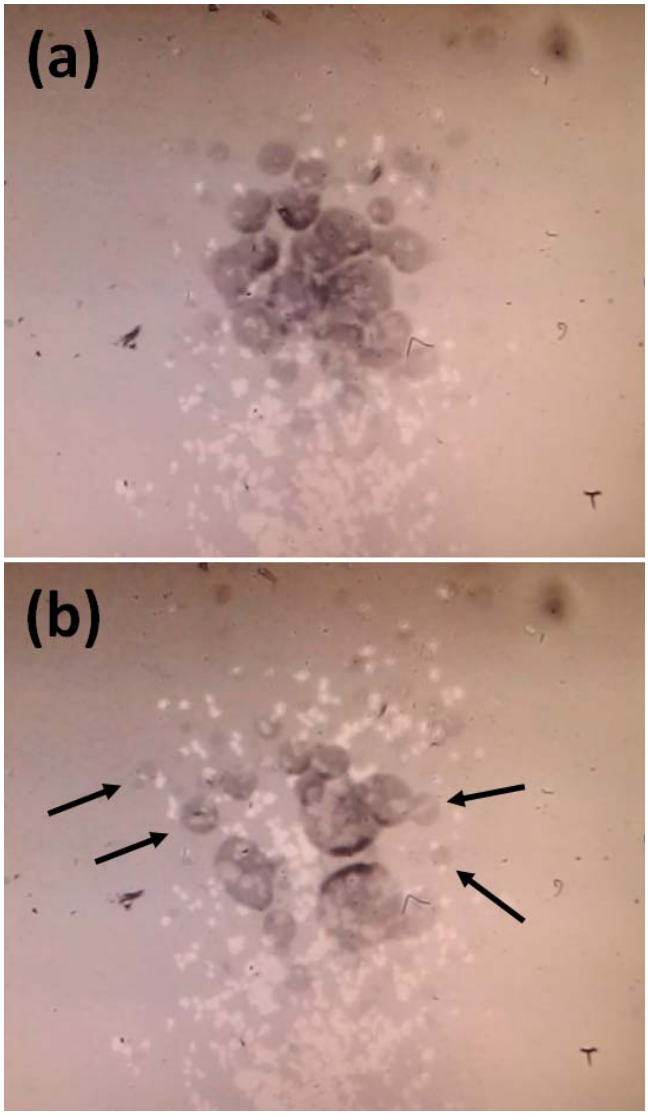

Fig. 3.12 Cavitation-enhanced fragmentation during LGFU treatment on the polymer film (the polymer detached region is shown brightly). Formation of cavitation bubbles are shown at the center which corresponds to the LGFU spot. The high-speed captured image shown in (a) was taken by ~1.5 second earlier than in (b). It is shown in (b) that the bubbles are preferentially generated on the micro-scale holes and cracks (indicated by the arrows).

as soon as the polymer was exposed under the LGFU (Fig. 3.12). The polymer film was fragmented into micro-particles by the shock waves and the acoustic cavitation. The

polymer-fragmented regions are seen as the bright spots. The image of Fig. 3.12(a) was taken by ~1.5 second earlier than that of Fig. 3.12(b). The acoustic cavitation was expedited by cracks and holes (indicated by the arrows) created by the dynamic fatigue during the compressive and tensile cycles of the LGFU. Consequently, the film was further eroded by the collapse of the collateral micro-bubbles in contact with the polymer. The micro-scale fragmentation process would be useful for applications which require delicate control over highly localized volumes.

3.4.4 Observation of Long-Lived Micro-Bubbles under Higher Negative Pressure Regime

The pressure amplitudes of the LGFU are not limited by the current lens design and the excitation laser used in this work. As the nonlinear induced behaviors are of particular interests, it is significant to explore such effects under higher negative pressure that can be reached by modified LGFU systems. In an effort to increase the negative amplitudes, we prepared a reflection-mode focusing configuration [34]. The experimental setup is shown in Fig. 3.13(a). The fiber hydrophone was located below the water surface at the reflected focus of the LGFU. As we use an air/water interface as a reflector with a reflection coefficient near −1 due to acoustic impedance mismatch ($Z_{water} \approx 3700 Z_{air}$), strong positive amplitudes of the incident shock waves can be totally reflected and inverted into negative ones. Slightly below the air/water boundary, the reflected negative amplitudes can be further enhanced by superposition with the successive negative phase of the incoming waveform. For our LGFU pulse, a maximum reflected focus was located

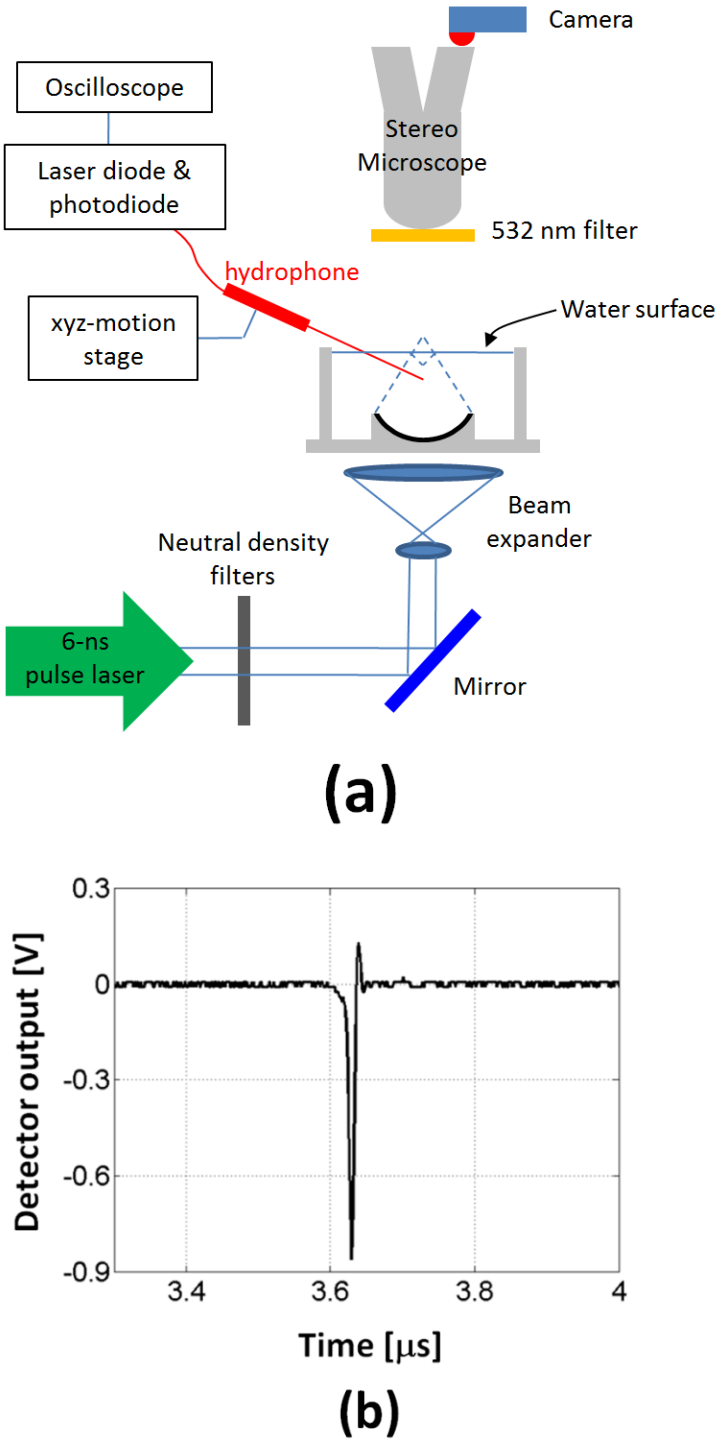

Fig. 3.13 (a) Experimental schematic for the LGFU in the reflection-mode. The maximum amplitude in the negative peak is measured at the reflected focal point (*i.e.* slightly upward from the hydrophone position shown in the figure). (b) Typical waveform of the reflected LGFU measured by the fiber-optic hydrophone. Note that the acoustic cavitation effect is probably mixed in the negative amplitude.

at 15~25 μm below the surface. In this way, we could generate several fold higher negative amplitudes. Fig. 3.13(b) shows the typical waveform at the reflected focal spot, obtained at the laser energy of >50 mJ/pulse. According to the sensitivity of the fiber hydrophone, this unusual negative peak corresponds to -145 MPa (-850 mV at the detector output). The peak amplitude was fluctuated within 20~30% range in the fixed time frame, rather than staying at a constant value. The amplitude fluctuation means that -145 MPa is not purely from the focused ultrasound as the negative phase already involves the acoustic cavitation and then causes the signal distortion dynamically.

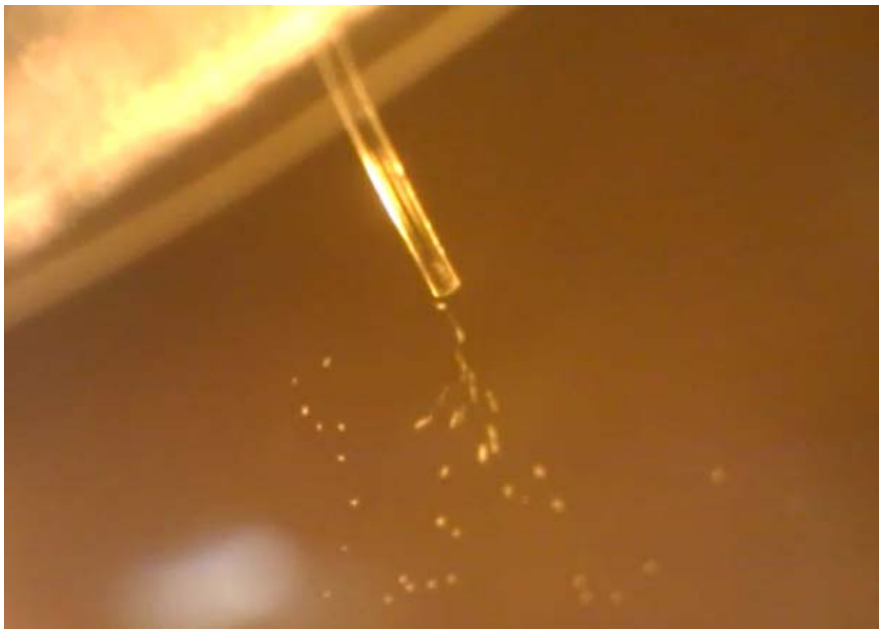

Fig. 3.14 Long-lived micro-bubble generation in the reflected focusing configuration. The fiber hydrophone (125 μm in diameter) was positioned slightly below the water surface which is the reflected focal spot of the LGFU. As soon as the micro-bubbles were generated, they left out of the focal zone.

Fig. 3.14 shows the photograph at the focal spot observed under an optical stereo microscope. Interestingly, we could observe the micro-bubbles even under naked eyes, indicating that they are stable and long-lived in time. The lifetime was unusually long, two orders of magnitude longer than those from the preceding setup. We also observed that the bubbles come out of the fiber surface as soon as generated, instead of being adhered on the fiber. These mean that the bubbles are generated in a secondary regime obtained under very high negative pressure. However, they still required the fiber hydrophone as a boundary for cavitation inception. For the free-boundary cavitation, we believe that simple increase of the lens area and the pressure amplitude is not a proper solution. We need to change the characteristics of excitation laser (*e.g.* increase in the pulse repetition rate) as the cavitation threshold is also a function of pulse repetition rate, temporal width, acoustic frequency, temperature, and so on [3,35].

3.5 Superposition of Focused Ultrasonic Waves for Enhanced Negative Pressure and Free-Boundary Cavitation

3.5.1 Pressure Enhancement by Superposition of Focused Ultrasound

Pulsed cavitational ultrasound therapy (PCUT) in low frequency has shown promising results which are useful for clinical applications [36]. In the typical HIFU, heat accumulation and thermal ablation is the primary mechanism for therapeutic effects, but the PCUT mainly depends on mechanical impacts from bubble collapse which leads to

local fractionation of tissues. The current LGFU is in line with the pulsed HIFU because of low repetition rate of the laser pulses (20 Hz).

In order to utilize the LGFU as the PCUT purpose, the focused ultrasound should be able to generate the cavitation bubbles on soft tissue boundaries or in a free-boundary condition. While the LGFU delivers strong peak pressure over the short pulse duration of ~10 ns, its intensity is fairly low due to the low repetition rate. Additional focused transmitters (*e.g.* low frequency) can be arranged to have the same focus with that of the LGFU and to boost the pressure and the intensity. We can use a low-frequency focused

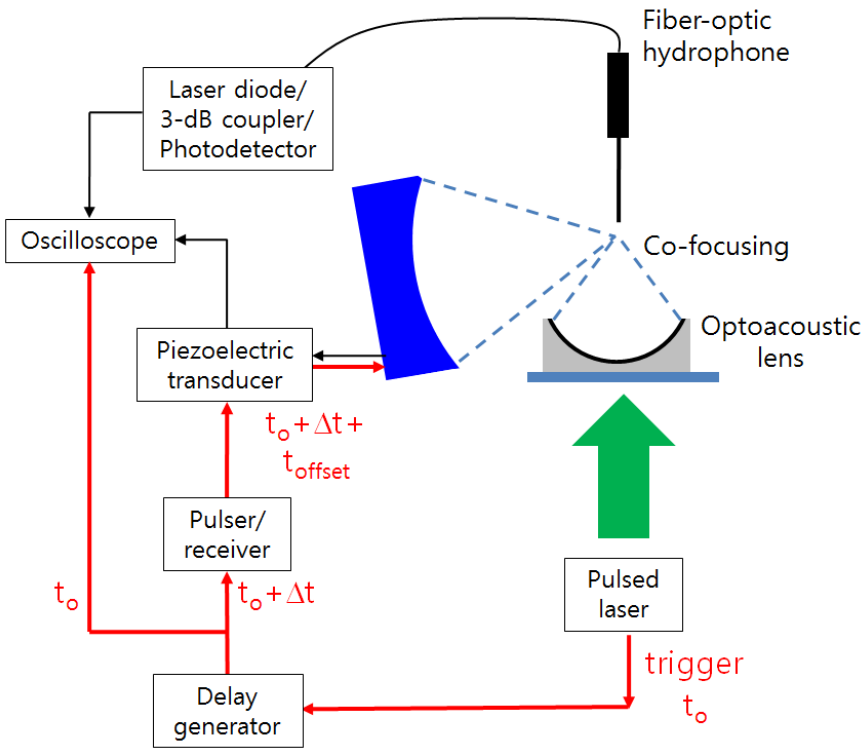

Fig. 3.15 Delay application scheme to superpose two focused ultrasonic waves which are generated from different focal lengths: 5.5 mm in the optoacoustic lens and 38.1 mm in the piezoelectric transducer. The internal trigger of the pulsed laser is used as a timing reference.

transducer as the additive one, but operate it below the cavitation threshold. Being superposed with the optoacoustic pulse, the focused ultrasound can induce the acoustic cavitation in tightly localized volumes, which is one of the main advantages of the LGFU. This would cause the overall focused pressure profiles to broaden, but they are in the sub-threshold regime.

We superposed two focused ultrasonic waves which were generated from the optoacoustic lens (type I) and a piezoelectric transducer which has a center frequency of 3.5 MHz and a focal distance of 38.1 mm. The experimental setup is shown in Fig. 3.15. As the focal lengths of optoacoustic lens (~5.5 mm) and the piezoelectric transducer (38.1 mm) are different, we need to apply a time delay between these two sources. In the delay application, we have one restriction that our pulsed laser does not receive an external trigger as its input. Therefore, we used a trigger timing of the pulsed laser (t_0) as an input reference to the delay generator shown in Fig. 3.15. The time delay Δt was applied to the pulser/receiver module which has its own timing (t_{offset}) to generate electrical pulses. Finally, the piezoelectric transducer could deliver the acoustic pulses at $t_0 + \Delta t + t_{offset}$. As we should give a delay into the piezoelectric transducer which has the initially longer focal distance, approximately one repetition interval of the pulse laser (50 ms) was applied to Δt. The ultrasonic focus was aligned by using the fiber-optic hydrophone. Then, we could simultaneous monitor both signals from the optoacoustic lens and the piezoelectric transducer through the fiber hydrophone in the oscilloscope.

Fig. 3.16 shows the signal waveforms before and after superposition. Before the superposition, the focused ultrasound from the piezoelectric transducer is shown in Fig.

3.16(a). Three oscillatory cycles were generated under a single voltage pulse. Around the center of the waveform (~28.4 μs), we have the maximum amplitude in its negative phase. Note that the electronic time-delay was applied from the pulser/receiver module due to its internal time lag. Therefore, the time values in Fig. 3.16 do not reflect the propagation

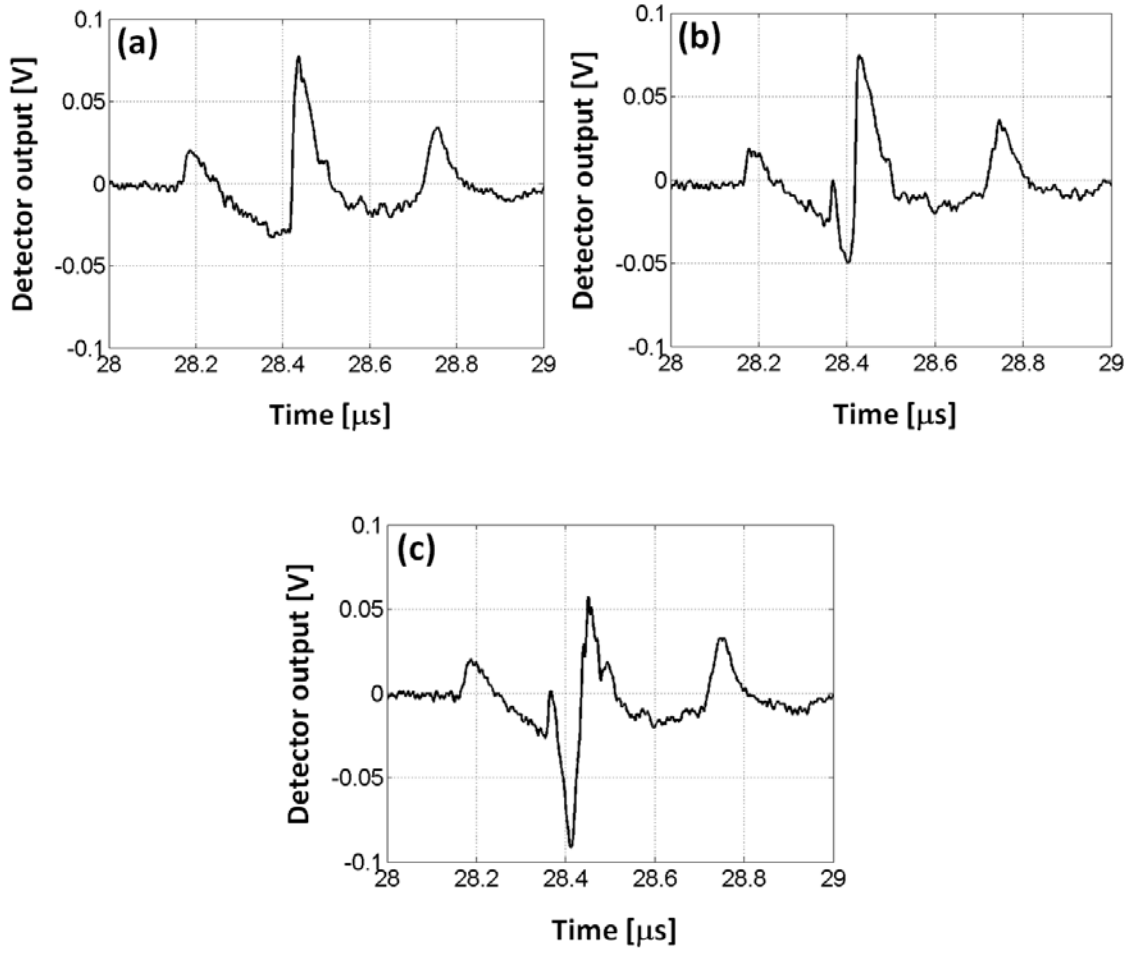

Fig. 3.16 Superposition of two focused ultrasonic waveforms generated from the optoacoustic lens and the piezoelectric transducer. The waveform of the piezoelectric transducer is shown in (a) (before superposition). Superposed waveforms are shown where the negative peak is ~60% of the cavitation threshold pressure in (b) and around the cavitation threshold. The time values do not correspond to the propagation distances due to the application of electronic time-delays (they are just relative).

distance. The negative peak pressure at the center was around -5 MPa. This is not sufficient to induce the cavitation. In Fig. 3.16(b), the waveform was superposed with the optoacoustic pulse which has the short temporal width. We adjusted the time delay to have the superposition at 28.4 μs which makes enhancement in the negative amplitude. The enhanced negative pressure is ~60% of the cavitation threshold. The further enhancement is shown in Fig. 16(c), which corresponds to the negative pressure slightly below the cavitation threshold. For higher laser energy, we could observe the waveform distortion which means the involvement of acoustic cavitation.

3.5.2 Observation of Free-Boundary Cavitation

We demonstrated the free-boundary cavitation under the superposition of two focused ultrasonic waves. We first made the superposition alignment by using both transmitters and then completely removed the fiber-optic hydrophone from the focal zone. The collapse signal was detected by the same piezoelectric transducer as shown in Fig. 3.17. The time-domain signal traces are compared without the bubble collapse moment in Fig. 3.17(a) and with the collapse in Fig. 3.17(b). The artifact is due to acoustic reflection from the edge of the optoacoustic lens. A few bubble collapse moments were randomly observed for 30-second monitoring time (the oscilloscope images are directly shown due to difficulty in catching the digitized signal waveforms which exactly include the collapse moments). The bubble collapse was observed only when both transmitters were superposed. In case of removing either optoacoustic or piezoelectric transmitters, we could not monitor the collapse event. For the given pulse repetition rate of 20 Hz, the

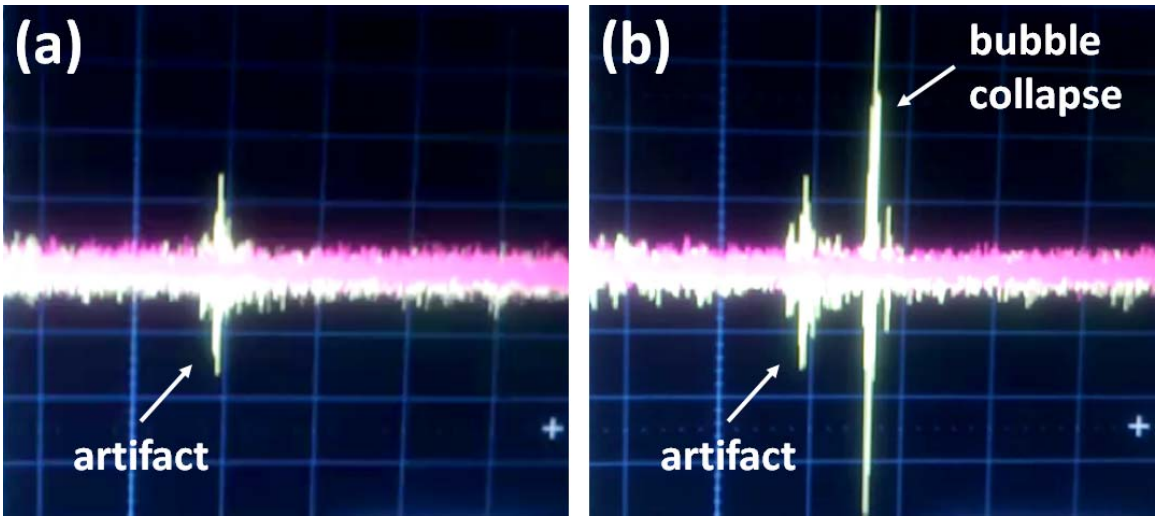

Fig. 3.17 Detection of free-boundary cavitation (captured images from video-recording of the oscilloscope screen). The time-domain signal traces are captured directly from the oscilloscope: without the bubble collapse moment in (a) and with the collapse in (b).

probability of bubble generation (number of bubbles per number of laser pulses) was lower than 0.5%. In the previous heterogeneous cavitation where the fiber surface was used as the promotion boundary, we could observe the cavitation signal for each laser pulse. Although we obtained the cavitation bubbles in the low rate, this opens the possibility of using the free-boundary bubbles for the pulsed HIFU therapy. We also note that the superposed piezoelectric transducer here generates relatively low pressure amplitudes (-5 MPa). The superposed configuration can be promisingly improved in many ways by varying the control parameters of both transmitters such as the negative pressure amplitude, the operation frequency, and the pulse repetition rate.

3.6 Additional Features and Advantages of LGFU Approach

The LGFU has been introduced to generate strong and high frequency pressure which is sufficient to involve the shock waves and the acoustic cavitation in high resolutions. However, the potential of the LGFU is not limited by the scope of the current work. We emphasize that the LGFU characteristics rely on the excitation lasers as well as the optoacoustic sources. Pulsed-laser technologies give the LGFU great flexibility in determining specific frequency ranges and pressure amplitudes. While we used 6-ns in the pulse width, 20 Hz in the repetition rate, and tens of mJ in the laser energy, numerous pulsed lasers are commercially available with different conditions. Therefore, we can further improve the pressure amplitudes by using narrower laser pulses in time because the far-field optoacoustic pressure is proportional to the time-derivative of the original laser pulse. By using 1-ns laser pulses, we expect to reduce the cavitation threshold of laser energy by a factor of 1/6.

The pulse repetition is proportional to the intensity. The pulse repetition of higher than kHz is possible in the similar pulse energy and width, and it can be increased up to GHz with reduced laser energy. However, the choice of repetition rate relies on applications as the high intensity accumulates heat at focal volumes. The heating is an essential mechanism for cancer therapy through hyperthermia, but this should be excluded in drug delivery and thrombolysis because of irreversible thermal effects [37,38].

Moreover, our optoacoustic focusing approach has further advantages in operation and structure. In the operation, focal diameters and depths can be controlled in

a single optoacoustic lens by replacing the excitation lasers. In the traditional transducers, the operation frequency is initially fixed by the transducer thickness. However, the optoacoustic operation frequency is primarily determined by the excitation lasers, not by the optoacoustic source material. Various laser beams with different temporal profiles can be irradiated on a single CNT-polymer film. Then, we can obtain the focused ultrasound with the specific frequency characteristics of the excitation laser which determine the focal diameters and depths. In terms of device structure, the optoacoustic focusing lens simply consists of the concave substrate and the light-absorbing film. The lens can be scaled up to those of typical HIFU transducers and easily work with enlarged laser beams. Also, there are no complex issues for electrical impedance matching and high driving voltages.

3.7 Conclusion

We presented a new approach to optoacoustically deliver high-amplitude and high-frequency focused ultrasound in a non-invasive and non-ionized way. We suggested the major features of the optoacoustic focusing lenses which are high focal gains and short distances for shock formation. These are primarily due to the low *f*-number geometries, high-frequency natures of the optoacoustic generation. Even more on these unique focusing designs, we utilized the high-efficiency source materials which are the gold-coated CNT-PDMS composite films capable of converting the optical energy to the acoustic output. At the lens focus, we obtained the unprecedented optoacoustic pressure

amplitudes due to such characteristics of the optoacoustic focusing approaches. Furthermore, the high damage threshold in the CNT-polymer composites allowed the available laser energy and the maximum achievable pressure. From the small dimension lens of the type I (6 mm in diameter and 0.92 in *f*-number), we could generate the strong positive peak of 58 MPa at the tight focal spot of 75 μm in lateral and 400 μm in axial directions. The pronounced shock waves were formed at the short focal distance of ~5.5 mm. In the negative pressure, the measurable peak amplitudes were limited to ~13.7 MPa for the laser energy of 14 mJ/pulse (type I lens) and 10 mJ/pulse (type II lens). This is due to the measurement limitation because the acoustic cavitation is involved at these pressure levels on the fiber surface and then distorts the waveforms in the negative phase. Probably, higher than 25 MPa in the negative peak will be reached if the pressure amplitude is extrapolated over the high laser energy (the maximum available laser energy is ~6-fold higher than the threshold values). The temporal and the spatial profiles were experimentally characterized. The cavitation bubbles were characterized in terms of size and lifetime. The collapse time of micro-bubbles was typically <15 μs for the low laser energy range of <40 mJ/pulse. The LGFU-induced shock waves and acoustic cavitation were used for micro-scale fragmentation of the artificial stone and the polymer film. The cavitation-induced enhancement was confirmed in the fragmentation process of the polymer film. The cavitation behavior was further investigated under the condition of much higher negative pressure. We could observe the micro-bubbles which have the long lifetime of several seconds. These are distinguished from the previous cases obtained under the low laser energy. However, despite such highly negative amplitudes, the acoustic cavitation still needed the solid boundaries. The free-boundary cavitation was

achieved by using the superposition of two focused ultrasonic waves from the optoacoustic and the piezoelectric transmitters. The cavitation probability was lower than 0.5 %, but this can be further improved in many ways by varying the control parameters of both transmitters. The LGFU has great flexibility in terms of transmitter designs and excitation laser choices to control ultrasonic frequencies, amplitudes, and intensities. We expect that the LGFU becomes a versatile modality over a broad range of applications, especially as a high-accuracy treatment tool for cells, blood vessels, and tissue layers.

References

[1] M. F. Hamilton and D. T. Blackstock, *Nonlinear Acoustics*, Acoustical Society of America, Melville (2008).

[2] C. C. Coussios and R. A. Roy, Annu. Rev. Fluid Mech. 40, 395 (2008).

[3] E. Herbert, S. Balibar, and F. Caupin, Phys. Rev. E 74, 041603 (2006).

[4] E. A. Filonenko and V. A. Khokhlova, Acoust. Phys. 47, 468 (2001).

[5] M. R. Bailey, V. A. Khoklova, O. A. Sapozhnikov, S. G. Kargl, and L. A. Crum, Acoust. Phys. 49, 369 (2003).

[6] D. Dalecki, E. L. Carstensen, K. J. Parker, and D. R. Bacon, J. Acoust. Soc. Am. 89, 2435 (1991).

[7] M. S. Canney, M. R. Bailey, L. A. Crum, V. A. Khokhlova, and O. A. Sapozhnikov, J. Acoust. Soc. Am. 124, 2406 (2008).

[8] M. A. Averkiou and M. F. Hamilton, J. Acoust. Soc. Am. 102, 2539 (1997).

[9] J. E. Kennedy, Nat. Rev. Cancer 5, 321 (2005).

[10] Y.-F. Zhou, World J. Clin. Oncol. 2, 8 (2011).

[11] T. J. Dubinsky, C. Cuevas, M. K. Dighe, O. Kolokythas, J. H. Hwang, Am. J. Roentgenol. 190, 191 (2008).

[12] S. Mitragotri, Nat. Rev. Drug Discov. 4, 255 (2005).

[13] J. J. Choi, K. Selert, Z. Gao, G. Samiotaki, B. Baseri, and E. E. Konofagou, J.

Cerebral Blood Flow Metabol. 31, 725 (2011).

[14] B. Krasovitskia, V. Frenkelb, S. Shohama, and E. Kimmela, Proc. Natl Acad. Sci. USA 108, 3258 (2011).

[15] S. Song, Z. Shen, L. Chen, A. A. Brayman, and C. H. Miao, Gene Ther. 18, 1006 (2011).

[16] Y. Tufail, A. Yoshihiro, S. Pati, M. M. Li, and W. J. Tyler, Nat. Protocols 6, 1453 (2011).

[17] S.-S. Yoo, A. Bystritsky, J.-H. Lee, Y. Zhang, K. Fischer, B.-K. Min, N. J. McDannold, A. Pascual-Leone, and F. A. Jolesz, Neuroimage 56, 1267 (2011).

[18] J. E. Lingeman, J. A. McAteer, E. Gnessin, and A. P. Eva, Nat. Rev. Urology 6, 660 (2009).

[19] J. J. Rassweiler, T. Knoll, K.-U. Köhrmann, J. A. McAteer, J. E. Lingeman, R. O. Cleveland, M. R. Bailey, C. Chaussy, Eur. Urol. 59, 784 (2011).

[20] C. Goldenstedt, A. Birer, D. Cathignol, and C. Lafon, Ultrasound Med. Biol. 35, 985 (2009).

[21] V. E. Gusev and A. A. Karabutov, *Laser Optoacoustics*, American Institute of Physics, New York (1993).

[22] R. J. von Gutfeld and H. F. Budd, Appl. Phys. Lett. 34, 617 (1979).

[23] T. W. Murray, S. Krishnaswamy, and J. D. Achenbach, Appl. Phys. Lett. 74, 3561 (1999).

[24] T. Buma, M. Spisar, and M. O'Donnell, Appl. Phys. Lett. 79, 548 (2001).

[25] Y. Hou, J. S. Kim, S. Ashkenazi, M. O'Donnell, and L. J. Guo, Appl. Phys. Lett. 89, 093901 (2006).

[26] H. W. Baac, J. G. Ok, H. J. Park, T. Ling, S.-L. Chen, A. J. Hart, and L. J. Guo, Appl. Phys. Lett. 97, 234104 (2010).

[27] R. S. C. Cobbold, *Foundations of Biomedical Ultrasound*, Oxford University Press, New York (2007).

[28] M. D. Volder, S. H. Tawfick, S. J. Park, D. Copic, Z. Zhao, Wei Lu, and A. John Hart, Adv. Mater. 22, 4384 (2010).

[29] J. E. Parsons, C. A. Cain, J. B. Fowlkes, J. Acoust. Soc. Am. 119, 1432 (2006).

[30] G. J. Diebold, *Photoacoustic Imaging and Spectroscopy*, Chap. 1, edited by Lihong V. Wang, CRC Press, Boca Raton (2009).

[31] J. F. Krücker, A. Eisenberg, M. Krix, R. Lötsch, M. Pessel, and H.-G. Trier, J. Acoust. Soc. Am. 107, 1994 (2000).

[32] Y.A. Pishchalnikov, O.A. Sapozhnikov, M. R. Bailey, J. C. Williams, R. O. Cleveland, T. Colonius, L. A. Crum, A. P. Evan, and J. A. McAteer, J. Endourol. 17, 435 (2003).

[33] M. R. Bailey, L. A. Crum, A. P. Evan, J. A. McAteer, J. C. Williams, O. A. Sapozhnikov, R. O. Cleveland, and T. Colonius, Fifth International Symposium on Cavitation, Cav03-OS-2–1–006, Osaka, Japan (2003).

[34] A. D. Maxwell, C. A. Cain, J. B. Fowlkes, and Z. Xu, IEEE International Ultrasonics Symposium Proceedings, 108 (2010).

[35] A. A. Atchley, L. A. Frizzell, R. E. Apfel, C. K. Holland, S. Madanshetty, and R. A. Roy, Ultrasonics 26, 280-285 (1988).

[36] Z. Xu, M. Raghavan, T. L. Hall, M.-A. Mycek, J. B. Fowlkes, and C. A. Cain, IEEE Trans. Ultrason., Ferroelect., Freq. Contr. 55, 1122 (2008).

[37] V. Frenkel, and K. C. P. Li, Future Oncol. 2, 111 (2006).

[38] D. V. Sakharov, R. T. Hekkenberg, and D. C. Rijken, Thromb. Res. 100, 333 (2000).

Chapter IV

Optical Detection of High-Frequency Focused Ultrasound by using Polymer Microring Sensors

4.1 Introduction

For the optical detection of ultrasound, various configurations have been proposed using optical interferometric mechanisms, such as optical etalons [1,2], microring resonators [3-5], and Mach-Zehnder interferometers [6]. Among these approaches, the microring resonators have exhibited excellent characteristics in terms of frequency response, sensitivity, and spatial dimension.

The optical microring detector has a finite dimension in its diameter and waveguide width. For high frequency ultrasound, the acoustic wavelength can be comparable or even smaller than the microring size. Such a characteristic could be manifested in the microring response. Despite its excellent bandwidth up to high frequency, spatial and temporal responses of the microring in this regime have not been properly characterized so far. Here, we first confirm the microring responses under high frequency focused ultrasound. This is an essential step for later evaluating performances of focused ultrasound transmitters by the microring detectors.

As we need to characterize the microring (2 μm in waveguide width and 100 μm in diameter) in high-spatial resolution, a spatially localized acoustic source should be prepared. For this purpose, we use a metallic thin film to generate and focus high-frequency ultrasound. The laser-generated ultrasound is a proper source to characterize frequency-dependent responses of detector over a wide spectral range because the source materials can also provide similar frequency range. Here, we introduce an optoacoustic concave transmitter capable of sharp focusing. The focusing is achieved with a Cr layer deposited on the concave side of plano-concave glass lens. The transmitter is back-illuminated with ns laser pulses through the planar glass side, which leads to positive focusing of the acoustic waves.

4.2 Experimental configuration

We used the same polymer microring [7] which was introduced in the chapter II. The microring was operated in the same manner here. The optoacoustic concave transmitter was fabricated by depositing a 100 nm thick Cr layer by sputtering over a plano-concave spherical glass (Newport, KPC 043; radius-of-curvature 12.92 mm; diameter 22.86 mm). Sputtering was used to obtain uniform film thickness on the curved substrate. The measurement setup is shown in Fig. 4.1(a). A pulsed laser beam with 532 nm wavelength was used to illuminate the Cr film. A neutral density filter was used to attenuate the laser power. At the position of transmitter, the laser beam is 37 mm in diameter that is 1.5 times larger than the lens diameter, and the laser fluence is lower than

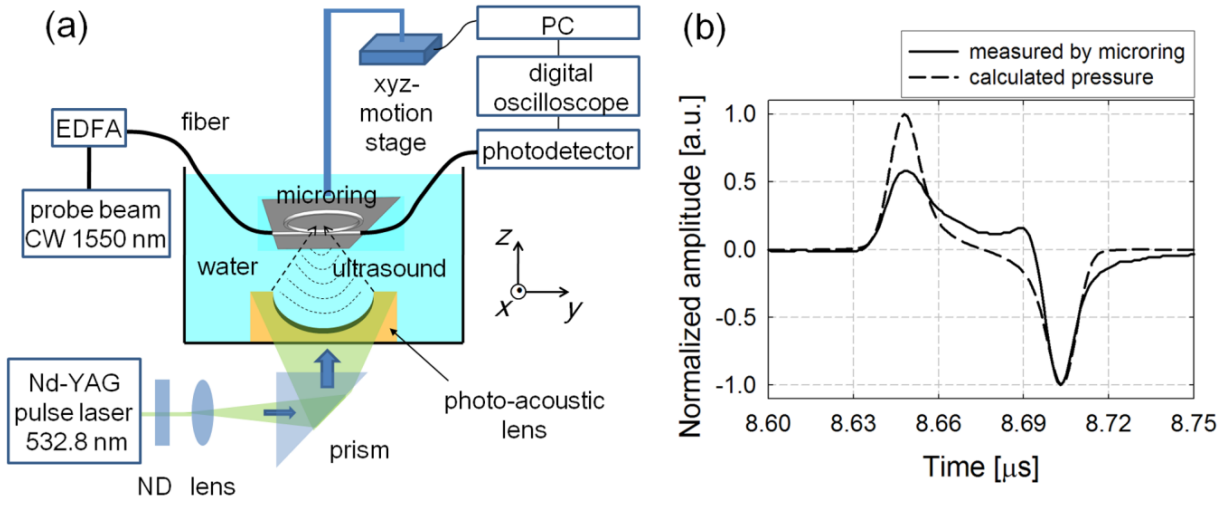

Fig. 4.1 (a) Measurement schematic (ND: neutral density filter; EDFA: erbium-doped fiber amplifier). (b) Temporal waveform measured at the focal spot. The calculated waveform does not include the effect of microring bandwidth.

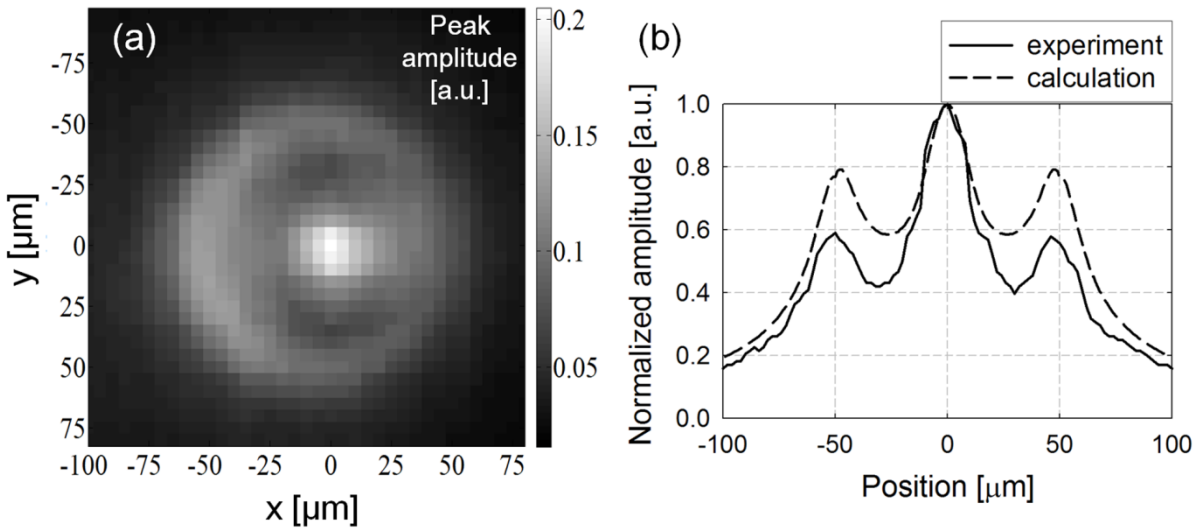

Fig. 4.2 (a) 2-D spatial profile of focused ultrasound measured at the focal plane by the microring detector. (b) 1-D profile measured across the focal spot. The calculated pressure profile in (b) does not include the effect of microring bandwidth.

0.5 mJ/cm^2. A larger beam size is desirable to ensure a sufficiently large effective aperture as well as uniform illumination over the lens surface. The focused ultrasound profile was measured by scanning the microring using motorized motion stages. An ideal frequency spectrum of optoacoustic source can be estimated by taking the Fourier transform of the time-derivative of the 6 ns laser pulse. The spectrum has a center frequency at 67.5MHz and 3-dB roll-off at 35 and 107 MHz.

4.3 Microring Detector Responses for Focused Ultrasound

4.3.1 Spatial Profiles Measured by Optical Microring Detectors

The optoacoustic concave transmitter generates the acoustic waves simultaneously over the concave surface due to rapid thermal expansion of the Cr film by the absorption of pulsed laser energy. The time-domain signal measured at the focal point (*i.e.* the center of the concave surface) should be the coherent summation of the acoustic waves generated from each point on the spherical Cr surface. In Fig. 4.1(b), the temporal profile near the focal point is shown, which is similar to the time derivative of the input laser pulse with the exception of a small kink between the peaks. The peak-to-peak interval was ~54 ns. This interval and the broadening in each polarity agree with that of simulated pressure waveform, not including the effect of microring bandwidth. The calculation was done by integrating the acoustic pressure at focal plane over the ring geometry [8] and taking into consideration the sound attenuation in water. We assume

uniform spatial distribution of optical beam on the Cr film in calculation. The peak interval between the positive and negative polarity can be reduced by using microring with smaller diameter as confirmed by our calculation. Since the concave substrate has a 12.92 mm radius-of-curvature, the focal spot in theory should appear around 8.61~8.73 μs with the sound speed of 1480~1500 m/s in water. We used 1494.7 m/s in the calculation to fit the measured waveform in Fig. 4.1(b). The waveform distortion may be due to the non-perfect spherical shape of the glass substrate (~1%) and the misalignment of the microring in the axial direction (tilt angle ~2.4°, as confirmed by the scanning along the *z*-axis).

Figure 4.2 shows the spatial profile of the focused ultrasound measured by scanning the microring at the focal plane. Each data point in the plot represents the absolute peak value of the time-domain signals measured at each spatial location. Interestingly, the 1-D profile of the focused ultrasound as detected by a 50-μm radius microring shows three peaks: a main peak located at the center and two secondary peaks located 50 μm from the center that coincide exactly with the position of the ring waveguide that is symmetric from the center. The FWHM of the central peak was 41 μm. This result implies that the microring detector may be able to measure objects whose size is smaller than its diameter. In Fig. 4.1(b), we also show the simulated pressure profile. The microring responses were relatively weak at the shoulder peak positions than at the center. It will be shown that the detector at these locations has more attenuation over high frequency components (the section of Fig. 4.4).

4.3.2 Frequency-Dependent Profiles of Focused Ultrasound

To better understand the origin of the three peaks, we reconstructed the spatial profiles of several harmonic frequency components in Fig. 4.3. For 10 MHz component as shown in Fig. 4.3(a), only a single spatial peak is observed. This can be understood because the acoustic wavelength for <15 MHz frequency is larger than the ring diameter. However, for higher frequency components with much reduced acoustic wavelength, the contour of the ring waveguide becomes distinct and should be reflected in the microring response. As the high frequency focused acoustic wave (*i.e.* with small wavelength) is scanned at the focal plane, it can intercept the ring-shaped waveguide twice, which results in two shoulder peaks. The shoulder peaks become very clear as the ultrasound frequency is greater than 20 MHz. The widths of shoulder peaks for 30 and 50 MHz are 36 and 22 μm, which agree within ±2 μm deviation with the calculated main lobe sizes.

This agreement is due to the narrow waveguide width which is much smaller than the acoustic wavelengths in the range of interest. On the other hand, the existence of the central peak may not be apparent at the first sight, as the main lobe does not overlap with the microring waveguide. We will show by calculation that it is the side lobes of the focused ultrasound interacting with the circumference of the microring waveguide that contribute to the main peak. In Fig. 4.3(b) and (c), we show the results of 2-D spatial convolution of the calculated side lobes with microring. In calculation, only 1st order side lobes were considered for 30 MHz, and 2nd order lobes for 50 MHz. All other lobes (including the main lobes) were intentionally omitted to manifest the effect of side lobes

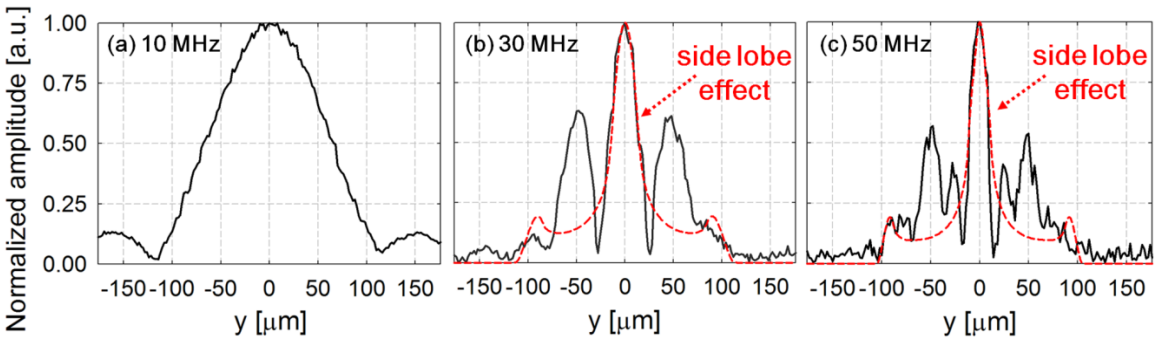

Fig. 4.3 Normalized spatial profiles reconstructed by the amplitudes of harmonic frequency components 10, 30 and 50 MHz from Fig. 4.2(b). The dotted profiles were calculated by spatially convolving the side lobes of the focused ultrasound with the microring geometry. Only the first order side lobe was used in (b), and the second order in (c). The widths of the experimental main peaks agree with those of the dotted profiles.

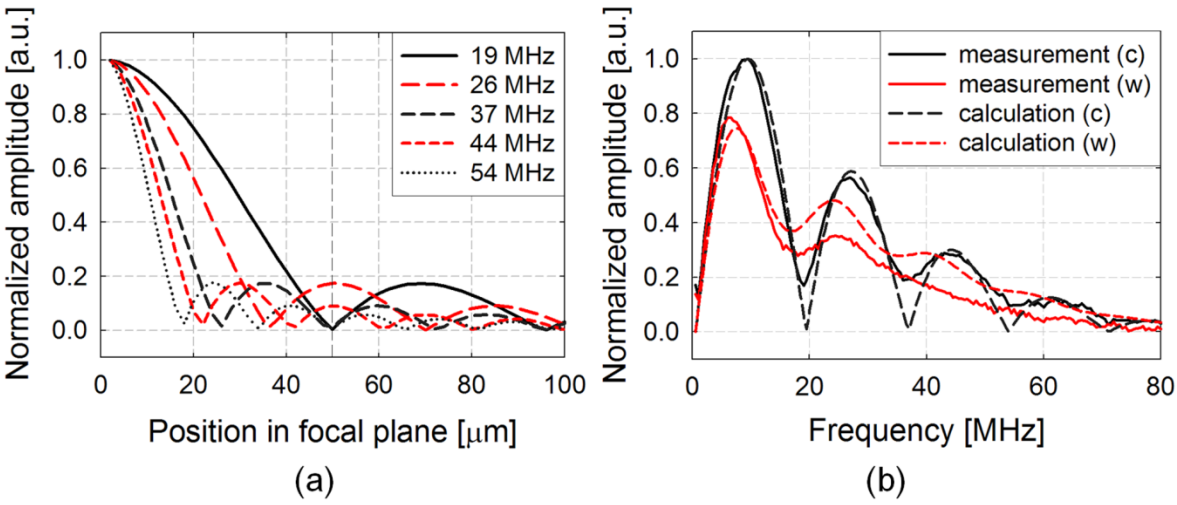

Fig. 4.4 (a) Calculated profiles of the focused ultrasound for several harmonic frequencies at the focal plane. The location of the microring waveguide is marked at 50 um. The side lobes of the focused ultrasound reach maxima at the location of the waveguide at 26 and 44 MHz (red), and minima at 19, 37, and 54 MHz (black). (b) The signal spectra at the location of the ring center (black, denoted as c) and the waveguide (red, denoted as w). These were obtained by Fourier transformation of the time-domain waveforms of microring output (solid) and the calculated pressure (dotted).

crossing the location of waveguide. The FWHM of the main peaks at these frequencies exactly agree with the spatial convolution result. This validates that the side lobe from the focused ultrasound is responsible for the appearance of the main peak. This effect can be significant because the side lobe of the focused ultrasound is integrated over the whole circumference of the ring waveguide.

The detection mechanism can be further explained by considering the frequency spectra of the signal together with the spatial profiles of focused ultrasound. Fig. 4.4(a) shows the calculated profiles of the focused ultrasound for several harmonic components. Because the main lobes for the harmonic components with <19 MHz are larger than the ring diameter and have direct overlap with waveguide, the detection of the focused ultrasound is primarily based on the main lobes. However, for >19 MHz, it is shown that the side lobes of the 26 and 44 MHz components reach maxima at the location of ring waveguide while those of 19, 37, and 54 MHz reach minima. This effect is consistent with the experiments and is verified in the frequency spectra of measured signals in Fig. 4.4(b). These frequency spectra are obtained by taking the Fourier transform of the time-domain waveforms measured where the ultrasound focus is at the ring center and at the waveguide. As expected, the spectrum measured at the ring center shows pronounced enhancement around 26 and 44 MHz, which is in contrast to the spectrum at the location of ring waveguide. The spectral dips were also observed around 19, 37, and 54 MHz because the ultrasound side lobes in these frequencies have minima. We note that this spectral feature can be seen because the spatial widths of side lobes are resolved by the narrower width of ring waveguide. In Fig. 4.4(b), the simulated spectra for the focused ultrasound (integrated over the ring position) are also shown. At the ring center, the

calculated spectrum is quite close to the measured one. But at the ring waveguide, the measured spectrum is attenuated over a broad range as compared to that of the calculated one. When the main lobe of the high frequency ultrasound is focused to a certain section of the ring waveguide, its side lobes are simultaneously incident on the other positions of the ring. Such side lobes can have opposite polarity against the main lobe. This can cause optical modulation of the microring to be less efficient due to destructive contribution. This is contrasted to the case at the ring center where the side lobe is incident in-phase along the ring circumference, so that the constructive contribution through the whole ring maximizes the optical modulation.

4.3.3 Recovery of Original Focal Spot Profile by Spatial Deconvolution

As the optical microring detector has a finite size and a specified shape, the imaging result is affected by such geometrical effect where the acoustic wavelength is smaller than or comparable to the detector dimension. For low frequency where the wavelength is much larger than the detector size, the microring works close to a point detector because the acoustic wave slowly varies in phase over the detector. Therefore, for high frequency detection, a proper step of spatial processing is required to remove the detector geometry effect. At each temporal frequency, the measured image in the experiment is the result of spatial convolution of the original pressure distribution with the detector geometry. Here, we assume that the microring detector has a 2-D shape as the waveguide height (2 μm) is sufficiently smaller than the acoustic wavelengths. Then, the 2-D spatial convolution process is described as

$$P(x,y) \otimes D(x,y) = Q(x,y) \tag{4.1}$$

where *P(x,y)* is the 2-D distribution of original pressure, *D(x,y)* is the geometry of the microring detector, and *Q(x,y)* is the measured image. Using the eq.(4.1), we could extract *P(x,y)* by deconvolving *Q(x,y)* with *D(x,y)*.

For the optoacoustic concave transmitter, the focal point is formed at the center of spherical curvature because the generated pressure has a complete spherical wavefront. Fig. 4.5(a) is an image on the focal plane (at a distance of the lens radius). In Fig. 4.5, we show the measured image, the 2-D profile of microring used in the calculation, and the recovered image of the focused pressure distribution. The measured image in Fig. 4.5(a) contains the effect due to the microring geometry. In Fig. 4.5(a), the measurement resolution was 4 μm in both *x*- and *y*-directions. In Fig. 4.5(b), the microring geometry was represented in 2 μm resolution. For the microring calculation, we assumed spatial amplitude of 1 at the location of microring waveguide and 0 elsewhere. The waveguide was described approximately as a single line in the figure as the width of microring waveguide is ~2 μm. For spatial signal processing, both Fig. 4.5(a) and Fig. 4.5(b) should have the same resolution in space. To meet this condition, the resolution in Fig. 4.5(a) was improved to 2 μm by interpolation. We inserted an interpolated value between adjacent pixels (*i.e*. an average value between two neighbors). The shape of the microring would have been more circular if we had used a higher resolution grid. However, we avoided it because more interpolation steps are required to the original data. Higher resolution scanning (<2 μm) in the original measurement is possible but this requires long

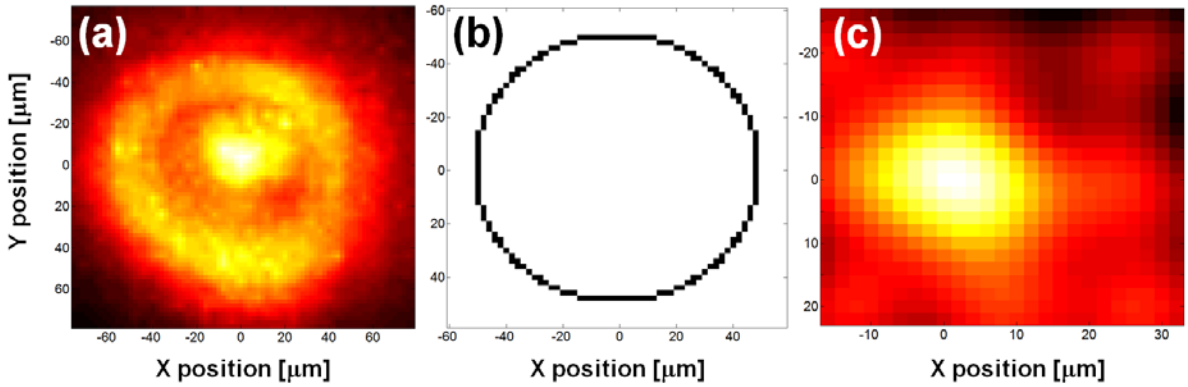

Fig. 4.5 A focused ultrasound image by optoacoustic concave transmitter. (a) An original image including the geometry effect of the optical microring detector, (b) a microring detector profile used in the deconvolution process, and (c) a recovered image of focused pressure. The pixel resolution is 2 μm by 2 μm for all cases. Note that the spatial dimensions displayed in (c) are different.

measurement time (~several hours) as the number of pixels increases. However, such long time measurement was not desirable due to a thermal stability issue in the detector. In Fig. 4.5(c), the deconvolution result is shown. Based on the spatial processing method, we extracted the spot width of the concave transmitter, ~44 μm. The deconvolution process reveals that the spot width is obviously smaller than the microring diameter as the focused ultrasound has high-frequency components (*i.e.* acoustic wavelengths smaller than the microring diameter).

4.4 Conclusion

The responses of optical microring detector have been characterized by using

high frequency focused ultrasound. The optoacoustic concave transmitter has been used as a broadband and high frequency focused source. As the focused ultrasound is scanned by the microring in the focal plane, two types of spatial peaks are observed: (1) shoulder peaks at the ring waveguide that result from direct overlap of the main lobes of the focused ultrasound with the ring waveguide, and (2) a main peak at the ring center that is contributed by both the main lobes of low frequency components and the side lobes of high frequency ones. Detection of the shoulder peaks means that even a part of the microring waveguide (several μm^2 in area) has substantial sensitivity. Therefore, a practical imaging with any features smaller than the ring diameter would require a spatial deconvolution process after measurement, which includes all the contribution over the ring circumference. As the measured spatial profile includes the geometrical effect of microring, we could extract the original focused image by performing 2-D spatial signal processing.

References

[1] S.-W. Huang, S.-L. Chen, T. Ling, A. Maxwell, M. O′Donnell, L. J. Guo, and S. Ashkenazi, Appl. Phys. Lett. 93, 113501 (2008).

[2] E. Zhang, J. Laufer and P. Beard, Appl. Opt. 47, 561 (2008).

[3] C. Y. Chao, S. Ashkenazi, S.-W. Huang, M. O'Donnel, and L. J. Guo, IEEE Trans. Ultrason., Ferroelect., Freq. Contr. 54, 957 (2007).

[4] A. Maxwell, S.-W. Huang, T. Ling, J.-S. Kim, S. Ashkenazi, and L. J. Guo, IEEE J. Select. Topics Quantum Electron. 14, 191 (2008).

[5] S.-W. Huang, Y. Hou, S. Ashkenazi, and M. O′Donnell, Appl. Phys. Lett. 92, 193509 (2008).

[6] G. Paltauf, R. Nuster, M. Haltmeier, and P. Burgholzer, Appl. Opt. 46, 3352 (2007).

[7] C. Y. Chao and L. J. Guo, J. Vac. Sci. & Technol. B 20, 2862 (2002).

[8] R. S. C. Cobbold, *Foundations of Biomedical Ultrasound*, Oxford University Press, New York (2007).

Chapter V

Optoacoustic 4f Imaging by using Polymer Microring Detectors

5.1 Introduction

In the previous chapter, we have shown the high-frequency characteristics of optical microring detectors. The frequency-dependent performance has been characterized using the focused ultrasound with broadband frequency components. The results suggest that the optical microrings are suitable for applications which require detectors with high sensitivity and small physical dimension. Such properties are highly desirable in some configuration which receives high-frequency ultrasound coming from broad angles of incidence. In this chapter, we demonstrate a novel optoacoustic imaging system using the microring detector and the acoustic 4f lens.

An optical 4f imaging is capable of mapping spatial information in an object plane onto an image plane with one-to-one correspondence [1]. Due to the spatial Fourier transform property of lens, unit magnification in axial and lateral directions between the object and the image is preserved. Such a feature is very attractive for fast 3-D imaging without complex reconstruction process. A similar concept has been recently introduced for optoacoustic imaging [2]. However, the imaging resolution in that system was very

low to 3~4 mm (lateral) due to low operation frequency and limited bandwidth of detector. As the 4f imaging system adopts two focusing lenses and its imaging is based on the collection of focused point images, a small size acoustic detector such as the microring is desirable to achieve high-spatial resolution. Moreover, a broadband response of the detector gives a significant benefit for optoacoustic imaging. High-frequency ultrasound over several tens of MHz is required to recognize the fine feature of objects while low frequency, <5 MHz, is still needed for smooth parts of the structures [3]. However, both cannot be satisfied in most of piezoelectric transducers which have limited bandwidths around their specified central frequency which is low or high. Therefore, it is difficult to achieve high-resolution in fine dimensions together with preserving large scale structures close to the original shape of the objects.

We propose a novel 4f imaging system by using the microring detector that satisfies the above requirements in terms of small detector dimension and broadband frequency responses. Two different systems were designed for long-range and short-range optoacoustic imaging. The long-range system was developed for an initial demonstration of the 4f imaging which includes an acoustic lens with 39 mm in focal distance and a microring detector of 100 μm in diameter (quality factor Q ~ 5000 at optical resonance) [4]. In the short-range system, another acoustic lens was designed to have 6.5 mm in focal distance. High-frequency performance was greatly enhanced due to two reasons: (1) a short focal distance and therefore reduced attenuation along acoustic propagation path, and (2) a new microring detector with smaller dimension of 40 μm in diameter and higher quality factor of Q ~ 30000 [5]. The high-frequency 4f imaging has been demonstrated using micro-scale objects. This reveals that the spatial resolution in our configuration is at

least 10-fold better than that of the existing 4f imaging system which uses piezoelectric transducers.

5.2 Design of Acoustic 4f Imaging System

5.2.1 Acoustic 4f Lens and Measurement Setup for Long-Range Imaging

We used acryl to fabricate the 4f lens because it has low acoustic attenuation and high transmission coefficient (~0.94) at the interface of acryl and water. The lens has a symmetric bi-concave shape (18 mm in radius-of-curvature and 35 mm in aperture diameter) and a wide aperture angle, ~153.3°. Distance from the edge of lens rim to the focal plane was 25.1 mm. The focal length of the lens was obtained by lens maker′s formula,

$$\frac{1}{f} = (n-1)\left(\frac{1}{r_1} - \frac{1}{r_2}\right) \tag{5.1}$$

where f is the focal length, n is the acoustic refractive index, and r_1 and r_2 are the radii-of-curvature for front and back surfaces. Here, the focal length f = 38.98 mm in the water was obtained by taking r_1 = 18 mm and $r_2 = \infty$. The sample is located at the front focal plane (object plane) and the detector at the back focal plane (image plane) (Fig. 5.1). The 4f imaging system gives an image which is spatially reversed to the object at the image

plane. Therefore, it eliminates the need of an image reconstruction step after data acquisition, which is typically required in conventional imaging systems. Moreover, the current configuration allows 3-D imaging in principle as elevation information can be obtained by converting time-of-flight of ultrasound into the corresponding axial distance. Two polymer microspheres with 301 μm in diameter (Thermo Scientific Inc., Waltham, MA) were used as light-absorbing objects. The microsphere has a polystyrene-based copolymer structure including a light-absorbing group which is uniformly distributed in the sphere. The microspheres were fixed onto an epoxy-coated glass substrate by UV-curing process. The epoxy (NOA 61, Norland Products Inc., Cranbury, NJ) is optically

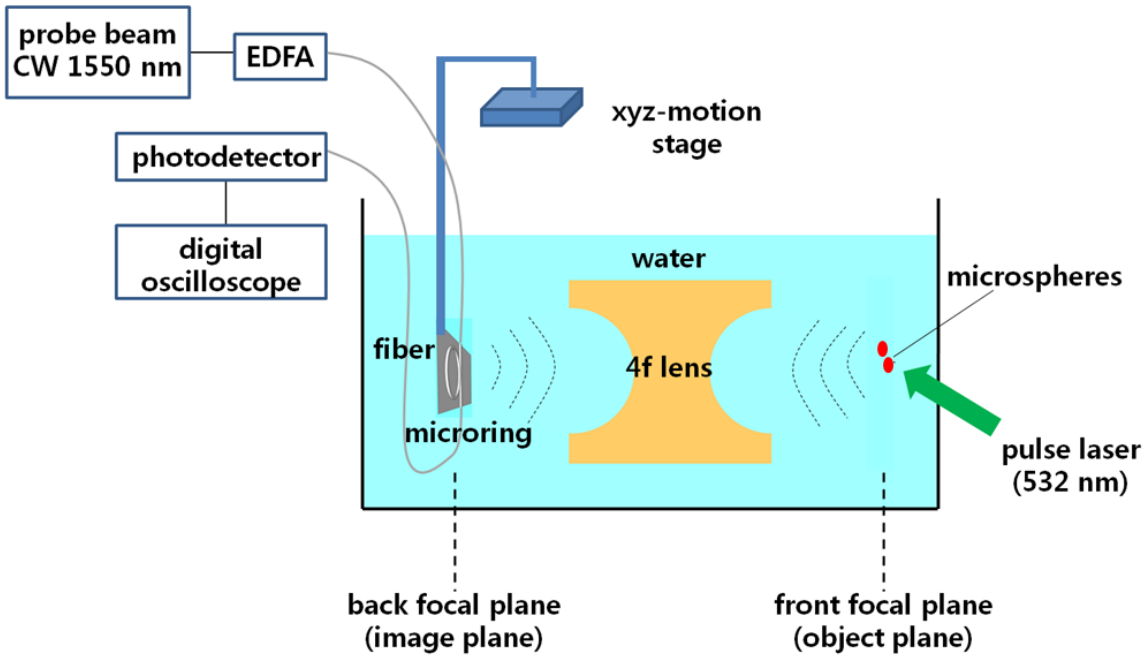

Fig. 5.1 Schematic of 4f imaging setup. The microspheres and the microring detector are located at the front and back focal planes, satisfying the 4f imaging condition. The probe laser beam, the digital oscilloscope, and the *xyz*-motion stage are controlled by computer.

transparent giving a high optical contrast against the microspheres. Approximately, half of the microsphere was embedded in the epoxy layer while the other half was exposed to water. Fig. 5.1 shows an experimental schematic for 4f imaging system based on the microring detector. The 4f image profile was measured by scanning the detector at the back focal plane using motorized motion stages while the objects were fixed at the front focal plane.

5.2.2 Acoustic 4f Lens and Measurement Setup for Short-Range Imaging

A separate experiment was performed by using another 4f imaging setup designed for short-range and high frequency imaging. A basic geometrical arrangement is identical with the one in Fig. 5.1. However, the scale of the 4f lens was reduced for high frequency imaging. The lens was designed to have a focal distance of 6.5 mm in water.

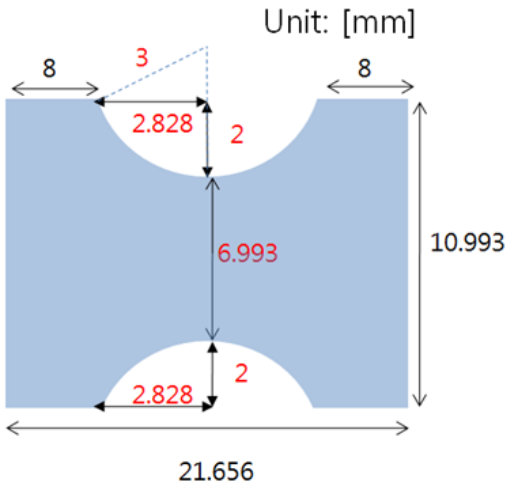

Fig. 5.2 A short-range version of acoustic 4f lens for high frequency imaging. The focal distance is 6.5 mm in water.

Also, we used a microring detector with higher sensitivity (Q~30000, diameter = 40 μm) than in the previous case (Q~5000, diameter = 100 μm). Fig. 5.2 shows the detail dimension of the 4f lens used in this system. Two polymer microspheres with 96 μm in diameter were used for optoacoustic imaging. The microspheres were fixed by using Agarose gel (2 wt% in water) and separated by 0.55 mm. Then, the gel was embedded in water. The 3-D optoacoustic imaging was performed for these microspheres by using the short-range 4f configuration.

5.3 Long-Range 4f Imaging by Using Optical Microring Detectors

In the long-range configuration of 4f imaging system, the available frequency spectrum of measured signal was limited to ~20 MHz. This is mainly because of the acoustic attenuation for long distance propagation across lens and water.

Fig. 5.3 shows the images obtained by the long-range system. Two microspheres with 301 μm in diameter were ~1.4 mm apart from each other. The image was obtained by taking peak values of time-domain signals in each position. The total imaging time depends on the number of pixels, the number (10~30) of signal averaging in each pixel, and the sweeping time of *xy*-manipulator over the imaging range. The experiment was carried to obtain a 2-D image including ~1600 pixels. In Fig. 5.3, the image amplitudes between the two microspheres were different (*i.e.* the bottom one is brighter than the upper in Fig. 5.3(a)) due to the non-uniform spatial intensity distribution of pulsed laser

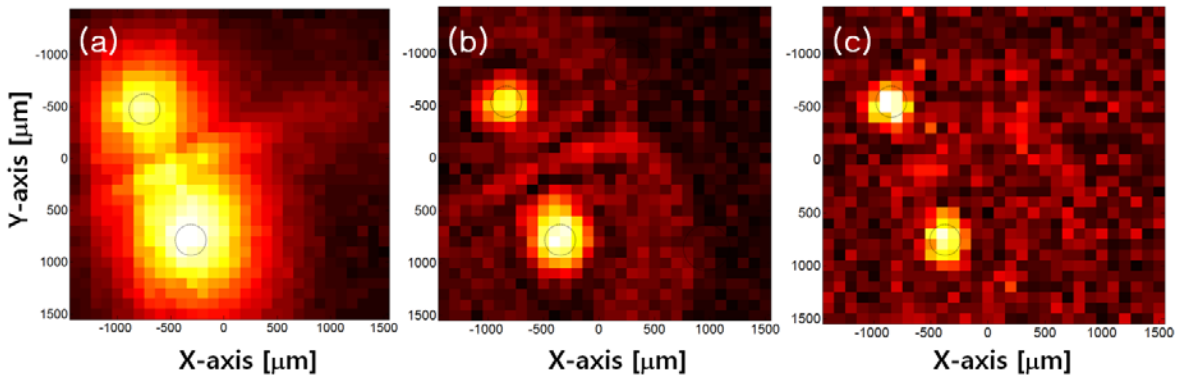

Fig. 5.3 2-D image of two black polymer microspheres with 301 μm in diameter. These are 1.4 mm apart. Each pixel size is 100 μm × 100 μm: (a) 4f image measured by the microring detector. The contour for the original sphere size is shown as the black circle, (b) and (c) the images obtained by harmonic frequency components of 10 MHz and 15 MHz. The image in (c) becomes sharper while the background noise is increased.

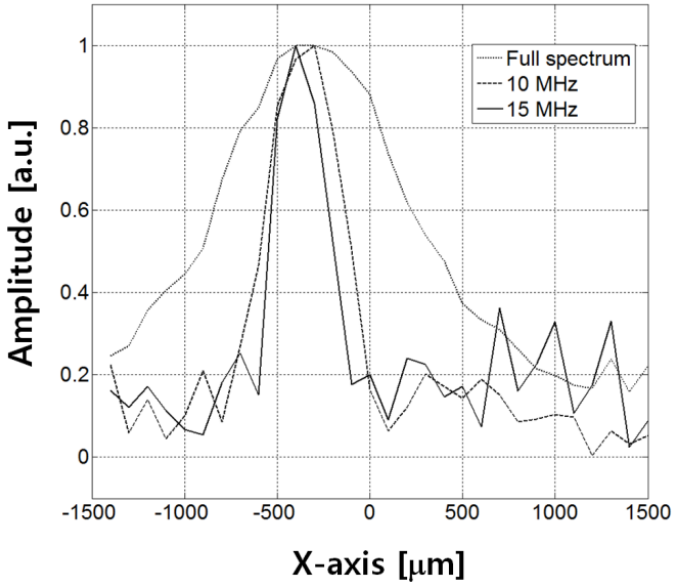

Fig. 5.4 1-D spatial profiles across the center of the bottom microsphere shown in Fig. 5.3. Three profiles were obtained from Fig. 5.3(a), (b), and (c). Each trace is normalized to its peak amplitude. The FWHMs were 1330 μm, 440 μm, and 370 μm, respectively. For the 15 MHz case, the background noise is increased, which makes the signal peak-to-background noise ratio ~3.

beam. The 300 μm contour lines are also shown. In this full spectrum image, the detected

signal is dominated by low frequency range < 5 MHz (shown in Fig. 5.3(a)). As a result, the image is broader than the nominal size of the microsphere. Two microspheres were distinguished more clearly in the high frequency image shown in Fig. 5.3(b) and (c). To obtain these images, we first obtained a frequency spectrum of the time-domain signal in each pixel of Fig. 5.3(a), and then chose the amplitude of a specific harmonic component to construct the pixel image. This process was applied for all pixels. Here, the images for 10 MHz and 15 MHz are shown as examples. The image size becomes close to the contour of the bead because the sharp boundary of the beads is characterized by high frequency components. For >20 MHz, the image contrast was rapidly degraded to <3 (the ratio of the peak value to the background noise). The 1-D cross-sectional profiles across the center are shown in Fig. 5.4. The FWHMs for these profiles were ~1330 μm (full), 440 μm (10 MHz) and 370 μm (15 MHz), respectively. The time-domain signal at the center of microsphere image is shown in Fig. 5.5(a). The waveform is the result of mixed acoustic signals from two microspheres, aberration in the lens system, and possible misalignment. In Fig. 5.5(b), the corresponding frequency spectrum is shown. High-frequency information (>15 MHz) in the signal was strong where the object and the image were placed around the focal points. The spectrum has a peak around 3~4 MHz and extends up to 20 MHz, covering both low and high frequency spectral ranges. The frequency response (especially, the high-frequency components) and the system resolution were limited by the following loss mechanisms: attenuation in the lens medium (6.4 dB/cm at 5 MHz [6]), boundary reflections at both front and back lens surfaces, and absorption in water (0.05 dB/cm at 5 MHz).

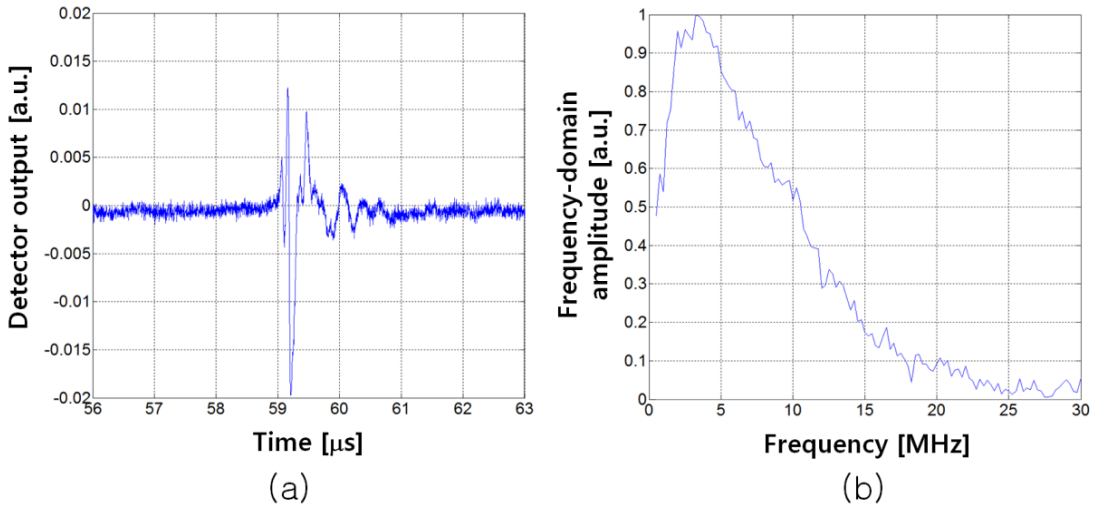

Fig. 5.5 (a) Time-domain waveform at the peak position of spatial image, and (b) the corresponding frequency spectrum.

The imaging capability of the 4f lens system was investigated using a single hair of 100-μm diameter which generates weaker optoacoustic pressure amplitudes than the previous microspheres of 300-μm diameter. The 6-dB cut images are shown in Fig. 5.6(a) for XY-plane and in Fig. 5.6(b) YZ-plane. We applied two different band-pass filters to examine frequency-dependent image quality. As the hair diameter is similar with the acoustic wavelength corresponding to 15 MHz frequency, we used two filter regimes of lower and higher than 15 MHz frequency. In the high-frequency filtering (35~45 MHz), the image should be able to provide clear definition of the single hair. However, the hair diameter was observed as 200 μm which is just slightly smaller than the low-frequency filter image with 230-μm diameter. As confirmed in the previous microsphere imaging, the high-frequency acoustic waves are severely attenuated in the long-range system. Therefore, better image quality would be obtained if we can either generate stronger

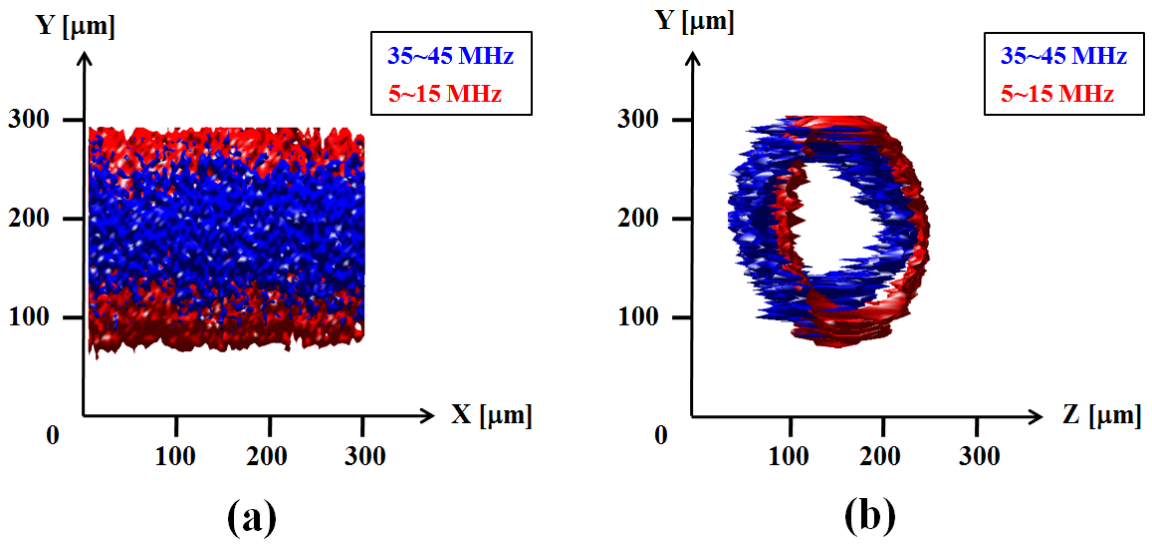

Fig. 5.6 A single hair image (originally, 100-μm diameter) obtained by the long-range 4f lens system. The 2-D images are shown: (a) longitudinal direction and (b) cross-sectional view. Two different band-pass filters were applied over low frequency (5~15 MHz) and high frequency (35~45 MHz). But the imaging results are similar.

amplitudes in the high-frequency ranges or receive them more sensitively. In the following section, we will show that the high-frequency performance is greatly enhanced in the short-range imaging system.

5.4 Short-Range 4f Imaging by Using Optical Microring Detectors

In the short-range imaging system, the acoustic attenuation for high-frequency ultrasound is greatly reduced due to the short focal distance (6.5 mm). This makes the 4f lens deliver stronger pressure amplitudes to the detector. Moreover, we used an improved optical microring detector which is suitable for the focal imaging system. The new

microring was fabricated to have smaller dimension (40 μm in diameter) and higher sensitivity (Q~30000) [5]. An angular response of the detector was improved with the decreased dimension. This means that the detector can receive high-frequency acoustic waves with reduced loss, which come from broad angles of incidence. The improved angular response is significant in the 4f imaging system because the ultrasound comes into the detector in a spherically focused way from the lens aperture. The enhanced

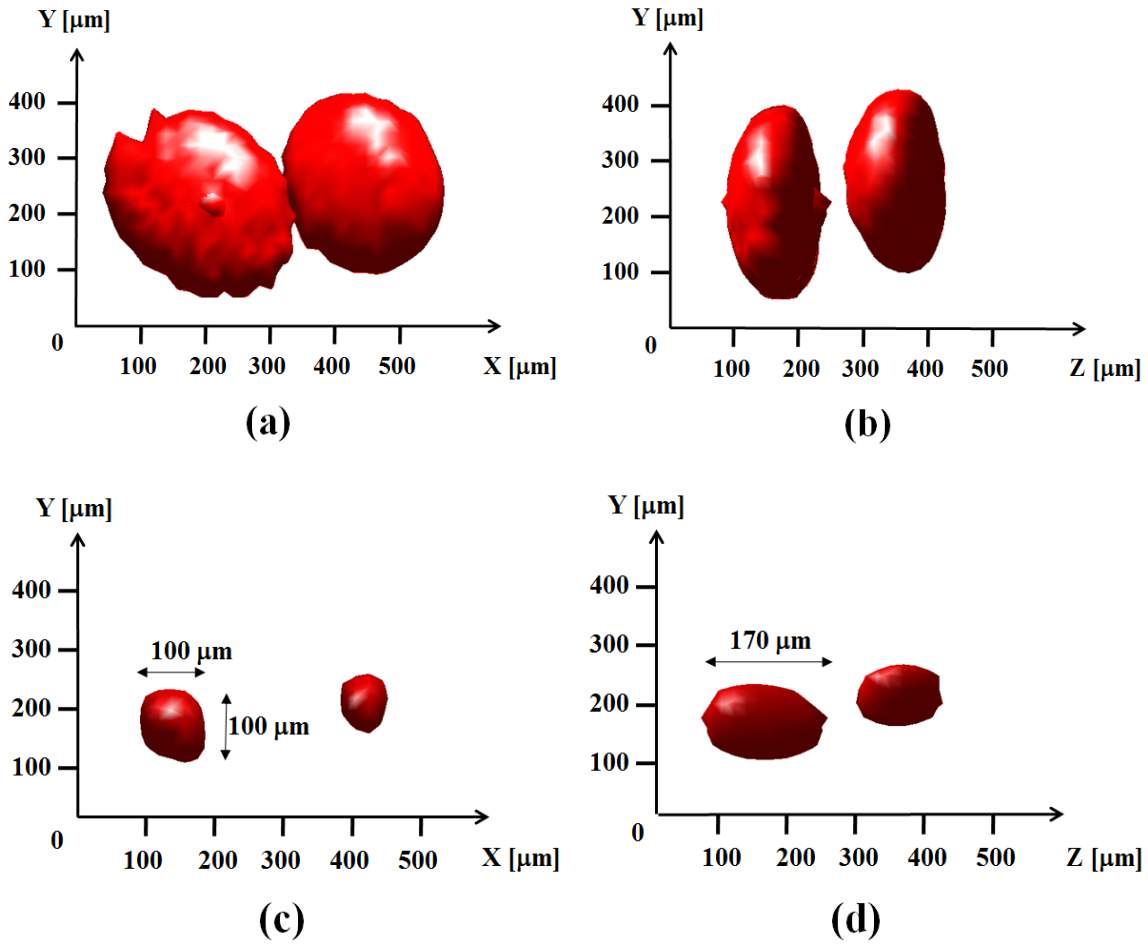

Fig. 5.7 2-D images of two polymer microspheres (100 μm) obtained by the short-range 4f lens system. Two different band-pass filters were applied: low frequency (5~15 MHz) for (a) and (b), and high frequency (35~45 MHz) for (c) and (d). Improvement in the image quality is clearly observed.

sensitivity is also highly desirable for detecting weak amplitudes of high- frequency ultrasound. Consequently, we can expect better imaging performance compared to the previous long-range case.

Figure 5.7 shows the 6-dB cut of 4f images for two microsphere beads with 100 μm in diameter. While the microspheres are seen as ~300 μm in the low frequency images in (a) and (b), they are resolved as exactly 100 μm in the high-frequency image shown in (c). This means that the resolution limit would be even lower than 100 μm. In Fig. 5.7(d), we observed elongation of the bead image to some extent along the axial direction of the lens, which results in 170-μm diameter. This is probably due to limitation in the depth of lens focus and alignment errors (*i.e.* the detector may not be exactly at the focal plane of the 4f lens). However, we could confirm the significant improvement in the image quality for both Fig. 5.7(c) and (d). This is due to the improved detector performance and the short focal length of the lens. Here, both beads have an identical size, but the optical absorption at each bead is initially different due to non-uniform laser intensity distribution. We normalized the image amplitude to the left bead in Fig. 5.7 which has stronger absorption and optoacoustic signal. The bead dimension was also determined by the left bead.

5.5 Discussion

We have demonstrated the high-resolution optoacoustic 4f imaging systems by

using the microring detectors. However, the 4f arrangement has several loss mechanisms which should be resolved for practical utilization in future. First, the acoustic waves experience high attenuation through the long propagation distance in water and lens medium, strong reflection at the lens/water interfaces, and focal distortion due to lens aberration. As the lens material, we used the acryl to reduce the boundary reflection, considering the acoustic impedance matching with water: Z_{acryl} = 3.22 [MRayl] and Z_{water} = 1.48 [MRayl]. However, the high-frequency ultrasound is severely attenuated through the thick acryl medium. This significantly reduced the optoacoustic signal especially in the long range system. In applications of scanning acoustic microscopy, ZnO and Al_2O_3 are often used as acoustic lenses to reduce the high-frequency loss. While these materials allow high-frequency transmission up to hundreds of MHz, their acoustic impedances do not have good matching with water (Z_{ZnO} = 36.4 [MRayl] and $Z_{Al_2O_3}$ = 40 [MRayl]). An additional matching layer ($\lambda/4$) on these lens surfaces may be considered to reduce the boundary reflection. But this approach is not desirable because the acoustic frequency would also be determined together with the layer thickness. Consequently, we would lose the broadband frequency characteristic which is one of the main advantages in our configuration.

Moreover, the 4f imaging system has an issue of the microring responses. As shown in the previous chapter, the spatial response of the microrings depends on the focal spot dimensions. The spatial deconvolution can be used to recover the correct pressure profile and amplitude, but this would give an additional complexity upon the imaging system. Smaller microrings, compared to the focal widths, are highly preferred to take the full benefits of high-frequency responses and fast 3-D imaging without considering the

mathematical recovery step.

5.6 Conclusion

The optoacoustic 4f imaging systems have been proposed using the microring detector and the bi-concave lens. The long-range and the short-range systems were demonstrated for optoacoustic imaging of micro-scale objects. The long-range system could resolve two microspheres (each 300 μm in diameter) located at the long focal distance of 39 mm. The FWHM of the image obtained at the 15 MHz frequency was ~370 μm, which is close to the nominal size of the microsphere. However, for a smaller object which is a single hair of 100-μm thickness, the long-range system could not provide clear definition of the object due to weak optoacoustic pressure amplitudes, especially for the high-frequency range. In the short-range system, the high-frequency performance was significantly improved. This is because the system consists of (1) the smaller microring detector (40 μm in diameter) together with higher sensitivity (Q~30000) and (2) the short focal distance of the 4f lens which reduces the acoustic attenuation effect as compared to that of the long-range 4f lens. The microspheres of 100-μm diameter were clearly resolved in the short-range imaging system by using the band-pass filter over 35~45 MHz frequency range. The lateral dimension (100 μm) at the focal plane was exactly same with the nominal size of the microspheres, but the image along the axial direction of the lens was distorted to 170 μm. It is possibly due to the limited

depth of focus in the 4f lens and misalignment among the detector, the 4f lens, and the objects.

References

[1] J. W. Goodman, *Fourier Optics*, 3rd edition, Roberts & Company Publishers, Colorado (2004).

[2] Z. Chen, Z. Tang, and W. Wan, Opt. Express 15(8), 4966 (2007).

[3] S.-L. Chen, S.-W. Huang, T. Ling, S. Ashkenazi, and L. J. Guo, IEEE Trans. Ultrason., Ferroelect., Freq. Contr. 56, 2482 (2009).

[4] S.-W. Huang, Y. Hou, S. Ashkenazi, and M. O′Donnell, Appl. Phys. Lett. 92, 193509 (2008).

[5] T. Ling, S.-L. Chen, and L. J. Guo, Appl. Phys. Lett. 98, 204103 (2011).

[6] A. R. Selfridge, IEEE Trans. Sonics and Ultrasonics Su-32(3), 381 (1985).

Chapter VI

Concluding Remarks and Suggestions for Future Work

6.1 Thin-Film Optoacoustic Transmitters for High-Frequency and High-Amplitude Focused Ultrasound

For optical generation of ultrasound, we demonstrated thin-film transmitters made by using CNT-polymer composites which are capable of generating strong and high frequency pressure. These transmitters satisfy most of the conditions for highly efficient optoacoustic generation. In terms of optoacoustic material, the CNTs have low density (1/7 of the gold) and fast heat conduction (an order of magnitude higher thermal conductivity than in the gold). They could be grown in highly packed manners, which is not easy in other materials and approaches. Their uniform distribution over the substrate is an additional advantage. In the composite film form, they form a densely-packed thin layer near the substrate. These enable high optical absorption over the thin layer (≈ effective absorption depth). Moreover, the CNTs are surrounded by the elastomeric polymer with high thermal expansion (5-fold higher than water), the temperature increase in the CNTs could be very efficiently converted to volume deformation.

As these properties in the CNT-polymer composites work as enhancement factors in optoacoustic pressure outputs, we could generates 18-fold stronger amplitudes than

that of the Cr film case and even 5-fold stronger than that of the AuNP composite with the same polymer. This enhancement persisted over a broadband frequency range up to 120 MHz. Using an 1-D layered model, we estimated and verified the optoacoustic generation performance theoretically. As thermal transfer media, various polymers were investigated, and then we confirmed that the PDMS enables most efficient transfer due to the high thermal expansion. The CNT-PDMS composite films were further improved by using a thin gold. The thin gold (20~30 nm) was deposited over the CNTs before forming the composite with the polymer. This significantly improved the pressure output because (1) the increase in the absorption cross-section at the individual CNTs, and (2) the formation of random nano-structures of the gold on the substrates which work as an additional source for optical absorption. Depending on initial CNT densities, the optoacoustic pressure amplitudes were improved by 1.2-fold ~ 9.2-fold. We also confirmed that the composite film has high damage threshold for laser-induced thermal ablation. It was 8.5-fold higher than those of other metal-based sources. This is important because this can increase the available excitation energy in the pulsed laser. Then, the ultimate achievable pressure is increased by the available laser energy without destroying the transmitters.

Based on the great enhancement by using the CNT-polymer composites, we presented a new approach for generation of high-frequency and high-amplitude focused ultrasound in a non-invasive and non-ionized way. We designed and fabricated the optoacoustic focusing lenses. The composite films of gold-coated CNT-PDMS were formed on the concave substrates. Under the pulsed laser excitation, the optoacoustic pressure was generated and focused from the concave surfaces. At the lens focus, we

could generate unprecedented optoacoustic pressure amplitudes, simultaneously achieving tight focal spots which are an order of magnitude smaller than those of the traditional low-frequency HIFU transducers. We obtained strong positive peaks of 58 MPa at the tight focal spot of 75 μm in lateral and 400 μm in axial directions. The pronounced shock waves were formed at the short focal distance of ~5.5 mm. In the negative pressure, the measurable peak amplitudes were limited to ~13.7 MPa for the laser energy of 14 mJ/pulse (type I lens) and 10 mJ/pulse (type II lens). This is due to the measurement limitation because the acoustic cavitation is involved at these pressure levels on the fiber surface and then distorts the waveforms in the negative phase. Higher than 25 MPa in the negative peak is possibly reached if the pressure amplitudes are extrapolated over the high laser energy.

As the main features of the optoacoustic focusing lens, we suggested high geometrical gain and strong shock formation in the short distances. The high geometrical gain is primarily due to high-frequency nature of laser pulses and low *f*-numbers in the lens geometry. Since the CNTs can be grown on arbitrary curvatures, we can make the low f-number focusing lenses without difficulty even in small dimension of several millimeters. These high-frequency and high-gain characteristics also enable strong shock formation in the short distance of ~5 mm. This can be even shorter depending on the lens design. High surface pressure is another reason due to the efficient optoacoustic energy conversion in the CNT-PDMS composites and the narrow temporal width in the laser pulses. We emphasize that the output performance of the optoacoustic focusing approaches is not limited to the current experimental results specifically obtained from the type I and II lenses. The optoacoustic focusing has great flexibility in terms of

transmitter designs and excitation laser choices to control ultrasonic frequencies, amplitudes, and intensities.

6.2 Nonlinear Induced Effects: Shock Waves and Acoustic Cavitation

The acoustic cavitation and shock-wave behaviors were verified using various experimental methods. The cavitation bubbles were visualized by the high-speed camera recording, revealing the existence of multiple bubbles on the fiber surface. The bubbles were correlated with the distortion in the acoustic signal waveforms. These were detected only when they were in contact with the fiber core. The multiple bubbles were further characterized in terms of lifetime. The collapse time of micro-bubbles was typically <15 μs for the low laser energy range of <40 mJ/pulse. The LGFU-induced shock waves and acoustic cavitation were used for micro-scale fragmentation of the artificial stone and the polymer film. Although the optoacoustic focusing makes tighter focal spots temporally and spatially than the conventional HIFU, the generated ultrasound was strong enough for the stone lithotripsy. The accurate control was possible with the fine patterns less than 500 μm in width. The cavitation-induced enhancement was confirmed in the fragmentation process of the polymer film. The cavitation behavior was further investigated under the condition of much higher negative pressure. We could observe the micro-bubbles which have the long lifetime of several seconds. These are distinguished from the previous cases obtained under the low laser energy. However, despite such

highly negative amplitudes, the acoustic cavitation still needed the solid boundaries. As the possibility of free-boundary cavitation becomes a subject of interest, we demonstrated superposition of two focused ultrasonic waves: one from the optoacoustic transmitter and the other from the traditional piezoelectric transmitter operating at 3.5 MHz with the negative amplitude of -5 MPa. The low-frequency transmitter provided weak pressure by itself to induce the cavitation. Under the superposition the ultrasonic waveforms have broadened profiles, but the acoustic cavitation can be still tightly localized because it is defined by the focal profile of optoacoustic transmitter. Indeed, the free-boundary cavitation was observed under the superposed focused ultrasound. The cavitation probability was lower than 0.5%. This is probably due to low repetition rate of our pulsed lasers and therefore low intensity. We believe that the superposed configuration can be promisingly improved in many ways by varying the control parameters of both transmitters such as the negative pressure amplitude, the operation frequency, and the pulse repetition rate. We expect that the LGFU becomes a versatile modality over a broad range of applications, especially as a high-accuracy treatment tool for cells, blood vessels, and tissue layers.

6.3 High-Frequency Characterization of Optical Microring Detectors and Their Optoacoustic Imaging Applications

We investigated the characteristics of the microring detectors in the regime where the acoustic wavelengths of incident pressure are comparable or even smaller than the microring size. As the optical microring detector has a finite dimension in its diameter

and waveguide width, this is an essential step to understand how the microring responds to such high frequency ultrasound waves with short wavelengths. The responses of optical microring detector were characterized by using high-frequency "focused" ultrasound. The optoacoustic concave transmitter was as a broadband and high-frequency focused source. As the focused ultrasound is scanned by the microring in the focal plane, two types of spatial peaks were observed: (1) shoulder peaks at the ring waveguide that result from direct overlap of the main lobes of the focused ultrasound with the ring waveguide, and (2) a main peak at the ring center that is contributed by both the main lobes of low-frequency components and the side lobes of high-frequency ones. Detection of the shoulder peaks means that even a part of the microring waveguide (several μm^2 in area) has substantial sensitivity. Therefore, a practical imaging with any features smaller than the ring diameter would require a spatial deconvolution process after measurement, which includes all the contribution over the ring circumference.

In an effort to utilize the high-frequency and broadband responses and the dimensional aspects (*i.e.* small size) of the microring detectors, we proposed optoacoustic 4f imaging systems. Such properties of the microrings are highly desirable in a focal imaging configuration which receives high-frequency ultrasound coming from broad angles of incidence. We designed the system containing the microring detector the acryl-based acoustic lens. The long-range and short-range systems were designed and used for optoacoustic imaging of polymer microspheres and a single hair. The long-range system allowed to get images from the beads located at the long focal distance (39 mm). Two microspheres of 300 μm were clearly distinguished by using the high frequency harmonic components of the detected signal. The FWHM of the image obtained at the 15 MHz

frequency was ~370 μm, which is close to the nominal size of the microsphere. The spectral analysis for the time-domain signal showed that the image consists of frequency components up to 20 MHz. However, the image contrast was degraded with high-frequency ranges. We implemented the 4f imaging with a smaller object which is a single hair of 100-μm thickness. This revealed that the long-range system cannot properly resolve such small dimension. Also, the high-frequency amplitudes were weak and not sufficiently received in the detector.

In the short-range imaging system, the 4f lens with a short focal distance of 6.5 mm was used. As the acoustic attenuation for high-frequency ultrasound is greatly reduced, the 4f lens can deliver stronger pressure amplitudes to the detector. Moreover, we used an improved optical microring detector which is suitable for the focal imaging system. The new microrings have smaller dimension (40 μm in diameter) and higher sensitivity (Q~30000) [5]. As the decreased dimension of the detector improves directional responses over broad angles of incidence, the detector can receive high-frequency acoustic waves with reduced loss. The high-resolution aspects in the short-range system were clearly demonstrated using the microspheres of 100-μm diameter. Using a frequency band-pass filter over 35~45 MHz, we could obtain the exact images of the microsphere.

6.4 Future Work: All-Optical Transducers

In future, we can integrate the CNT-polymer composite transmitters with the

optical detectors for making all-optical transducers. The transmitter can be designed in either planar or focused modes. In the planar design, focused laser spots will be irradiated onto the composite film, and then an individual element will be defined by the focused laser beams. In the focal design, we can use all of the advantages investigated in this thesis. In either way, strong and high-frequency characteristics can be basically used as unique features which cannot be achieved in other modalities. However in the focal design, one important issue comes from the lens material. For a receive-mode, different lens substrates should be considered (*e.g.* polymer) to avoid large attenuation during acoustic propagation through the glass substrate.

We have considered fabricating the optoacoustic focusing lens by using a mold transfer approach (Fig. 6.1). In this way, we could form a CNT layer on polymer concave substrates. In this thesis, we did not include experimental results obtained from this type of lenses. But in general, we could obtain similar focused ultrasonic profiles which have strong shock front in positive phases (>40 MPa) and cavitation behavior in negative ones.

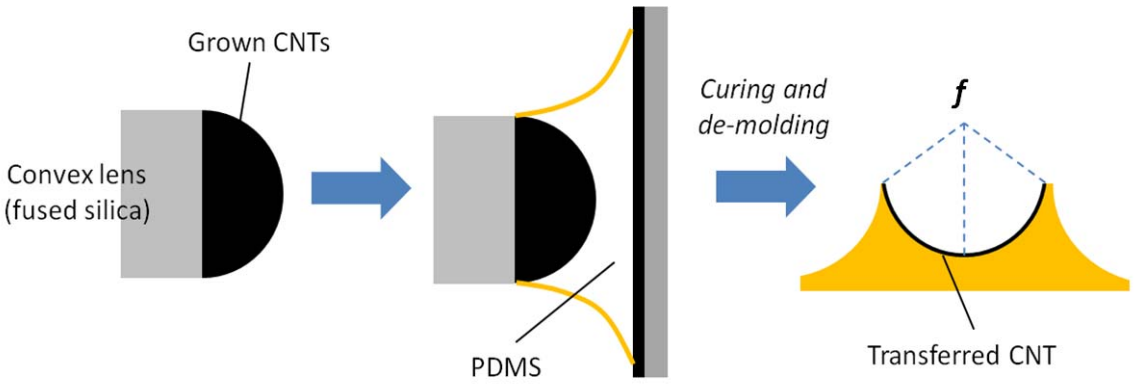

Fig. 6.1 Transfer-based fabrication of optoacoustic focusing lenses. The as-grown CNTs initially on the convex lens are transferred to a polymer structure.

We adopted the MW-CNTs again, but they were initially grown on a “convex” substrate (fused silica) coated with a catalyst layer of Fe. Then, we fabricated a molded replica which is a concave structure of PDMS (Sylgard 184, Dow Corning). After curing at 40 °C for >24 hours and then 90 °C for 2 hour, the polymer replica was de-molded bringing the CNTs from the fused substrate onto the surface of the polymer. The CNTs were embedded and surrounded by the PDMS which has a high thermal expansion coefficient.

As the optical detectors, we can consider the microrings or the Fabry-Perot type structures. The microrings can be used if the all-optical transducers demand such excellent detector responses in terms of sensitivity and high-frequency. In terms of frequency characteristic, this will be almost optimal because the transmitter generates ultrasound which has almost same spectrum as that of laser pulse as well as the detector exactly covers these frequency ranges. However, with the optoacoustic focusing lens, the Fabry-Perot detectors may be preferred. As the incoming acoustic waves are received through the lens which has several tens of mm^2 in area, the film-type detectors can receive the acoustic waves over wide areas rather than the microring cases. In the Fabry-Perot structures, the detection area is defined by the area of probing laser beam on the surface.

In the all-optical transducers, the optoacoustic focusing transmitters can be utilized in dual-functional ways. In low-amplitude regimes, this will work as a transducer-mode for imaging. Once any object is detected as a target for therapy or focused-ultrasound treatment, the same transducer can be used in high-amplitude modes. Therefore, imaging-and-treatment can be simultaneously achieved in a single platform.

Furthermore, these all-optical transducers can be designed in small structures of the order of several mm which are proper for fiber-optic integration as an attractive platform for endoscopic applications. A bundle of fiber array can be used to deliver high laser energy and generate strong pressure at the end of fibers where the optoacoustic lens is located. In these configurations, light paths for detection and generation should be properly separated for example using multiple fibers or dual-mode fibers.

APPENDIX

Appendix A

Fabrication of CNT-Polymer Composite Films and Optoacoustic Focusing Lenses

For CNT growth, we prepared fused silica substrates which have catalyst layers of Fe (~1 nm) and Fe_2O_3 (~3 nm) deposited by using a sputtering system. The fused silica substrates were plano-concave optical lenses (purchased from Edmund Optics, Barrington, NJ) with dimensions of 5.5 mm in radius-of-curvature and 6 mm in diameter for type I lens, and 11.46 mm and 12 mm for type II lens, respectively (Fig. A1). Multi-walled CNTs were grown in a mixture of C_2H_4/H_2/He in an atmospheric pressure tube furnace at 775 °C. This process led to a tangled CNT layer with high density as compared to those in solution-processed CNT layers. The as-grown CNTs were then deposited by a gold layer of 20 nm. This enhanced the optical extinction to higher than 90% without increasing the overall source thickness significantly. The elastomeric polymer, PDMS, was used again for thermo-acoustic transfer medium due to its high thermal expansion coefficient (~5-fold higher than water). The PDMS was spin-coated on the CNT-grown surface at 2000 r.p.m. for 2 minutes, and then cured at 100 °C for 1 hour. The lens design parameters are summarized in Table A1. Various lens dimensions from 3 mm in diameter up to 20 mm could be fabricated. Currently, the maximum lens size is limited by the CNT

growth chamber. This is just a technical issue. In this work, we just used the type I and II lenses.

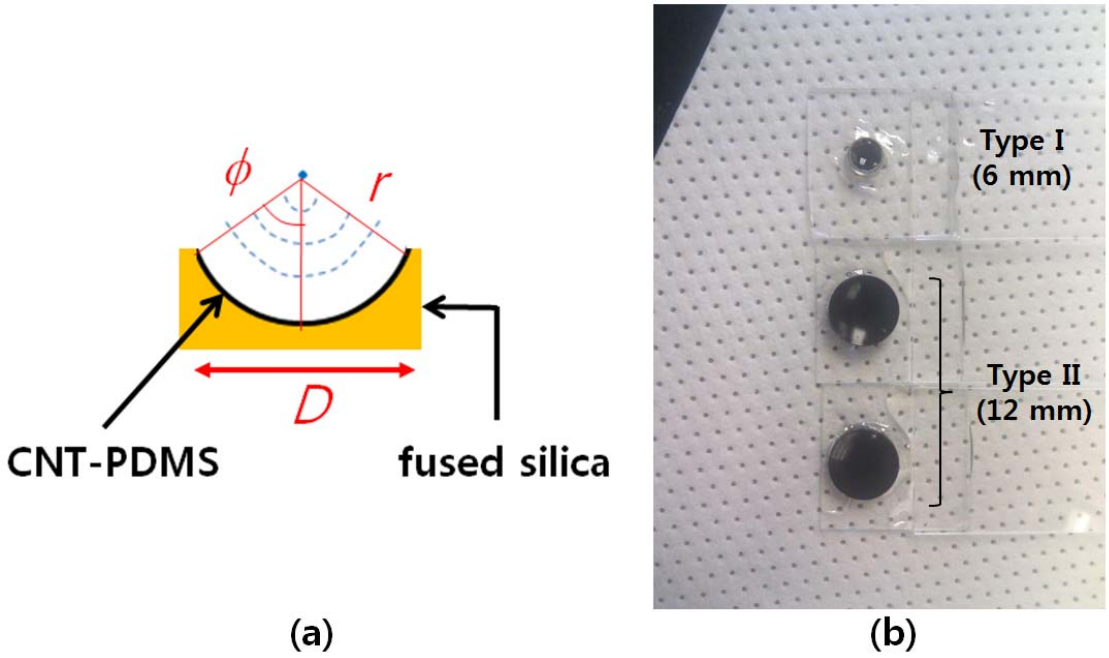

Fig. A1 (a) Structure of the optoacoustic focusing lens. The CNT-PDMS layer is formed on the concave surface. Before the PDMS coating, the gold is deposited over the CNTs. (b) Photograph of the fabricated lenses. The type I and II lenses are defined by their dimensions.

	Diameter (D)	Radius-of-curvature (r)	Angle of aperture (2ϕ)	*f*-number (r/D)
Type I	6 mm	5.5 mm	66°	0.92
Type II	12 mm	11.46 mm	63°	0.96

Table. A1 Lens parameters of the type I and II. Both have similar *f*-numbers but radii-of-curvature. Therefore, the focal distance of the type II lens is ~2-fold longer than that of the type I.